Long-Range Ising Interactions Mediated by $\lambda\phi^4$ Fields: Probing the Renormalization of Sound in Crystals of Trapped Ions

G. Martín-Vázquez[1,2] G. Aarts[3,4] M. Müller[5,6] and A. Bermudez[1,7,*]

[1]*Departamento de Física Teórica, Universidad Complutense, Madrid 28040, Spain*

[2]*Nano and Molecular Systems Research Unit, University of Oulu, Oulu 90014, Finland*

[3]*Department of Physics, Swansea University, Singleton Campus, Swansea SA2 8PP, United Kingdom*

[4]*European Centre for Theoretical Studies in Nuclear Physics and Related Areas (ECT*) and Fondazione Bruno Kessler Strada delle Tabarelle 286, Villazzano, TN 38123, Italy*

[5]*Institute for Theoretical Nanoelectronics (PGI-2), Forschungszentrum Jülich, Jülich 52428, Germany*

[6]*JARA-Institute for Quantum Information, RWTH Aachen University, Aachen 52056, Germany*

[7]*Instituto de Física Teórica, UAM-CSIC, Universidad Autónoma de Madrid, Cantoblanco, 28049 Madrid, Spain*

The generating functional of a self-interacting scalar quantum field theory (QFT), which contains all the relevant information about real-time dynamics and scattering experiments, can be mapped onto a collection of multipartite-entangled two-level sensors via an interferometric protocol that exploits a specific set of source functions. Although one typically focuses on impulsive δ-like sources, as these give direct access to n-point Feynman propagators, we show in this work that using always-on harmonic sources can simplify substantially the sensing protocol. In a specific regime, the effective real-time dynamics of the quantum sensors can be described by a quantum Ising model with long-range couplings, the range and strength of which contains all the relevant information about the renormalization of the QFT, which can now be extracted in the absence of multipartite entanglement. We present a detailed analysis of how this sensing protocol can be relevant to characterize the long-wavelength QFT that describes quantized sound waves of trapped-ion crystals in the vicinity of a structural phase transition, opening a new route to characterize the associated renormalization of sound.

I. INTRODUCTION

Large-scale fault-tolerant quantum computers have the potential to solve relevant computational problems in ways that surpass the capabilities of any classical device [1]. To achieve this long-term goal, these devices must process information by taking explicit advantage of the laws of quantum mechanics, while they also correct for the errors that occur during the computation due to imperfections and noise. In this way, one actively battles a possible accumulation of the errors [2], as has already been demonstrated in various small-scale processors [3–12], including atomic, molecular, and optical (AMO) technologies such as trapped ions [13–15].

Recent progress with noisy intermediate-scale quantum technologies [16] has shown that, even if these errors are not actively corrected for, and can thus accumulate, the level of the overall noise is sufficiently low that current noisy devices can already solve certain computational tasks that no classical computer could solve in any feasible amount of time [17,18]. This has allowed the so-called quantum advantage and supremacy to be demonstrated [19]. In theoretical physics, some of the most complicated problems appear in the study of quantum systems with a large, sometimes even infinite, number of coupled degrees of freedom. These systems are typically formulated in terms of quantum field theories (QFTs) [20,21], some of which pose problems whose solution has remained elusive for decades, in spite of the availability of large computational resources. With some notable exceptions [22], determining their specific complexity, or proving rigorously that no classical computer will ever be able to solve them in a feasible amount of time, are very delicate matters. In any case, given the limitations of current computational approaches in QFTs, e.g., real-time evolution or finite fermion densities, and their importance in

---
*bermudez.carballo@gmail.com

understanding Nature at its most fundamental level [23], any possible progress using alternative methods can be of great value. In this context, we find that the prospects of using noisy intermediate-scale quantum technologies to address open questions in QFTs is fascinating [24,25]. We also find particularly enticing that these quantum technologies may offer novel ways to experimentally realize and probe paradigmatic QFTs, which, although not finding counterparts in Nature, e.g., reduced dimensionality, contain key fundamental aspects that shape our understanding of it. We emphasize below the results of the present work in this respect.

Although the initial focus of such, so-called, quantum simulators (QSs) [24,26] has been on condensed-matter models, such as the bosonic [27,28] and fermionic [29–31] Hubbard models with cold atoms [32,33], or models of interacting spins [34–37] with trapped ions [38,39]; QSs may also find numerous applications for high-energy physics [40]. Trapped-ion systems have already been used to explore the predictions of the Dirac equation [41–43]. Similarly, cold Fermi gases in hexagonal optical lattices [44,45] serve to realize experimentally the fermion doubling in lattice discretizations of Dirac QFTs [46]. One can also explore other discretizations where topology plays a key role [47], which connects to a very fruitful line of research in cold-atom QSs [48]. The characteristic level of microscopic control of these QSs allows exploration of QFTs with additional interactions, the strength of which can be tuned independently, connecting to paradigmatic four-Fermi models [49–52] or self-interacting scalar fields [22,53,54]. In connection to our most fundamental theories of Nature [55], QSs have also been proposed to target gauge theories [56,57] with both Abelian [58] and non-Abelian [59] groups. Proposals to include fermionic matter coupled to such gauge fields [60,61], together with initial experimental progress along these lines [62–71], have made it a very active and rapidly evolving research direction [72,73] (see Ref. [40] for a recent review) with interesting connections to topological phases of matter and topological order [74–77].

In this paper, we focus on one of the aspects emphasized above: the possibility of realizing paradigmatic QFTs that can be probed in unprecedented ways. In the context of high-energy physics, one typically probes these QFTs via scattering experiments where the particles, described as the fundamental excitations of the fields, collide against each other in large accelerators. In the context of AMO quantum technologies, there are other techniques to probe a quantum field, which can be traced back to the origins of quantum optics and the theory of photodetection of the electromagnetic field [78]. Historically, there have been various models of the photodetector, such as harmonic-oscillator probes [79], an ensemble of ancillary atoms with a single ground state and a continuum of excited levels [80], or a simple two-level atom or qubit [81], all of which

get excited by the absorption of photons from the electromagnetic field. By placing these probes at different spatial locations, and detecting delayed photon coincidences, one gets information about the retarded correlation functions of this gauge field. These correlation functions play a key role in the quantum theory of optical coherence [78], and form the basis of numerous ground-breaking experiments [82,83] that have shaped the progress of AMO quantum technologies [84]. Similar ancillary probes are referred to as particle detectors in QFTs on curved space times [85], such as a quantum particle held in a box that moves with constant acceleration in the background of a scalar field [84]. The excitation rate of this accelerated particle, which is nonzero even when the field is in the vacuum, probes the so-called Unruh effect [86]. Modified versions of this particle detector, such as a two-level atom [87,88] or a harmonic oscillator [89], are commonly referred to as Unruh-DeWitt detectors, which, if correctly switched on and off, can give information about the so-called Wightman correlation function of the scalar field [90].

In the context of contemporary applications of quantum technologies, in particular, quantum sensing [91], these photon and particle detectors can be categorized as Rabi-type quantum sensors, as they rely on the excitation of the probe to gather information about the quantum field. There is, however, a different kind of quantum sensor where, rather than focusing on its excitation probability, one monitors its coherence via Ramsey interferometry [92]. Ramsey-type sensors are actually used in high-precision measurements, and exploited as frequency standards in the so-called atomic clocks [93], which include both trapped-ion and cold-atom technologies. In the context of QSs of condensed-matter models, Ramsey sensors have also been considered as probes for quantum many-body properties, both in equilibrium [94,95] to probe equal-time correlation functions [96,97], and out of equilibrium [98–102], where noise and fluctuations can give crucial information about transport phenomena.

In the context of QSs of high-energy physics, to the best of our knowledge, Ramsey-type probes have been much less studied. In Ref. [103], these probes were used to characterize the Wilson loop operator of a lattice gauge theory. In Ref. [53], Ramsey-type probes coupled to self-interacting Klein-Gordon fields have been explored for trapped-ion QSs. Although the real Klein-Gordon field [104,105] is an archetype QFT [20], and the inclusion of self-interactions, e.g., $\lambda\phi^4$ terms, shapes our understanding of crucial aspects of QFTs such as renormalization [106]; there is no fundamental particle in Nature described by this real scalar field. It is thus quite interesting that QSs have the potential to realize this paradigmatic QFT in real experiments and, actually, explore different effective dimensionalities. Moreover, as put forth in Ref. [53], one can devise a Ramsey-type protocol to probe this field theory, turning key QFT concepts such as the generating functional

[20] into experimentally measurable observables. In that work, we showed how one can devise an interferometric protocol that maps the information of such a generating functional onto a multipartite entangled state of ancillary qubits [53], which are coupled to the scalar field via a generalization of the so-called Schwinger sources [107,108]. It is interesting that, in contrast to the previous probing protocols that infer either equal-time, retarded, or Wightman correlation functions, by switching these sources on and off appropriately in the impulsive (i.e., antiadiabatic) regime [53], these entangled Ramsey sensors give access to any n-point Feynman propagator. Such time-ordered functions form the basis of current approaches to QFTs, and measuring them is thus a way of extracting all relevant information about equilibrium or real-time dynamics of the QFT, providing an alternative to scattering experiments.

A. Summary of the main results

The protocol presented in Ref. [53] can be considered as an initial step that identifies an interesting research direction: key mathematical tools used to characterize QFTs, such as the generating functional, may actually become observable quantities by leveraging advances in the field of quantum technologies. In particular, this interferometric protocol exploits entanglement via specific quantum circuits that prepare a multipartite entangled probe (see Fig. 1), which can be coupled to the interacting quantum field via fast microscopic control at the level of each of the sensing qubits, which must be placed at specific space-time points of an underlying lattice regularization of the QFT. The scheme to infer the generating functional in its

full generality requires thus a large number of qubits, deep quantum circuits to prepare the probes, fast and precise switching of the qubit-field couplings, and an excellent isolation from environmental noise such that the interferometric signal is not degraded substantially by decoherence. Even if the price is high, the reward is worth it: one would have access to all of the equilibrium and nonequilibrium properties of the simulated QFT going beyond the capabilities of present numerical approaches based on classical hardware. On the other hand, reaching these demands with current quantum technologies seems to be still far ahead. For instance, the largest multipartite maximally entangled states prepared to date with bare circuits, i.e., no error mitigation or postselection, has reached $N = 24$ qubits [109]. Additionally, depths beyond 100 gates have been achieved in recent sequential circuits with $N = 16$ qubits [110]. This is still far away from the spatial lattice sizes and temporal resolution for the fast switching that would be required to recover the continuum-limit generating functional of the QFT one is trying to probe. A timely question is thus to explore alternative strategies, which, albeit not being able to recover the full generating functional of interacting QFTs, still provide a novel manner to probe key aspects of QFTs that is readily applicable in present or near-term quantum technologies.

In this paper, we address this important question, and show that a much simpler sensing protocol for QFTs can dispense with (i) the requirement of initializing the qubits in a large multipartite entangled state, and (ii) the need of fast and accurate switching controls. We show that, by abandoning the impulsive regime to focus instead on harmonic off-resonant Ising-Schwinger sources, one can
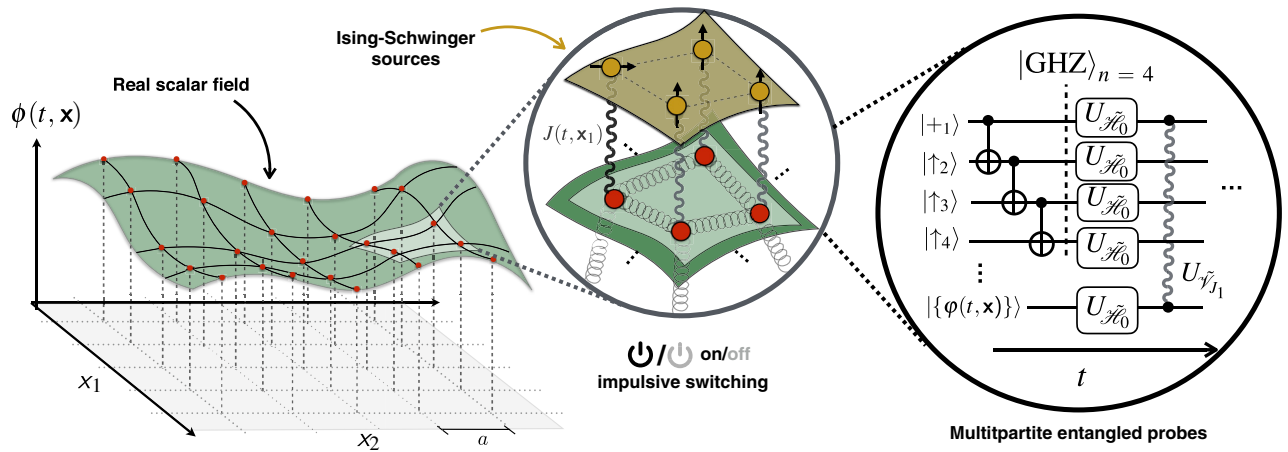

FIG. 1. Scheme of the impulsive sensors for the generating functional: a real scalar field $\phi(t, \mathbf{x})$ is coupled locally by Ising-Schwinger sources of strength $J(t, \mathbf{x})$ to an ancillary Ising field, which, in principle, also resides at every space-time point $\boldsymbol{\sigma}(t, \mathbf{x})$. In practice, the QFT will be regularized on a lattice of spacing a, and the discretized Ising field need only be placed at a reduced set of spatial locations, which can be interpreted as a multipartite sensor. By switching on and off the Ising-Schwinger sources are impulsively, as discussed in the text, one maps the information of the generating functional of the field $\mathsf{Z}[J]$ onto the Ising spins (see the first inset). The full time evolution, including the initialization of the Ising spins in a multipartite entangled state, can be represented as a quantum circuit (see the second inset).

characterize the interacting QFT by exploiting a Yukawa-type interaction between the qubits. Such an interaction takes the form of an effective quantum Ising model with long-range couplings that depend on a dimensionally reduced Euclidean propagator of the self-interacting Klein-Gordon field. Despite lacking the generality of the scheme to probe the full generating functional [53], which would allow the recovery of any real-time *n*-point function, we show that this dimensionally reduced propagator contains relevant information about various aspects of the interacting QFT. In particular, we show that it can be used to explore the renormalization of the scalar field, which can be directly probed by monitoring the dynamics of the ancillary qubits that are no longer required to be prepared in a large multipartite entangled state. Additionally, in contrast to the impulsive protocol [53], the sources need not be switched on and off in various combined experiments, but are simply adiabatically ramped up and down at the initial and final instants of the probing sequence. In order to analyze this novel probing scheme, we describe the sensor-field system through a path-integral formulation in terms of a scalar-σ model composed by a self-interacting Klein-Gordon field coupled to a constrained σ field that represents the underlying qubits. This framework allows quantitative calculations to be performed for the interacting QFT coupled to Ising-Schwinger probes, and shall be the starting point for future works addressing different aspects of this new scheme, e.g., finite temperatures, out-of-equilibrium dynamics, etc.

In addition to these theoretical results, our paper provides a detailed and realistic description of an implementation with current trapped-ion devices, going significantly beyond the description of Ref. [53]. We show that the QFT framework connects quantitatively to a long-wavelength description of the aforementioned QSs of spin models in trapped ions [34–36,39], and that nonlinearities will increase their role for experiments performed in the vicinity of a structural phase transition [111]. Here, the role of the real Klein-Gordon field is played by the transverse sound waves of the ions, which, for sufficiently low temperatures, describe the vibrations of the ions around the equilibrium positions of a linear Coulomb crystal. In contrast to sound waves in solid-state materials, a detailed long-wavelength theory shows that these vibrational excitations, the so-called phonons, are massive particles and thus move inside an effective light-cone determined by a transverse speed of sound that is experimentally tunable. As one modifies the ratio of the trap frequencies, approaching the aforementioned structural phase transition, the bare mass of the effective Klein-Gordon field reduces, whereas the role of quartic nonlinearities becomes more important. By introducing additional lasers, one can couple the transverse motion of the ions to the internal energy levels, which can be described in terms of qubits. We show quantitatively that the low-energy description of this

system is the aforementioned scalar-σ QFT, providing specific expressions for all microscopic parameters. By exploiting the connection to high-energy physics, the current paper pinpoints the origin of the long-range spin-spin couplings routinely observed in trapped-ion QSs [34–36, 39]. These can be understood as Yukawa-type interactions due to the exchange of phonons between the qubits, which, by virtue of the additional quartic self-interactions, can now be subjected to various scattering processes along the way (see Fig. 2). This allows us to predict that, in comparison to the standard phonon-mediated Ising interactions in harmonic trapped-ion crystals [34–36,39], by approaching the structural phase transition, the intensity and range of the Ising couplings get contributions from these scattering events of the virtually excited bosons, and can be neatly described in terms in light of the renormalization of QFTs. We show that the mass and wave-function renormalization of the scalar field control the main changes in interaction range and strength due to the nonlinearities. In essence, the role of the quartic interactions leads to a renormalization of transverse sound in the ion crystal, which can be probed by monitoring the real-time dynamics of an effective long-range Ising model. We believe that the results presented in this work are in reach of several current trapped-ion experiments, and provide a key insight in how nonlinearities, finite temperature, multispin interactions, etc., will come into play in near-term experiments. The new scheme analyzed in this work provides an important and timely step forward, both regarding the prospect of an experimental implementation with current techniques for QSs with large ion strings [112], as well as providing a new QFT framework for future theoretical studies such as finite-temperature effects or out-of-equilibrium dynamics.

Since the topic of this paper is multidisciplinary in nature, we have made a special effort to present our results in a way that is accessible to two communities, those working in lattice-field theories for high-energy physics and those more familiarized with quantum optics and AMO quantum technologies. We thus include additional material in Appendixes to make this work self-contained, and to present concepts in a accessible way.

II. KLEIN-GORDON SCALAR FIELDS COUPLED TO $\mathbb{Z}_2$ FIELDS

In this section, we use canonical-quantization techniques to describe two different sensing protocols for the generating functional of the massive Klein-Gordon field $\mathsf{Z}_0[J]$. In Appendix A, the reader can find details about the derivation of $\mathsf{Z}_0[J]$ for this field theory, which we now build upon to present an alternative take on the quantum-sensing protocol introduced in Ref. [53]. As described in Sec. II A, the exact form of the unitary evolution operation sheds light on the need of multipartite entangled probes to extract $\mathsf{Z}_0[J]$ within this scheme. This discussion also
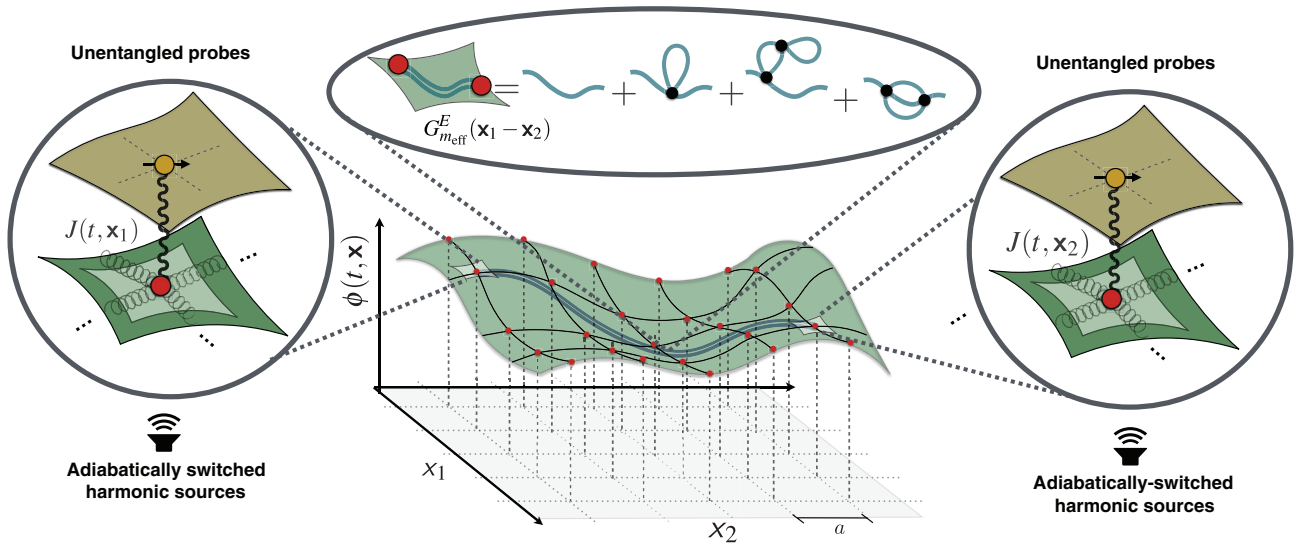
FIG. 2.   Scheme of the harmonic sensors for the generating functional: two distant Ising spins at positions $\mathbf{x}_1$ and $\mathbf{x}_2$ are coupled to the real scalar field $\phi(t, \mathbf{x})$ locally by harmonic Ising-Schwinger sources $J(t, \mathbf{x}_i) \propto \sin(\omega_J t - \mathbf{k}_J \cdot \mathbf{x}_i)$ that is adiabatically switched during the whole probing lapse. As a consequence, the scalar bosons will mediate an effective Ising interaction between the spins, which is represented by a double blue line. In the upper inset, we depict the strength of this spin-spin interaction, which is effectively controlled by a dimensionally reduced Euclidean propagator of the scalar field. In the presence of quartic couplings, this propagator will include all possible scattering events that can be represented in terms of Feynman diagrams, as displayed in the inset up to second order of the quartic interaction strength.

clarifies, as described in Sec. II B, that the mapping of $\mathsf{Z}_0[J]$ onto the probes relies on interactions mediated by the virtual exchange of Klein-Gordon bosons, which in turn suggests a simpler sensing protocol based on the use of off-resonant harmonic sources, as introduced in Sec. II B. By measuring the dynamics of a pair of unentangled probes to infer the characteristics of an effective long-range Ising Hamiltonian, one can reconstruct the two-point propagator and with it, also the free generating functional $\mathsf{Z}_0[J]$ in a simpler manner.

A. Impulsive sensors of the generating functional

In the framework of canonical quantization, the real scalar field evolving under a Klein-Gordon equation [104,105] can be described by the following Hamiltonian:

$$H_0 = \int d^d\mathbf{x}\, \mathscr{H}_0, \quad \mathscr{H}_0 = \frac{1}{2}\pi^2(x)$$
$$+ \frac{1}{2}[\nabla\phi(x)]^2 + \frac{1}{2}m_0^2\phi^2(x), \quad (1)$$

where $\phi(x), \pi(x)$ are the field operator and its conjugate momentum, both defined on a $D = d + 1$ Minkowski space time $x = (t, \mathbf{x})$, and satisfying equal-time bosonic commutation relations $[\phi(t, \mathbf{x}), \pi(t, \mathbf{x}')] = i\delta^d(\mathbf{x} - \mathbf{x}')$. Here, m_0 stands for the bare mass of the scalar bosons, ∇ contains only spatial derivatives, and we use natural units $\hbar = c = 1$.

The generating functional $\mathsf{Z}_0[J]$ depends on the so-called Schwinger sources $J(x)$ [107,108], which are classical fields that introduce local perturbations in the original QFT, Eq. (1), modifying the number of excitations of the field, and thus creating or annihilating scalar bosons (see Appendix A). We consider the promotion of these classical sources to quantum-mechanical degrees of freedom [53], by introducing an Ising field $\boldsymbol{\sigma}(x)$ expressed in terms of the identity and Pauli matrices

$$\sigma^0 = \mathbb{I}_2, \quad \sigma^1 = X, \quad \sigma^2 = Y, \quad \sigma^3 = Z, \quad (2)$$

in the corresponding basis $\{|0_\mathbf{x}\rangle = |\uparrow_\mathbf{x}\rangle, |1_\mathbf{x}\rangle = |\downarrow_\mathbf{x}\rangle\}$. With this notation, the Ising fields can be interpreted as qubits [1] that will serve as two-level quantum sensors located at different space-time points (see Fig. 1). Accordingly, the Hilbert space becomes a tensor product $\mathscr{H} = \mathscr{H}_\phi \otimes \mathscr{H}_\sigma$, and one can exploit the coupling between the scalar and Ising fields to define a measurement protocol for $\mathsf{Z}_0[J]$. This becomes particularly interesting when including interactions, as the same measurement scheme applies, but the generating functional now contains nontrivial information about the interacting fields, such as renormalization and the underlying fixed points [106,113].

As discussed in Ref. [53], the Schwinger sources are promoted to $J(x) \to \boldsymbol{J}(x) \cdot \boldsymbol{\sigma}(x)$, which becomes interesting for $\boldsymbol{J}_\alpha(x) = J(x)(\delta_{\alpha,0} - \delta_{\alpha,3})/2$, as the scalar field then couples to

$$\boldsymbol{J}(x) \cdot \boldsymbol{\sigma}(x) = J(x)P(x), \quad (3)$$

where we introduce the orthogonal Ising projector

$$P(x) = |\downarrow_{\mathbf{x}}\rangle \langle\downarrow_{\mathbf{x}}| = \frac{1}{2}[\mathbb{I} - Z(x)]. \qquad (4)$$

The new Hamiltonian density $\tilde{\mathscr{H}}_0 + \tilde{\mathscr{V}}_J$ with these Ising-Schwinger sources is

$$\tilde{\mathscr{H}}_0 = \mathscr{H}_0 + \delta\epsilon(x)Q(x), \quad \tilde{\mathscr{V}}_J = -J(x)\phi(x)P(x), \quad (5)$$

where we introduce the remaining orthogonal projector

$$Q(x) = |\uparrow_{\mathbf{x}}\rangle \langle\uparrow_{\mathbf{x}}| = \frac{1}{2}[\mathbb{I} + Z(x)], \qquad (6)$$

and $\delta\epsilon(x)$ is the energy density for the Ising field. Since $[P(x), Q(y)] = 0$, it is straightforward to see that the time-evolution operator $U(t_f, t_0) = U_{\tilde{\mathscr{H}}_0} U_{\tilde{\mathscr{V}}_J}$ can be expressed in terms of two unitaries

$$U_{\tilde{\mathscr{H}}_0} = e^{-i\int d^D x \tilde{\mathscr{H}}_0}, \quad U_{\tilde{\mathscr{V}}_J} = \mathsf{T}\left\{e^{+i\int d^D x J(x)\phi_H(x)P(x)}\right\}, \qquad (7)$$

in complete analogy to the situation for the standard Schwinger sources in Eq. (A2). Here, $\mathsf{T}\{\cdot\}$ is the time-ordering operator, the scalar fields $\phi_H(x) = (U_{\tilde{\mathscr{H}}_0})^\dagger \phi(x) U_{\tilde{\mathscr{H}}_0}$ evolve in the Heisenberg picture with respect to the unsourced Klein-Gordon Hamiltonian (1), whereas the Ising projectors do not change since $U_{\tilde{\mathscr{H}}_0} P(x)(U_{\tilde{\mathscr{H}}_0})^\dagger = P(x)$. By using the Magnus expansion [114,115] described in Eq. (A7) of the Appendix, and carrying out the steps in analogy to the Klein-Gordon QFT with classical sources of Appendix A, we find

$$U_{\tilde{\mathscr{V}}_J} = U_N e^{-(1/2)\int d^D x_1 \int d^D x_2 P(x_1)J(x_1)\Delta_{m_0}(x_1-x_2)J(x_2)P(x_2)}. \qquad (8)$$

Here, we introduce the normal-ordered unitary

$$U_N =: e^{-i\int d^D x J(x)\phi_H(x)P(x)} :, \qquad (9)$$

and the time-ordered Feynman propagator of the scalar field

$$\Delta_{m_0}(x) = \int_k \tilde{\Delta}_{m_0}(k)e^{-ikx}, \quad \tilde{\Delta}_{m_0}(k) = \frac{i}{k^2 - m_0^2 + i\epsilon}, \qquad (10)$$

where $k = (\omega, \mathbf{k})$, and we define $\int_k = \int d^D k/(2\pi)^D$, and $\epsilon \to 0^+$. The structure of Eq. (8) already suggests that it may be possible to map all the information of the

generating functional (11) of the massive Klein-Gordon field

$$\mathsf{Z}_0[J] = e^{-(1/2)\int d^D x_1 \int d^D x_2 J(x_1)\Delta_{m_0}(x_1-x_2)J(x_2)}, \qquad (11)$$

onto the dynamics of the qubits by an appropriate protocol. Note that $\mathsf{Z}_0[0] = 1$, so we are referring to the free normalized generating functional, or the full one $\mathsf{Z}[0] = 1$, in this paper.

The key idea underlying the mapping of the generating functional onto the Ising probes, presented in Ref. [53] using a different approach, is that the full time evolution $U(t_f, t_0) = U_{\tilde{\mathscr{H}}_0} U_{\tilde{\mathscr{V}}_J}$ can map this information into the amplitudes of a specific initial state. One starts by preparing a Greenberger-Horne-Zeillinger (GHZ) state for the qubits through the quantum circuit displayed in Fig. 1, which applies concatenated CNOT gates to a product input state, and should be extended to all the locations of the Ising spins. After these gates [1], and right before the Ising-Schwinger sources are switched on, the state is $|\psi(t_0)\rangle = |0\rangle \otimes |\text{GHZ}\rangle$, where $|0\rangle$ is the Klein-Gordon vacuum, and $|\text{GHZ}\rangle = (\Pi_{\mathbf{x}}|\uparrow_{\mathbf{x}}\rangle + \Pi_{\mathbf{x}}|\downarrow_{\mathbf{x}}\rangle)\sqrt{2}$ is a multipartite entangled state. We now let the scalar and Ising fields couple through the Ising-Schwinger sources, and obtain the time-evolved state $|\psi(t_f)\rangle = U_{\tilde{\mathscr{H}}_0} U_{\tilde{\mathscr{V}}_J} |\psi(t_0)\rangle$, where the unitaries are described in Eq. (7). Due to trivial action of the normal-ordered part, Eq. (9), on the Klein-Gordon vacuum, and the action of the Ising projectors on the corresponding qubit states, only the second part of the entangled state evolves nontrivially, yielding

$$|\psi(t_f)\rangle = \frac{1}{\sqrt{2}}|0\rangle \otimes \left(\Pi_{\mathbf{x}}|\uparrow_{\mathbf{x}}\rangle + \mathsf{Z}_0[J]e^{i\int d^D x \delta\epsilon(x)}\Pi_{\mathbf{x}}|\downarrow_{\mathbf{x}}\rangle\right). \qquad (12)$$

Here, we readily find that the free generating functional (11) appears in the relative amplitude of the time-evolved spin state, after neglecting an irrelevant global phase factor that oscillates with the zero-point energy of the scalar field. The signal can be extracted by measuring the global parities

$$\mathsf{P}_1[J] = \langle\psi(t_f)|\Pi_{\mathbf{x}}X(\mathbf{x})|\psi(t_f)\rangle = \text{Re}\{\mathsf{Z}_0[J]e^{i\int d^D x \delta\epsilon(x)}\},$$

$$\mathsf{P}_2[J] = \langle\psi(t_f)|\Pi_{\mathbf{x}}Y(\mathbf{x})|\psi(t_f)\rangle = \text{Im}\{\mathsf{Z}_0[J]e^{i\int d^D x \delta\epsilon(x)}\}. \qquad (13)$$

After introducing the generating functional of connected propagators, which in the noninteracting case simply reads

$$\mathsf{W}_0[J] = -i\log\mathsf{Z}_0[J]$$
$$= \frac{i}{2}\int d^D x_1 \int d^D x_2 J(x_1)\Delta_{m_0}(x_1-x_2)J(x_2). \qquad (14)$$

Here, one can see that this functional is encoded in the relative phase of the multipartite entangled state, Eq. (12),

unveiling some analogy with Ramsey interferometry [92], one of the key methods in quantum sensing [91]. The global parities are thus a multipartite generalization of a pair of Ramsey signals

$$P_1[J] = \cos\left(W_0[J] + \int d^D x \delta\epsilon(x)\right),$$

$$P_2[J] = \sin\left(W_0[J] + \int d^D x \delta\epsilon(x)\right). \quad (15)$$

Selecting specific timings (t_0, t_f) would allow one to reconstruct the desired generating functional for any particular set of sources $J(x)$ from experimental data. This result teaches us an important lesson: mathematical constructs in QFTs, such as the generating functional, can indeed become observable quantities when combining ideas from high-energy physics and AMO quantum technologies.

As discussed in Ref. [53], the qubits need not be attached to every space-time point when one is only interested in recovering a specific n-point propagator (A3). In that case, it suffices to use n qubits located at the desired spatial locations $\delta\epsilon(x) = \omega_0 \sum_{i=1}^n \delta^d(\mathbf{x} - \mathbf{x}_i)$, where ω_0 is the transition frequency between the two levels, and switch on and off the sources impulsively (i.e., nonadiabatically with respect to any other timescale in the problem) at the corresponding lapses of time $J(x) = \sum_i J_i \delta^D(x - x_i)$, as indicated in Fig. 1. One would then gather the interferometric experimental data P_1, P_2 for various combinations of the impulsive sources [53], and infer the corresponding functional derivatives that lead to the desired n-point propagator. In the simplest situation, inferring $\Delta_{m_0}(x_1 - x_2)$ requires repeating the interferometric protocol four times using two qubits at each of the spatial locations of interest $\mathbf{x}_1, \mathbf{x}_2$, and switching on and off the sources at the corresponding times t_1, t_2 of the space-time points x_1, x_2. Together with the requirement of using multipartite entangled states for the initialization of the Ramsey probe, maintaining the coherence of macroscopically distinct states, and repeating the whole experimental sequence to extract the quantum-mechanical statistics, this sensing protocol turns out to be quite challenging from an experimental perspective. In the following section, we describe a simpler alternative.

B. Harmonic sensors and long-range Ising models

The above simple calculation for the free Klein-Gordon field unveils an interesting fact, which was partially hidden under the general formalism for interacting fields [53]. Equation (8) shows that the $Z_0[J]$ mapping relies on unitaries describing pairwise interactions $U_{\tilde{\mathcal{V}}_J} = U_N \Pi_{x_1 x_2} U_{x_1 x_2}$ with

$$U_{x_1,x_2} = e^{-(1/2)P(x_1)J(x_1)\Delta_{m_0}(x_1-x_2)J(x_2)P(x_2)}. \quad (16)$$

This unitary represents a pairwise coupling between distant qubits, which must be mediated by the Klein-Gordon bosons acting as fundamental carriers of a spin-spin interaction. Since the Feynman propagator of the scalar field appears in Eq. (16), there might be simpler measurement protocols to extract relevant properties of the QFT without resorting to the full generating-functional protocol just described.

Let us note, before moving on, that the crucial aspect of the above pairwise unitary is not restricted to the specific form of the Ising-Schwinger sources, which involve orthogonal projectors, Eq. (5). The key point is that the coupling must contain a qubit operator $P(x) \to O(x)$ that, in the Heisenberg picture with respect to the unsourced Hamiltonian (5), commutes with itself at different instants of time $[O_H(x), O_H(y)] = 0$. As becomes clear when discussing the particular application for trapped-ion quantum computers [116,117], one can find various schemes where this operator is any of the Pauli matrices $O(x) \in \{X(x), Y(x), Z(x)\}$. In the following, we solely focus on the Z-type couplings

$$\tilde{\mathcal{V}}_J = -J(x)\phi(x)Z(x), \quad (17)$$

leading to Ising ZZ pairwise unitaries

$$U_{x_1,x_2} = e^{-(1/2)Z(x_1)J(x_1)\Delta_{m_0}(x_1-x_2)J(x_2)Z(x_2)}, \quad (18)$$

but note that the results will be interchangeable to the other XX or YY Ising interactions.

As shown below, for certain types of sources, these pairwise unitaries can be expressed in terms of an effective time-independent Hamiltonian, which allow for a different sensing protocol. In particular, the probes evolve under an effective Ising model with long-range couplings H_{eff}, which controls completely the nontrivial part of the time evolution

$$U(t_f, t_0) \approx U_{\tilde{\mathcal{H}}_0} U_{\text{eff}} = e^{-i(t_f-t_0)\tilde{H}_0} e^{-i(t_f-t_0)H_{\text{eff}}}. \quad (19)$$

Instead of using nonadiabatic sources that are switched on and off in the impulsive regime, we consider a harmonic source

$$J(x) = J_0 \sin(k_J x) = J_0 \sin\left(\omega_J t - \mathbf{k}_J \cdot \mathbf{x}\right), \quad (20)$$

where J_0 is the coupling strength density, and $k_J = (\omega_J, \mathbf{k}_J)$ is the external D-momentum determining the plane-wave harmonic source. We also consider that the source lies below the resonance of the Klein-Gordon modes (i.e., $\omega_J \lesssim m_0$) and, moreover, its strength density is constrained according to

$$J_0 \ll (\omega_{\mathbf{k}} - \omega_J) d^d \mathbf{k} < (\omega_{\mathbf{k}} + \omega_J) d^d \mathbf{k}. \quad (21)$$

In this regime, the time integrals underlying the space-time formulation of the evolution operator (8) can be performed

analytically using the forward and backward parts of the Feynman propagator (A9). We find that the normal-ordered part of Eq. (8) becomes negligible, such that the evolution of the scalar field and the Ising spins gets effectively decoupled. Whereas the former evolves under the Klein-Gordon dynamics, Eq. (1), the spins also experience the second-order term including the pairwise couplings, Eq. (18), which leads to

$$U_{\text{eff}} = e^{i(t_f - t_0) \int d^d x_1 \int d^d x_2 \int_k \{J_0^2 \cos[(\mathbf{k} - \mathbf{k}_J) \cdot (\mathbf{x}_1 - \mathbf{x}_2)]/}$$
$$\times \, (\omega_{\mathbf{k}}^2 - \omega_J^2)\} Z(\mathbf{x}_1) Z(\mathbf{x}_2), \quad (22)$$

where $\int_k = \int d^d k/(2\pi)^d$ stands for the integrals with respect to the spatial components of the D momentum. Using Eq. (19), one readily identifies an Ising Hamiltonian

$$H_{\text{eff}} = \frac{1}{2} \int d^d x_1 \int d^d x_2 J(\mathbf{x}_1 - \mathbf{x}_2) Z(\mathbf{x}_1) Z(\mathbf{x}_2), \quad (23)$$

where the factor of 1/2 avoids double counting of pairs, and we introduce the long-range coupling-strength density

$$J(\mathbf{x}_1 - \mathbf{x}_2) = -2J_0^2 \int_k \frac{\cos[(\mathbf{k} - \mathbf{k}_J) \cdot (\mathbf{x}_1 - \mathbf{x}_2)]}{\mathbf{k}^2 + (m_0^2 - \omega_J^2)}. \quad (24)$$

It is worth pointing out that, despite starting with a local Lorentz-invariant field theory in Eqs. (1) and (5), it seems that we arrive to an action at a distance between the Ising fields (23) that naively violates causality. Note, however, that the relevant timescale of the problem $t \sim 1/J(\mathbf{x}_1 - \mathbf{x}_2) d^{2d} \mathbf{x} \gg ||\mathbf{x}_1 - \mathbf{x}_2||/c = t_{\text{ret}}$, where we include again the speed of light to identify the corresponding retardation time t_{ret}. Accordingly, the regime of validity of the effective Ising model, Eq. (23), assumes that the timescales are sufficiently large for the bosons to causally connect any pair of qubits.

Let us also point out that, in order to achieve this purely unitary dynamics, keeping the Ising fields off resonant is crucial. Otherwise, the scalar bosons could also act as a source of dissipation, as our field theory could be understood as a multiqubit continuum limit of the unbiased spin-boson model at zero temperature [118–120]. Here, the harmonic frequency would play the role of the so-called quantum tunneling $\Delta_{\text{QT}} \approx \omega_J$, provided that Eq. (60) is fulfilled. Neglecting possible collective dissipative effects, the main source of irreversible dynamics would appear in the form of decoherence with a dephasing rate Γ_d that is proportional to the spectral density $S(\omega)$ of the Klein-Gordon modes at a slightly renormalized tunneling amplitude $\omega_{J,r} < \omega_J < m_0$ [121]. Since there are no modes with frequency $\omega_{\mathbf{k}} < m_0$, the corresponding spectral density would be zero $S(\omega_{J,r}) = 0$, such that $\Gamma_d = 0$, and we can simply focus on the purely coherent dynamics of Eq. (19).

Coming back to the integral (24), we note that it can be expressed in terms of the dimensionally reduced Euclidean propagator of a Gaussian field in d dimensions [106, 122,123]. This is defined through the following Green's function:

$$\left(-\nabla^2 + m_{\text{eff}}^2\right) G_{m_{\text{eff}}}^E(\mathbf{x}) = \delta^d(\mathbf{x}), \quad (25)$$

where the effective mass is shifted from the bare mass to

$$m_{\text{eff}}^2 = m_0^2 - \omega_J^2. \quad (26)$$

Since the Compton wavelength in natural units is simply the inverse of the bare mass $\xi_0 = 1/m_0$, we can define the following effective wavelength:

$$\xi_{\text{eff}} = m_{\text{eff}}^{-1} = 1/\left(m_0^2 - \omega_J^2\right)^{1/2}, \quad (27)$$

which shall control the range of the mediated interactions.

This Euclidean propagator can be obtained by lowering the dimension $D = d + 1 \to d$ of the Feynman propagator of Eq. (10), and making a Wick rotation, yielding

$$G_{m_{\text{eff}}}^E(\mathbf{x}) = \int_k \frac{e^{i\mathbf{k}\cdot\mathbf{x}}}{\mathbf{k}^2 + m_{\text{eff}}^2} = \left(\frac{m_{\text{eff}}}{||\mathbf{x}||}\right)^\nu \frac{K_\nu(m_{\text{eff}}||\mathbf{x}||)}{(2\pi)^{\nu+1}}, \quad (28)$$

where $\nu = (d/2) - 1$, and $K_\nu(u)$ is the modified Bessel function of the second kind [124], also called the Basset function [125].

We thus find that the effective spin-spin couplings mediated by a D-dimensional Klein-Gordon field subjected to harmonic Ising-Schwinger sources are controlled by the dimensionally reduced Euclidean propagator via

$$J(\mathbf{x}_1 - \mathbf{x}_2) = -2J_0^2 G_{m_{\text{eff}}}^E(\mathbf{x}_1 - \mathbf{x}_2) \cos\left[\mathbf{k}_J \cdot (\mathbf{x}_1 - \mathbf{x}_2)\right]. \quad (29)$$

Let us pause for a moment and analyze this result. First of all, one can check that the above expressions are dimensionally correct in mass and energy units. According to Eq. (1), the natural or scaling dimension of the scalar field is $d_\phi = (d-1)/2$, whereas the Ising field is dimensionless $d_\sigma = 0$. Therefore, the Euclidean propagator (28) has natural dimension $d_{G_m^E} = d - 2$, whereas the coupling strength J_0, Eq. (20), has natural dimension $d_{J_0} = (d+3)/2$, and one finds that the effective Ising Hamiltonian (23) has units of energy. We now discuss the implications of the form of the spin-spin couplings, Eq. (29), in various dimensions. For the $D = 3 + 1$ Klein-Gordon field, $\nu = 1/2$, and the modified Bessel function is $K_{1/2}(u) = \sqrt{\pi/2u}e^{-u}$, such that the Ising couplings become

$$d = 3, \quad J(\mathbf{x}) = -\frac{J_0^2}{2\pi} \frac{e^{-(||\mathbf{x}||/\xi_{\text{eff}})}}{||\mathbf{x}||} \cos\left(\mathbf{k}_J \cdot \mathbf{x}\right). \quad (30)$$

Hence, we identify a Yukawa-type interaction between the qubits (i.e., screened Coulomb decay) [126]. In fact, the

analogy becomes clearer when writing the spins in terms of fermions via a Jordan-Wigner transformation [127], since the Ising-Schwinger source term, Eq. (5), becomes a Yukawa coupling between the fermionic charge density and a propagating scalar field, although the former would be spinless and static rather than that described by a relativistic Dirac field.

We note that the range of the Yukawa interaction, Eq. (30), is controlled by the inverse of the effective mass, Eq. (26), and can thus be tuned by placing the frequency of the harmonic source ω_J closer or further from the bare mass m_0. If $\mathbf{k}_J = 0$, the spin couplings are always negative, and would thus describe an Ising-Yukawa ferromagnet. Note that, as advanced above, the Ising field need not be densely distributed over the whole Minkowski space time, but can be arranged at

$$\delta\epsilon(x) = \omega_0 \sum_{i=1}^{n} \delta^d(\mathbf{x} - \mathbf{x}_i). \quad (31)$$

In this situation, ferromagnetic couplings can also be achieved for a harmonic source with nonzero momentum if the qubits are arranged in a plane or line orthogonal to the plane wave $\mathbf{k}_J \perp (\mathbf{x}_i - \mathbf{x}_j)$. Likewise, if the qubits are contained in a region much smaller than the harmonic wavelength $\mathbf{k}_J \cdot (\mathbf{x}_i - \mathbf{x}_j) \approx 0$, the interactions are approximately ferromagnetic. Away from these conditions, the Yukawa-decaying couplings will alternate between ferromagnetic and antiferromagnetic depending on the qubit distance, which can lead to magnetic frustration.

For the $D = 1 + 1$ Klein-Gordon field $\nu = -1/2$, the modified Bessel function is $\mathsf{K}_{-1/2}(u) = \mathsf{K}_{1/2}(u)$, such that

$$d = 1, \quad \mathsf{J}(x) = -\mathsf{J}_0^2 \frac{e^{-(|x|/\xi_{\text{eff}})}}{m_{\text{eff}}} \cos\left(k_{J,x} x\right). \quad (32)$$

The situation is similar to the one discussed above, albeit with exponentially decaying spin-spin interactions. Whereas for small distances $||\mathbf{x}_1 - \mathbf{x}_2|| \ll \xi_{\text{eff}}$, we get a Coulomb-type decay in three dimensions $\mathsf{J}(\mathbf{x}_1 - \mathbf{x}_2) \propto 1/||\mathbf{x}_1 - \mathbf{x}_2||$, which gets exponentially screened at larger spatial separations, the one-dimensional case, Eq. (32), is always described by exponentially decaying interactions regardless of the distance.

Finally, for the $D = 2 + 1$ scalar field $\nu = 0$, the modified Bessel function cannot be expressed in terms of elementary functions. In this case, one finds

$$d = 2, \quad \mathsf{J}(\mathbf{x}) = -\frac{\mathsf{J}_0^2}{\pi} \mathsf{K}_0\left(\frac{||\mathbf{x}||}{\xi_{\text{eff}}}\right) \cos\left(\mathbf{k}_J \cdot \mathbf{x}\right). \quad (33)$$

For small spatial separations $||\mathbf{x}_1 - \mathbf{x}_2|| \ll \xi_{\text{eff}}$, there are logarithmically decaying couplings $\mathsf{J}_2(\mathbf{x}_1 - \mathbf{x}_2) \approx -\gamma + \log(2\xi_{\text{eff}}/||\mathbf{x}_1 - \mathbf{x}_2||)$, where $\gamma \approx 0.577$ is Euler's constant. Conversely, for long distances $||\mathbf{x}_1 - \mathbf{x}_2|| \gg \xi_{\text{eff}}$,

one obtains a power-law coupling that gets exponentially screened.

Before concluding this section, let us also note that one can include quantum fluctuations in the effective Ising models by modifying the perturbation in Eq. (5) to

$$\tilde{V} \rightarrow \hat{V} = \int d^d x \left[-J(x)\phi(x)Z(x) - H_t(x)X(x) \right], \quad (34)$$

where $H_t(x)$ is a new coupling-strength density. We assume that the Ising fields are distributed in a certain spatial arrangement $\mathbf{x}_i \in \Lambda_s$, such that

$$H_t(x) = 2h_t(x)\cos(\omega_0 t), \quad h_t(x) = h_t \sum_{i=1}^{n} \delta^d(\mathbf{x} - \mathbf{x}_i),$$

$$J(x) = \sum_{i=1}^{n} J_0 \sin\left(\omega_J t - \mathbf{k}_J \cdot \mathbf{x}_i\right) \delta^d(\mathbf{x} - \mathbf{x}_i), \quad (35)$$

where the couplings J_0, h_t have now units of mass and energy. The nontrivial part of the time-evolution operator, considering that $h_t \ll 2\omega_0$, can now be described as

$$U_{\hat{V}_J} = \mathsf{T}\left\{ e^{+i \int dt \sum_i \left[J(t,\mathbf{x}_i)\phi_H(t,\mathbf{x}_i)Z(t,\mathbf{x}_i) + h_t X(t,\mathbf{x}_i) \right]} \right\}, \quad (36)$$

We can now repeat the previous procedure to calculate the evolution operator, but differences will arise as the Magnus expansion is no longer exact at second order, Eq. (A7). Nonetheless, the additional terms can be neglected if the coupling constraint, Eq. (60), is changed so that it encompasses both couplings

$$|J_0|, |h_t| \ll (\omega_{\mathbf{k}} - \omega_J), (\omega_{\mathbf{k}} + \omega_J). \quad (37)$$

We then arrive at a long-range version of the transverse-field quantum Ising model [128,129], namely

$$H_{\text{eff}} = \frac{1}{2} \sum_{i=1}^{n} \sum_{j=1}^{n} J_{ij} \, Z(\mathbf{x}_i)Z(\mathbf{x}_j) - h_t \sum_{i=1}^{n} X(\mathbf{x}_i), \quad (38)$$

where the spin-spin couplings $J_{ij} = \mathsf{J}(\mathbf{x}_i - \mathbf{x}_j)J_0^2/\mathsf{J}_0^2$ have units of mass and energy, and are thus controlled by the D-dimensional Euclidean Green's function (29). In analogy to the nearest-neighbor models [128,129], there is a competition between magnetic phases that break spontaneously the $\mathbb{Z}_2$ symmetry $P_1 = \Pi_{\mathbf{x}_i} X(\mathbf{x}_i)$ that inverts $Z(\mathbf{x}_i) \rightarrow P_1 Z(\mathbf{x}_i) P_1 = -Z(\mathbf{x}_i)$; and paramagnetic phases where all spins point in the direction of the external transverse field h_t. Neglecting the possible frustration due to the periodic alternation between ferro and antiferro couplings, we expect that the exponential screening at large distances will lead to critical theories in the Ising universality class,

which have the same scaling behavior as the corresponding nearest-neighbor models.

Let us now switch to the discussion of the simplified quantum sensors of the massive Klein-Gordon field. Regardless of the phase diagram of the Ising spins in the thermodynamic limit $n \to \infty$, if one is interested in the characterization of the underlying scalar field, a pair of Ising spins can suffice as sensor qubits $n = 2$ (see Fig. 2), providing a much simpler scheme than the one presented above for the full generating functional. First of all, we do not require initializing the system in a multipartite entangled state, but instead in $|\Psi_0\rangle = |0\rangle \otimes |+_i\rangle \otimes |+_j\rangle$, where we recall that $|0\rangle$ is the Klein-Gordon vacuum, and $|+_i\rangle = (|\uparrow_{\mathbf{x}_i}\rangle + |\downarrow_{\mathbf{x}_i}\rangle)/\sqrt{2}$ is a coherent superposition for each of the Ising probes. Secondly, instead of measuring the global parities, Eq. (13), it will suffice to measure a single-qubit observable in the Pauli basis, e.g., $X(\mathbf{x}_i)$, in the time-evolved state $|\Psi_f\rangle = U[t_f, (t_f - t_0)/2]X(\mathbf{x}_i)X(\mathbf{x}_j)U[(t_f - t_0)/2, t_0]|\Psi_0\rangle$. Setting $h_t = 0$, this time evolution yields

$$\langle \Psi_f | X(\mathbf{x}_i) | \Psi_f \rangle = \langle \Psi_0 | U_{\tilde{\mathcal{V}}_J}^\dagger X(\mathbf{x}_i) U_{\tilde{\mathcal{V}}_J} | \Psi_0 \rangle$$
$$= \cos \left[2J_{ij}(t_f - t_0) \right], \qquad (39)$$

such that one could extract the spin-spin coupling strength J_{ij} from the real-time evolution of the transverse magnetization. We note that these periodic oscillations resemble the dynamics of the global parity observables encoding the full connected generating functional (15). The bare mass of the Klein-Gordon field m_0 and the bare coupling J_0 could be inferred by repeating the same scheme for different frequencies of the harmonic source ω_J, as this should change the range of the interaction and lead to different oscillation frequencies. With this information, one can reconstruct $Z_0[J]$ in Eq. (11).

Note that, in addition to dispensing with the need of preparing large multipartite entangled states, the previous evolution is of the spin-echo type [130], and will thus refocus the dephasing caused by external fluctuations that affect the qubits on a slower timescale than each of the single experimental runs. In contrast, spin echos or any other dynamical-decoupling sequence [131], cannot be incorporated in the generating-functional sensing scheme of Ref. [53], as it would also refocus some of the signals that are required to estimate the derivatives. We conclude that the harmonic scheme is not only simpler than the impulsive one, but also more robust to noise.

III. SELF-INTERACTING SCALAR FIELDS COUPLED TO $\mathbb{Z}_2$ FIELDS

In this section, we describe the previous sensing protocols in the presence of self-interactions in the massive Klein-Gordon field, which leads to the so-called $\lambda\phi^4$

QFT, and can be addressed by the use of functional-integral methods. In Appendix B, we review this functional approach for the full generating functional of the interacting scalar field $Z[J]$ in the absence of the Ising spins. This yields a graphical representation of $Z[J]$ in terms of Feynman diagrams, where the logarithm of the full generating functional can be expressed as a series in even powers of the source functions weighted by the renormalized connected propagators. To extend these results to the full problem with Ising-Schwinger sources, we describe in Sec. III A a spin-path integral representation of the amplitude of propagation between two arbitrary states of the Ising and scalar fields, which leads to an effective scalar-σ QFT. In Sec. III B, we show that the $\lambda\phi^4$ bosons act as mediators of Ising-type interactions between $2n$ spins, each of which is controlled by the renormalized $2n$-point connected propagator of the self-interacting scalar bosons. For harmonic sources in the specific regime of the previous section, the leading term leads again to a quantum Ising Hamiltonian with long-range couplings, the range of which now accounts for all the possible scattering events that the boson can undergo while propagating between the corresponding pair of Ising spins. This shows that the sensing scheme of Sec. II, when applied to the full interacting case, can gain information about the renormalization effects, and thus probe this QFT in a novel manner.

A. Spin-path integral and scalar-σ field theory

As discussed in the previous section, the real Klein-Gordon field is the simplest model where one can introduce key concepts and techniques to be used later in more complicated QFTs. For instance, including quartic self-interactions in the Klein-Gordon field, Eq. (1), leads to the $\lambda\phi^4$ model

$$\mathscr{H} = \mathscr{H}_0 + \mathscr{V}_{\text{int}}, \quad \mathscr{V}_{\text{int}} = \frac{\lambda_0}{4!} \phi^4(x), \qquad (40)$$

where λ_0 is the bare coupling strength. This model has played a leading role in the development of QFT. On the one hand, it is a cornerstone in our understanding of the spontaneous breakdown [132,133] and restoration [134,135] of symmetries in QFTs. This model has also been a neat playground to understand the conceptual implications of the renormalization of QFTs [106,136], such as the role of fixed points controlling the long-wavelength properties, finding many applications in the theory of phase transitions and critical phenomena [137]. Finally, we note that the $\lambda\phi^4$ model has also been a cornerstone in the constructive approach to QFTs, allowing to prove rigorous results for various dimensions [138–144].

In Appendix B, we review the effects of the $\lambda\phi^4$ interactions using the path-integral formalism for the generating functional (B23). Paralleling our approach for the free Klein-Gordon field, we can use this discussion as a guide

to understand how the self-interactions affect the effective Ising models, Eq. (38), when considering harmonic Ising-Schwinger sources. As reviewed in the Appendix, to get the path-integral formulation (B3) of the full generating functional $Z[J]$ (B2), one uses the resolution of the identity in the field and momentum orthonormal basis of the scalar field. To include the Ising-Schwinger sources and the transverse field, Eq. (34), one may complement this basis with that of spin coherent states [21,145], defined through the action of the ladder operators on a fiducial state

$$|\mathbf{\Omega}(x)\rangle = e^{\tan[\theta_s(x)/2]e^{i\phi_s(x)}S^+(x)}|S,-S\rangle_x. \tag{41}$$

Here, $|S,-S\rangle_x = |\downarrow\rangle_x$, and $S^+(x) = \frac{1}{2}[X(x) + iY(x)]$ for our original qubits $S = 1/2$, Eq. (5), but can be readily generalized to any spin-S representations of the $\mathfrak{su}(2)$ algebra. In addition, $\mathbf{\Omega}(x)$ is a unit vector field constrained to reside on the S_2 sphere, which can thus be characterized by the polar $\theta_s(x)$ and azimuthal $\phi_s(x)$ angles at each space-time point.

An important difference with respect to the aforementioned field and momentum basis is that the coherent states are not orthogonal, but satisfy instead

$$\langle\mathbf{\Omega}(x_1)|\mathbf{\Omega}(x_2)\rangle = e^{iS\Phi[\mathbf{\Omega}(x_1),\mathbf{\Omega}(x_2),\mathbf{e}_z]}\left(\frac{1 + \mathbf{\Omega}(x_1)\cdot\mathbf{\Omega}(x_2)}{2}\right)^S. \tag{42}$$

Here, $\Phi[\mathbf{\Omega}(x_1),\mathbf{\Omega}(x_2),\mathbf{e}_z]$ stands for the area of the spherical triangle with vertices determined by the tips of the coherent-state unit vectors and the north pole of the S_2 sphere. These scalar products appear after splitting in infinitesimal pieces the corresponding time-evolution operator (36), where the fields now evolve in the Heisenberg picture with respect to the unsourced $\lambda\phi^4$ QFT (see Appendix B). Paralleling the path-integral construction for this scalar-field theory, we introduce the resolution of the identity of the field and momentum and coherent-state basis at nearby fixed instants of time, and obtain a functional integral for the $\lambda\phi^4$ QFT coupled to Ising fields via Ising-Schwinger sources. Following Ref. [21], for each spatial point, we find that the amplitude of the above overlap contributes to the kinetic energy of a nonrelativistic particle moving along the trajectory $\mathbf{\Omega}(t,\mathbf{x})$ on the unit sphere. However, when recovering the continuum-time limit, the mass of this particle vanishes, and the trajectory depends only on the accumulated phase, Eq. (42), and the source couplings to $J(x),H_t(x)$. The latter can be obtained through the coherent-state expectation values of the Ising-Schwinger term (34), $dt\langle\mathbf{\Omega}(t,\mathbf{x}_i)|\hat{V}|\mathbf{\Omega}(t+dt,\mathbf{x}_i)\rangle \approx dt[J(t,\mathbf{x}_i)\phi_H(t,\mathbf{x}_i)2S\Omega_z(t,\mathbf{x}_i) + h_t(t,\mathbf{x}_i)2S\Omega_x(t,\mathbf{x}_i)] + \mathcal{O}(dt^2)$. In addition, the accumulated phase, Eq. (42), for the whole time evolution can be expressed as the integral of a Berry connection along the trajectory $\mathbf{\Omega}(t,\mathbf{x})$,

which is equivalent to the Aharonov-Bohm phase acquired by a test particle moving in the background gauge field generated by a monopole of charge S situated at the origin of S_2. Remarkably, for the Euclidean path integral that arises from the finite-temperature T partition function of a spin model, these trajectories must be closed $\mathbf{\Omega}(0,\mathbf{x}_i) = \mathbf{\Omega}(1/T,\mathbf{x}_i)$, and the integral of the Berry connection can then be expressed as a topological Berry phase or, equivalently, as a Wess-Zumino θ term. This term plays an important role for both Heisenberg ferromagnets [21] and antiferromagnets [146,147].

In our case, given the form of the coupling, Eq. (34), it suffices to parametrize the dynamics of the spins using coherent states along a great circle of S_2, i.e., setting $\phi_s(x) = 0$ in Eq. (42). Accordingly, the Berry connection vanishes, and there is no accumulated phase. The amplitude of propagation of the full field theory between an arbitrary pair of states in this basis finds the following path-integral representation:

$$\langle\{\varphi(x),\mathbf{\Omega}(x)\}|U_{\hat{\mathcal{V}}_J}|\{\varphi(y),\mathbf{\Omega}(y)\}\rangle$$
$$= \int_{\text{BC}} D[\varphi,\mathbf{\Omega}]\delta(\mathbf{\Omega}^2 - 1)e^{iS}. \tag{43}$$

Here, we introduce the action

$$S = \int d^D x[\mathcal{L}_0 - \mathcal{V}_{\text{int}}(\varphi) - \hat{\mathcal{V}}_J(\varphi,\mathbf{\Omega})], \tag{44}$$

where we get the Klein-Gordon Lagrangian (B4) with the $\lambda\phi^4$ interactions, Eq. (40), and an additional spin-scalar coupling

$$\hat{\mathcal{V}}_J = -J(x)2S\varphi(x)\Omega_z(x) - h_t(x)2S\Omega_x(x). \tag{45}$$

Note that the spin-scalar path integral (50) has an integration measure with a constraint that enforces the vector fields to lie on S_2, and one integrates over all possible fields consistent with (BC), namely the boundary conditions associated to the initial and final spin configurations of the asymptotic states.

In the following, we implement the constraint on the vector fields explicitly by making the following substitution on the symmetry-breaking and transverse components

$$\sigma(x) = \Omega_z(x), \quad \pi(x) = \sqrt{1 - \Omega_z^2(x)} = \sum_{\ell=0}^{\infty} g_\ell\sigma^{2\ell}(x), \tag{46}$$

where $g_\ell = (-1)^\ell\binom{\frac{1}{2}}{\ell}$, and $\binom{\alpha}{\ell} = \alpha(\alpha - 1)\cdots(\alpha - \ell + 1)/\ell!$ is the generalized binomial coefficient. Upon substitution, the action, Eq. (44) can be rewritten as a scalar-σ

model

$$S = \int d^D x \big[\mathscr{L}_0 - \mathscr{V}_{\text{int}}(\varphi, \sigma) + J_s(x)\sigma(x)\varphi(x) \big], \quad (47)$$

with a nonlinear part that includes the self-interactions of the φ field, but also those of the σ field

$$\mathscr{V}_{\text{int}}(\varphi, \sigma) = \frac{\lambda_0}{4!}\varphi^4(x) + \sum_\ell h_\ell(x)\sigma^{2\ell}(x). \quad (48)$$

Here, we define the couplings

$$J_s(x) = 2SJ(x), \quad h_\ell(x) = 2Sg_\ell h_{\text{t}}(x). \quad (49)$$

This QFT partially resembles a nonlinear σ model [148], but note that, in this case, the σ fields are nonpropagating. Nontrivial effects come from the coupling to the interacting scalar bosons, and hence the name scalar-σ model.

This coupled QFT has a global $\mathbb{Z}_2 \times \mathbb{Z}_2$ symmetry by which any of the scalar or σ fields gets inverted. In the presence of the Ising-Schwinger source term, this symmetry is reduced to $\mathbb{Z}_2$ acting simultaneously on both fields $[\varphi(x), \sigma(x)] \to [-\varphi(x), -\sigma(x)]$. Note that spontaneous symmetry breaking (SSB) of a discrete symmetry at zero temperature can take place in any dimension d, and is characterized by the appearance of a vacuum expectation value in any of the fields. This is the field-theoretic interpretation of the SSB in the effective quantum Ising model, Eq. (38), which would lead to the ferromagnetic ordered mentioned in the previous sections. In that case, SSB could occur only in the σ sector, as the scalar sector is described by free Klein-Gordon fields that do not support a nonzero vacuum expectation value. Even if the generic $\lambda_0\phi^4$ field theory can support this scalar SSB channel, we do not explore it in this paper for the reasons outlined in Sec. IV B, where we connect to trapped-ion experiments.

B. Renormalized long-range quantum Ising models

In this subsection, we start from the scalar-σ field theory, Eq. (47), and exploit functional methods to find an effective description of the unitary dynamics that governs the model of scalar $\lambda\phi^4$ fields coupled to the Ising spins.

We note that the action of the scalar-σ model, Eq. (47), is formally equivalent to the standard functional description of the self-interacting Klein-Gordon field in Eq. (B3) of Appendix B, provided that one substitutes the sources $J(x) \to J_s(x)\sigma(x)$. If we are interested in a situation where, as customarily, the scalar field evolves in time from the vacuum into the vacuum, we can then follow a similar approach as described in Appendix B to express the amplitude of propagation $\mathscr{T}_{\boldsymbol{\Omega}(y)\to\boldsymbol{\Omega}(x)} = \langle 0, \{\boldsymbol{\Omega}(x)\} | U_{\hat{\mathscr{V}}_J} | 0, \{\boldsymbol{\Omega}(y)\}\rangle$ as follows:

$$\mathscr{T}_{\boldsymbol{\Omega}(y)\to\boldsymbol{\Omega}(x)} = \int_{\text{BC}} D\sigma \frac{e^{-i\int d^D x \mathscr{V}_{\text{int}}(-i\delta_{J_s(x)\sigma(x)},\sigma(x))}\mathsf{Z}_0[J_s\sigma]}{e^{-i\int d^D x \mathscr{V}_{\text{int}}(-i\delta_{J_s(x)\sigma(x)},\sigma(x))}\mathsf{Z}_0[J_s\sigma]\big|_0},$$
$$(50)$$

where we use a short-hand notation for the functional derivatives $\delta_{J_s(x)\sigma(x)} = \delta/\delta J_s(x)\sigma(x)$, and (BC) now refers only to the initial and final configurations of the σ field, which are determined by the asymptotic spin states of the transition amplitude. Note that, in this expression, the free generating functional $\mathsf{Z}_0[J] \to \mathsf{Z}_0[J_s\sigma]$ has the same form as Eq. (11), but now describes the mediated couplings between σ fields. In addition, the self-interaction potential must include the σ field nonlinearities (48).

This expression can be treated using perturbation theory, and admits a description in terms of Feynman diagrams. Note that, in principle, the new interaction term, Eq. (48), not only includes the scalar vertex with four legs, but also all possible σ vertices involving $2n$ legs. These additional vertices could in principle combine into a wider landscape of Feynman diagrams with respect to those arising in the pure $\lambda\phi^4$ theory discussed in Appendix B, including additional insertions of the σ vertices. However, the constraints in Eq. (37), which allowed us to neglect the terms of the Magnus expansion beyond second-order, Eq. (A7), stemming from higher-order nested commutators, are equivalent to considering only Feynman diagrams with the σ vertices at tree level, i.e., neglecting the combination of the scalar and σ scattering processes in the diagrams. Accordingly, the diagrammatic description of this transition amplitude, Eq. (50), is

$$\int_{\text{BC}} D\sigma \left(1 + \frac{i}{4} \Uparrow\!\!-\!\!\bigcirc\!\!-\!\!\Downarrow + \frac{1}{8} \Uparrow\!\!-\!\!\ominus\!\!-\!\!\Downarrow + \frac{1}{8} \Uparrow\!\!-\!\!\bigcirc\bigcirc\!\!-\!\!\Downarrow + \frac{1}{12} \Uparrow\!\!-\!\!\bigcirc\!\!-\!\!\Downarrow - \frac{i}{4!} \Uparrow\!\!-\!\!\rightarrow\!\!-\!\!\Downarrow - \frac{1}{12} \Uparrow\!\!-\!\!\ominus\!\!\rightarrow\!\!-\!\!\Downarrow - \frac{1}{32} \Uparrow\!\!-\!\!\ominus\!\!-\!\!\Downarrow - \frac{1}{16} \Uparrow\!\!-\!\!\ominus\!\!-\!\!\Downarrow + \cdots \right) \tilde{\mathsf{Z}}_0.$$
$$(51)$$

This equation should be read as follows: the Ising-Schwinger source terms, proportional to the σ fields, are depicted by arrows $\Uparrow = J_s(x)\sigma(x)$ to represent the

underlying spins at different space-time locations x. The blobs $\bullet = \lambda_0$ stand for interaction vertices with the bare quartic coupling. Solid lines that join an arrow and a

blob should be translated into $\times\!\!-\!\!\bullet = \Delta_{m_0}(x - z)$, and thus involve the free Feynman propagator of the scalar field, Eq. (10), from the point x of the σ field to the self-interaction vertex at z. Likewise, solid lines connected to the same blob stand for interaction loops that should be translated for $\bullet\!\!\bigcirc = \Delta_{m_0}(0)$, while those connecting two distant blobs must be substituted by the scalar-field propagator between the corresponding space-time points $\bullet\!\!-\!\!\bullet = \Delta_{m_0}(z_1 - z_2)$. For each of the above diagrams, we should integrate over all possible space-time locations of the sources $\int d^D x_i$, and those of the intermediate interaction vertices $\int d^D z_i$.

Note that the arrows in Eq. (51) are drawn in different directions to emphasize that, contrary to the standard Schwinger sources, the dynamics of which is fixed externally, the new Ising-Schwinger sources involve σ fields with their own dynamics. In particular, from the perspective of Sec. II B on the free Klein-Gordon field coupled to Ising spins, we know that there are boson-mediated processes where the spins, when initialized in a particular basis, can be flipped dynamically. Additionally, if the transverse field is nonzero, there will be quantum fluctuations that will also flip the spins in a different basis. Our choice of alternating directions of the arrows $\Uparrow, \Rightarrow, \Downarrow, \Leftarrow$, thus tries to depict this inherent spin dynamics. Additionally, in Eq. (51), the free generating functional should be substituted for $\mathsf{Z}_0[J_s\sigma] \to \tilde{\mathsf{Z}}_0[J_s\sigma, h_\ell]$, which now includes the Ising-Schwinger sources and the tree-level σ vertices

$$\tilde{\mathsf{Z}}_0 = e^{-(1/2)\int d^D x_1 \int d^D x_2 J_s(x_1)\sigma(x_1)\Delta_{m_0}(x_1 - x_2)\sigma(x_2)J_s(x_2) + i\int d^D x \sum_\ell h_\ell \sigma^{2\ell}(x)}. \tag{52}$$

The graphical representation in terms of Feynman diagrams and $\tilde{\mathsf{Z}}_0$ in Eq. (51) then has a clear interpretation. Distant Ising spins can virtually excite the bosonic field via the source coupling, and effectively interact by a long-range coupling mediated by the exchange of a virtual scalar boson, Eq. (52). Additionally, these spins are also subjected to quantum fluctuations captured by the nonlinearities of the σ vertices, Eq. (52). The Feynman diagrams, Eq. (51), show that this virtual exchange process is not entirely captured by the free terms, Eq. (52), as the scalar field also has self-interactions, and the mediating boson may get scattered through various processes as it propagates between the spins, as depicted in the upper inset of Fig. 2.

In addition to modifying the interactions between pairs of spins, Eq. (52), self-interactions introduce further possibilities where $2n$ spins also get effectively coupled. In the fifth diagram of Eq. (51), we show that a 4-spin interaction can occur by the action of two Ising-Schwinger sources that virtually excite a pair of bosons, which then scatter into another pair of bosons that carry the interactions to a different pair of spins. Note that these two-boson mediated processes also allow for further scattering of the carriers due to the self-interaction of the scalar field, as described by the following diagrams of Eq. (51) and depicted in the upper inset of Fig. 3.

We can turn this qualitative explanation of the mediated interactions into a quantitative analysis by handling the perturbative series in analogy to our exposition of Appendix B. From now onwards, for our spin $S = 1/2$ case, we make no distinction between the bare and spin sources since $J_s(x) = J(x)$. The amplitude of propagation between two different σ-field configurations can be written in a condensed form that considers all of the scattering processes of the bosonic carriers mentioned above. In summary, these scattering events lead to additive and multiplicative renormalizations of the bare mass $m_0 \to m_r$, and the bare coupling strength $\lambda_0 \to \lambda_r$. As discussed in Appendix B, using the power series of the self-energy $\Sigma(k) = \Sigma(0) + k^2 \partial_{k^2}\Sigma(k)|_{k^2=0} + \cdots$ to second order in the coupling strength, one can obtain the so-called tadpole and sunrise contributions to $\Sigma_{m_0,\lambda_0}(0) = \Sigma_{m_0,\lambda_0}^{(1,\mathrm{td})} + \Sigma_{m_0,\lambda_0}^{(2,\mathrm{td})} + \Sigma_{m_0,\lambda_0}^{(2,\mathrm{sr})}$, namely

$$\Sigma_{m_0,\lambda_0}^{(1,\mathrm{td})} = \frac{\lambda_0}{2}\int_{k_1} \tilde{\Delta}_{m_0}(k_1),$$

$$\Sigma_{m_0,\lambda_0}^{(2,\mathrm{td})} = -i\frac{\lambda_0^2}{4}\int_{k_1}\int_{k_2} \tilde{\Delta}_{m_0}^2(k_1)\tilde{\Delta}_{m_0}(k_2),$$

$$\Sigma_{m_0,\lambda_0}^{(2,\mathrm{sr})} = -i\frac{\lambda_0^2}{6}\int_{k_1}\int_{k_2} \tilde{\Delta}_{m_0}(k_1)\tilde{\Delta}_{m_0}(k_2)\tilde{\Delta}_{m_0}(k_1 + k_2), \tag{53}$$

as well as the sunrise contribution to the wave-function renormalization $z_{m_0,\lambda_0}^{-1} = 1 - \partial_{k^2}\Sigma(k)|_{k^2=0}$, namely

$$\left.\frac{\partial\Sigma^{(2,\mathrm{sr})}}{\partial k^2}\right|_0 = \frac{\lambda_0^2}{6}\int_{k_1}\int_{k_2} \tilde{\Delta}_{m_0}(k_1)\tilde{\Delta}_{m_0}(k_2)\tilde{\Delta}_{m_0}^2(k_1 + k_2). \tag{54}$$

Accordingly, to leading order, the renormalized mass reads

$$m_r^2 = \left[m_0^2 + \Sigma_{m_0,\lambda_0}(0)\right] z_{m_0,\lambda_0}, \tag{55}$$

whereas the source functions become

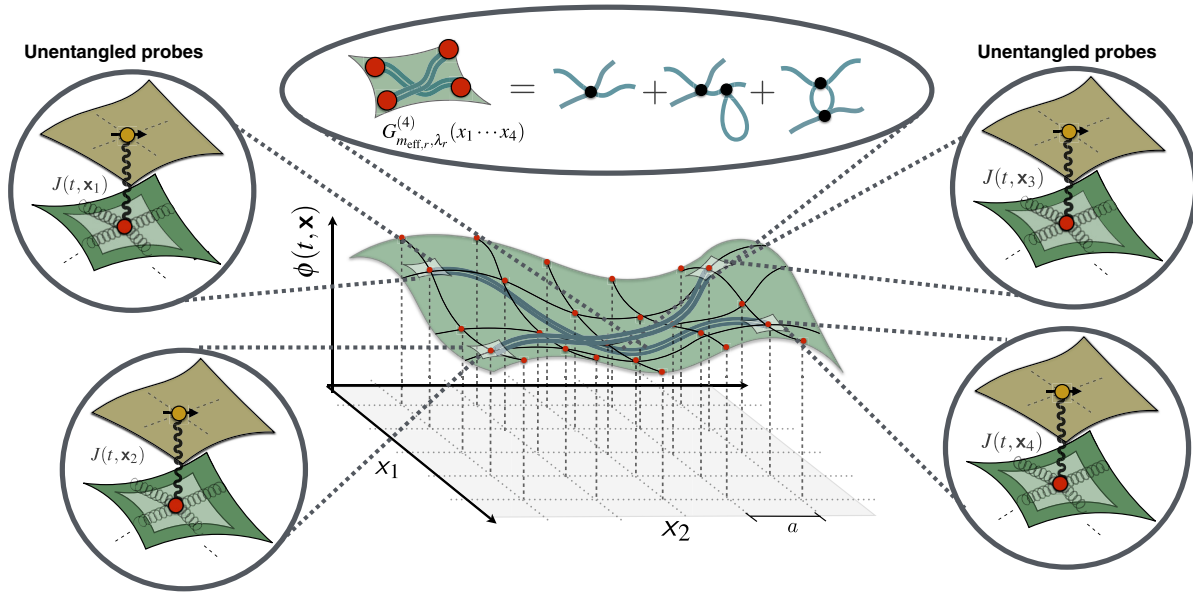$$J_r(x) = J(x)\sqrt{z_{m_0,\lambda_0}}. \tag{56}$$

FIG. 3. Scheme of the 4-spin interactions for the harmonic sensors: four distant Ising spins at positions $\mathbf{x}_1, \cdot, \mathbf{x}_4$ are coupled to the real scalar field $\phi(t, \mathbf{x})$ locally by harmonic Ising-Schwinger sources $J(t, \mathbf{x}_i) \propto \sin(\omega_J t - \mathbf{k}_J \cdot \mathbf{x}_i)$. As a result, there are 4-spin Ising interactions mediated by the scalar bosons, the strength of which will be related to a connected four-point propagator. In the upper inset, we show that in the presence of quartic couplings, these interactions will include all possible scattering events that involve two incoming and two outgoing virtual bosons, together with internal loops due to the self-interaction vertices.

Finally, the interaction strength also gets renormalized due to the last diagram of Eq. (51), leading to

$$\lambda_r = \left(\lambda_0 - i\frac{3\lambda_0^2}{2}\int_{k_1}\tilde{\Delta}_{m_0}^2(k_1)\right)z_{m_0,\lambda_0}^2. \tag{57}$$

With these renormalizations, the amplitude of propagation in Eq. (51) can thus be compactly rewritten as

$$\mathscr{T}_{\mathbf{\Omega}(y)\to\mathbf{\Omega}(x)}$$
$$= \int_{\mathrm{BC}} D\sigma\, e^{-(1/2)\int d^{2D}x J_r(x_1)\sigma(x_1)\Delta_{m_r}(x_1-x_2)\sigma(x_2)J_r(x_2)-(i/4!)\int d^{4D}x J_r(x_1)J_r(x_2)\sigma(x_1)\sigma(x_2)G_{m_r,\lambda_r}^{(4,c)}(x_1\cdots x_4)\sigma(x_3)\sigma(x_4)J_r(x_3)J_r(x_4)+i\int d^D x \sum_\ell h_\ell \sigma^{2\ell}(x)},$$
$$\tag{58}$$

where we readily identify the quadratic and quartic long-range interactions of the σ fields mediated by the scalar bosons. Note that, as discussed in Appendix B, one could consider higher-order terms in the external sources, which would introduce $2n$-spin interactions with $n \geq 3$.

We now argue that, among all the possible boson-mediated interactions for harmonic Ising-Schwinger sources, Eq. (20), which include these $2n$-spin interactions, all but the 2-spin couplings will be negligible. Since the source amplitude gets renormalized $\mathsf{J}_0 \to \mathsf{J}_{0,r}$ via Eq. (56), the renormalized harmonic Ising-Schwinger sources read

$$J_r(x) = \mathsf{J}_{0,r}\sin(k_J x) = \mathsf{J}_{0,r}\sin(\omega_J t - \mathbf{k}_J \cdot \mathbf{x}). \tag{59}$$

To estimate the strength of the $2n$-spin interactions, we recall our discussion of Sec. II B, and the importance of tuning the sources below resonance to avoid dissipative processes where propagating bosons instead of virtual ones get excited. The nonresonance condition is now renormalized $\omega_J \lesssim m_r \lesssim \omega_{\mathbf{k},r} = (\mathbf{k}^2 + m_r^2)^{1/2}$. As discussed in the free case, the source couplings should also be constrained by Eq. (60) to effectively decouple the dynamics of the Ising and scalar fields. This leads to a unitary evolution where the only nontrivial part was encoded in the Ising Hamiltonian (23). The renormalized version of the constraint (60) reads

$$\mathsf{J}_{0,r} \ll (\omega_{\mathbf{k},r} - \omega_J)d^d\mathsf{k} < (\omega_{\mathbf{k},r} + \omega_J)d^d\mathsf{k}, \tag{60}$$

which guarantees that the backaction of the Ising spins onto the $\lambda\phi^4$ field is negligible and that, if initialized in the vacuum (or any other state), the scalar field will remain in such a vacuum during the whole evolution. The discussion of Sec. II B then proceeds by performing explicitly the time integrals involving the harmonic sources in the forward and backward directions of the Feynman propagator. As a result of these integrations and the coupling constraint (60), one can neglect rapidly oscillating terms, and describe the evolution unitary by a time-independent effective Hamiltonian (23). We see in Eq. (24) that the long-range spin-spin coupling scales with $\mathbf{J}_0 \cdot \mathbf{J}_0 / (\omega_{\mathbf{k}} - \omega_J)(\omega_{\mathbf{k}} + \omega_J)$, which is already small according to the constraint (60). Hence, the dynamical effects of these interactions can only be observed by letting the system evolve for sufficiently long times. For the current renormalized equations (58), we get a similar behavior, and one can check that the additional 4-σ term in Eq. (58) also contributes to the time-independent Hamiltonian, but this time with 4-spin interactions that scale with terms like $\mathbf{J}_{0,r} \cdot \mathbf{J}_{0,r} \cdot \mathbf{J}_{0,r} \cdot \mathbf{J}_{0,r} / (\omega_{\mathbf{k}_1,r} \pm \omega_J)(\omega_{\mathbf{k}_2,r} \pm \omega_J)(\omega_{\mathbf{k}_3,r} \pm \omega_J)(\omega_{\mathbf{k}_4,r} \pm \omega_J)$. These terms should be integrated over in momentum space with a total momentum conservation, and will lead to spin interactions between four distant spins with some specific long-range coupling. In any case, Eq. (60) shows that these 4-spin interactions will be negligible in comparison to the 2-spin terms, and more so if one considers higher-order $2n$-spin interactions for $n \geq 3$.

Once arrived at this point, the last step is to convert the leading contribution to the amplitude of propagation from the path-integral formulation (58) onto a canonical time-evolution operator, reversing the steps of the path-integral construction. Altogether, when considering that the Ising spins occupy only a certain spatial arrangement, Eq. (35), we arrive at the final result: the full time evolution can be represented by the two concatenated unitaries in Eq. (19), where the nontrivial dynamics of the Ising spins is controlled by a renormalized long-range quantum Ising Hamiltonian

$$H_{\text{eff},r} = \frac{1}{2} \sum_{i=1}^{n} \sum_{j=1}^{n} J_{ij}^r \, Z(\mathbf{x}_i) Z(\mathbf{x}_j) - h_{\text{t}} \sum_{i=1}^{n} X(\mathbf{x}_i). \quad (61)$$

Here, the spin-spin couplings have a range that is controlled by the dimensionally reduced Euclidean propagator

$$J_{ij}^r = -2J_{0,r} G_{m_{\text{eff},r}}^E (\mathbf{x}_i - \mathbf{x}_j) \cos\left[\mathbf{k}_J \cdot (\mathbf{x}_i - \mathbf{x}_j) \right] J_{0,r}, \quad (62)$$

with an effective renormalized mass given by

$$m_{\text{eff},r}^2 = m_r^2 - \omega_J^2. \quad (63)$$

Therefore, tuning the frequency ω_J of the harmonic source, Eq. (59), closer to, or further from, the renormalized mass

m_r of the scalar bosons, one will be able to control the range of the Ising interactions, and extract the information about the renormalization of the scalar field using the sensing method of Sec. II B. Let us recall again that this mass gets additive and multiplicative renormalizations, Eq. (55), from all the intermediate scattering events, Eq. (51), of the bosons mediating the Ising interaction. We finally note that the spin-spin couplings scale with the square of the source amplitudes $J_{0,r}$, and that these terms also get a multiplicative renormalization described in Eq. (56). Typically, for the decoupled $\lambda\phi^4$ QFT, such source renormalizations do not have any physical consequence, as one is ultimately interested in the renormalized propagators. The generating functional in these cases is a mathematical tool, and it suffices to take functional derivatives with respect to these new sources, or directly assume that the sources couple to the renormalized fields. In contrast, for the current spin-scalar model, the renormalization of the sources has an impact on the strength of the spin-spin couplings, which is relevant as these control the timescale of the spin dynamics.

Considering Eq. (61) and our previous discussions, the new sensing protocol that monitors the real-time oscillations of a pair of Ising spins coupled to the $\lambda\phi^4$ QFT will allow us to recover the renormalized parameters of the field theory. Once we have them, one can reconstruct the generating functional in Eq. (B23), in this case to second order in the sources

$$\mathsf{Z}[J_r] = e^{-(1/2) \int d^D x_1 \int d^D x_2 J_r(x_1) \Delta_{m_r}(x_1 - x_2) J_r(x_2)}. \quad (64)$$

We note that, if the timescales of the ever-present experimental noise on the qubits is sufficiently low, it may also be possible to devise schemes that sense the effect of the 4-spin (generally $2n$-spin) interactions, gaining access to higher-order propagators and the renormalized quartic coupling.

We close this section by noting that we have not mentioned any ultraviolet (UV) cutoff of the QFT so far, although it is implicit in the discretized drawings of Figs. 1–3. Such a cutoff is not required for the results presented in Sec. II on the effective Ising models mediated by free Klein-Gordon bosons. In this case, the only UV diverging quantity is the zero-point energies of the fields. However, as soon as $\lambda\phi^4$ interactions are included, a different kind of UV divergence appears, as we see that the renormalizations involve certain Feynman diagrams, such as the tadpole term in Eq. (53), which includes the propagator at infinitesimally short distances $\Delta_{m_0}(0)$ and thus displays such UV divergences. The QFT thus needs to be regularized by the introduction of a cutoff

$$|k^\mu| \leq \Lambda_c. \quad (65)$$

As a consequence, the renormalized parameters (55)–(57) will depend on the cutoff scale. The central result of the

renormalization group is that the bare coupling constants of the QFT, m_0, λ_0, J_0 in this case, will flow with the cutoff scale and give rise to physical renormalized quantities $m_r, \lambda_r, J_{0,r}$ that no longer depend on the arbitrary cutoff. As we discuss below, in certain situations, this UV cutoff is not arbitrary but fixed by the physical system at hand (e.g., physical lattice). In this case, the renormalization group allows us to extract the universal long-wavelength properties, and find a predictive field theory valid at low energies [149]. We discuss this in more detail in the following section.

IV. RENORMALIZATION OF SOUND IN TRAPPED-ION CRYSTALS

In this section, we present a detailed discussion on how the previous results can be applied to a long-wavelength description of crystals of atomic ions confined in radiofrequency traps. This description can be formalized within the framework of the theory of elasticity for the quantized sound waves of crystals, which is reviewed in Appendix C, where we also comment on the main obstacles for a solid-state implementation of the Ising-Schwinger sensing scheme introduced in this work. We show in Sec. IV A that the transverse sound waves of harmonic trapped-ion crystals subjected to state-dependent forces offer a neat realization of the massive Klein-Gordon field coupled to Ising spins. This allows us to apply the results of Sec. II B, connecting the predicted long-range Ising models with previous works on phonon-mediated spin-spin interactions between trapped ions. This clarifies the distance dependence of the latter, and shows that our theory is a valid long-wavelength description of trapped-ion crystals under state-dependent forces. In Sec. IV B, we abandon the harmonic limit by approaching a structural phase transition of the ion crystal, where nonlinear effects lead to scattering of the quanta related to the sound waves, namely the phonons, and requires us to use the renormalization predictions of Sec. III B. In particular, in Sec. IV C, we use an explicit integration of the renormalization-group flow equations in the limit of small quantum fluctuations to predict the renormalization of the range of the Ising spin-spin interactions. We conclude in Sec. IV D by showing that additional parametric modulations of the trap frequencies can give a knob to control the amount of quantum fluctuations, exploring regimes that go beyond the previous perturbative predictions, where the results of the proposed QS would be very interesting.

A. Harmonic trapped-ion crystals: rigidity, massive Klein-Gordon fields, and effective Ising models

In this section, we discuss the realization of the previous ideas using crystals of trapped atomic ions [53]. Clouds of singly ionized atoms can be confined in finite regions of space for hours or days using storage rings or Penning and Paul traps [150]. These traps are held inside ultrahigh vacuum chambers, and additionally shielded from external fluctuating fields, such that one can explore quantum many-body properties of the ion cloud in a pristine and controlled environment. In this way, one can observe the plasmalike behavior of large thermal clouds [151], or focus on ions in medium- to small-sized clouds. In the latter context, crucial progress in our understanding of laser cooling during the past decades [152–156] has allowed the development of various techniques [157] to reach ever-lower temperatures. At these ultracold temperatures, the ions crystallize as a result of the competition between trapping and Coulomb forces [158–162], leading to the so-called Coulomb clusters and crystals [151].

In the following, we focus on linear Paul traps, a type of radiofrequency trap that confines the ions in stable linear configurations along the trap symmetry axis [160]. These kinds of traps have been exploited, among other things, for the manipulation of individual quantum systems [163], the development of frequency standards based on optical clocks [93], and the demonstration of various quantum-computing algorithms [13–15]. In this configuration, the microscopic description of a single trapped ion [164], or its extension to a collection of them [165], shows how slow secular vibrations with a typical timescale set by the inverse of the trap frequencies $\{\omega_\alpha\}_{\alpha=x,y,z}$ get decoupled from a fast driven motion synchronous with the external radiofrequency field $\Omega_{\rm rf} \gg \omega_\alpha$.

For the ion crystal, the long-wavelength description of the collective secular dynamics [166] resembles the elastodynamical theory of phonons in a one-dimensional (1D) solid-state crystal, as reviewed in Appendix C, albeit with important differences that we now stress. On the one hand, while strict 1D crystals are thermodynamically unstable, the ion chains are dynamically driven inhomogeneous clusters of ions, such that there is no conflict with the spontaneous breakdown of translational symmetry in static situations [167–169]. However, due to the separation of timescales mentioned above, the much slower secular motion can be discussed using static equilibrium tools. Secondly, whereas 1D crystals can only support compressional longitudinal waves (C1), ions in a Coulomb chain can vibrate in both longitudinal and transverse directions with respect to the trap axis. One of the key advantages of trapped-ion crystals with respect to the solid state is that these different vibrations can be selectively cooled or excited by controlling both the frequency and the propagation direction of additional laser beams. This contrasts the typical situation in solids, where a macroscopic thermal strain excites all modes simultaneously. The last key difference with respect to the elastodynamical description of sound waves in solids of Appendix C is that, contrary to the screened interatomic potentials of solids, which are in accordance with the form of the coarse-grained stress forces, trapped-ion crystals are subjected to long-range

Coulomb potentials. These long-range forces will lead to important differences in the context of the present work. Additionally, trapped ions allow one to tune the analog of the bulk and shear moduli K_e, μ_r, which characterize the stiffness and rigidity of the crystal to external strain and, in turn, determine the effective speeds of sound as discussed in the Appendix in Eqs. (C1) and (C4). More importantly, trapped-ion crystals allow to control microscopically the importance of nonelastic corrections, providing a neat route to explore renormalized Ising interactions mediated by $\lambda\phi^4$ fields, as discussed in the following subsection.

Let us start by describing in detail the first differences, which can already be understood by inspecting the trapped-ion chain in the secular harmonic approximation [170,171], and the realization of phonon-mediated Ising-type interactions thereof [34,172], making contact with Sec. II. In the secular approximation, there is a competition between the harmonic trapping potential and the Coulomb repulsion such that, for $\omega_x \ll \omega_y, \omega_z$, the N trapped ions arrange in equilibrium positions $\mathbf{x}_i = x_i \mathbf{e}_x$ along the trap symmetry axis [see Fig. 4(a)]. The position of each ion can thus be expressed as $\mathbf{r}_i(t) = x_i \mathbf{e}_x + \sum_\alpha u_{i,\alpha}(t)\mathbf{e}_\alpha$, where $u_{i,\alpha}(t)$ represents the small local vibrations around equilibrium of the ith ion along the αth axis, which can be considered as a discretized version of the displacement field $u_\alpha(t, \mathbf{x})$ introduced in the coarse-grained elasticity theory, Eq. (C1). In a harmonic approximation, one expands the overall potential to second order, and finds that the dynamics of the ion chain can be described by a Hamiltonian of local harmonic oscillators with long-range couplings

$$H_h = \sum_{i,\alpha} \left(\frac{1}{2}m_a(\partial_t u_{i,\alpha})^2 + \frac{1}{2}\kappa^\alpha u_{i,\alpha}^2 \right.$$
$$\left. + \frac{1}{4}\sum_{j\neq i}\kappa_{i,j}^\alpha \left(u_{i,\alpha} - u_{j,\alpha}\right)^2 \right). \quad (66)$$

Here, m_a is the mass of the atomic ions, and

$$\kappa_{i,j}^z = -\frac{e^2}{4\pi\epsilon_0}\frac{1}{|x_i - x_j|^3} = \kappa_{i,j}^y = -\frac{1}{2}\kappa_{i,j}^x, \quad (67)$$

can be understood as interatomic spring constants with a dipolar decay due to the net charge of the ions. In addition,

$$\kappa^\alpha = m_a\omega_\alpha^2, \quad (68)$$

is an effective spring constant leading to an elastic local force that aims at restoring the equilibrium, i.e., $\mathbf{u}_i = \mathbf{0}, \forall i$.

Let us note that the elasticity theory of Appendix C relies on the short-range character of the interatomic forces. In the solid state, this is typically modeled by restricting the interatomic springs to nearest neighbors along the chain $\kappa_{i,j}^x \to \kappa_{i,i+1}^x$, and setting $\kappa^x = 0$ as there is no additional trapping potential [173,174]. Note that, in order
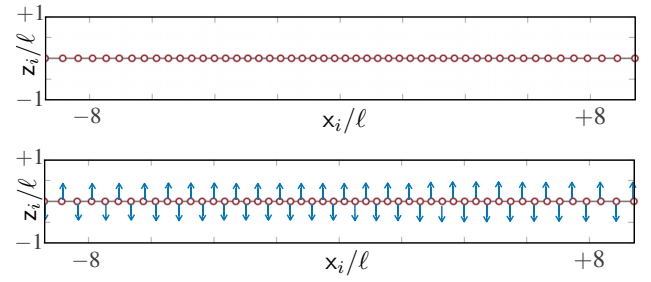

FIG. 4. Trapped-ion chain and effective Ising couplings: (a) equilibrium positions for a chain of $N = 50$ ^{171}Yb$^+$ ions confined in a Paul trap with secular frequencies $\omega_x/2\pi = 0.1$ MHz, and $\omega_z/2\pi = 3.75$ MHz. The microscopic length scale corresponds to $\ell = 12.7$ μm in this case, while the minimum distance at the bulk of the ion chain is $a = 4.4$ μm. (b) The blue alternating arrows depict the lowest vibrational mode in the transverse branch, the zigzag mode.

to describe a stable crystalline configuration, the nearest-neighbor couplings must be positive in this case $\kappa_{i,i+1}^x > 0$. For the Coulomb chain, Eq. (66), the situation is richer, as the nonzero local spring constants $\kappa^\alpha > 0$ allow for stable configurations with both attractive and repulsive elastic couplings $\kappa_{i,j}^\alpha \gtrless 0$. The attractive and repulsive character can be understood by considering that the ion excursions from equilibrium induce distant electric dipoles $\mathbf{P}_i = \mathbf{u}_i, \mathbf{P}_j = \mathbf{u}_j$. These dipoles interact by repelling (attracting) each other when aligned orthogonal (parallel) to the axis of separation, here the x axis, yielding $\kappa_{i,j}^y, \kappa_{i,j}^z > 0$ ($\kappa_{i,j}^x < 0$). This has a direct consequence for the collective vibrational branches, as the lowest longitudinal vibration will correspond to all dipoles lying in parallel, which requires the ions to vibrate in phase and leads to the so-called center-of-mass mode [166]. On the other hand, the lowest transverse vibrations correspond to alternating dipoles along the y,z axis, such that the ions vibrate out of phase and lead to the so-called zigzag mode [see Fig. 4(b)]. For reasons that will become clear below, we restrict to the transverse vibrations along the z axis in a situation where the corresponding trapping potential has been partially relaxed $\omega_x < \omega_z \ll \omega_y$.

We can now address the connection of this microscopic theory, Eq. (66), to a Klein-Gordon field theory, Eq. (1), at long wavelengths or, equivalently, low energies. As noted above, the lowest-energy transverse vibration will correspond to out-of-phase displacement of the ions, which can be associated to a quasimomentum $k_s = \pi/a$. Here, a is a characteristic microscopic length scale of the Coulomb chain [166] that will be proportional to the combination of microscopic parameters

$$\ell = (e^2/4\pi\epsilon_0 m_a\omega_x^2)^{1/3}. \quad (69)$$

Although we could carry on in the most generic situation [53], in order to make a more direct contact with the scalar

QFT of the previous sections, we assume that the ions are homogeneously distributed in the chain $\mathsf{x}_i = ia$ with inter-ion distance, i.e., lattice spacing, a set by the minimum distance between the bulk ions [see Fig. 4(a)]. This sets directly the aforementioned microscopic length scale, which turns out to be $a \lesssim \ell$. The homogeneous approximation is valid for the bulk of the ion crystal, neglecting the differences due to inhomogeneities as one approaches the chain edges [151], which is consistent with the spirit of our long-wavelength theory. We thus apply periodic boundary conditions, and leave a numerical study of the inhomogeneous chain to the end.

As is customary in other long-wavelength descriptions of condensed-matter problems [175,176], one proceeds by separating fast and slow variations of the degrees of freedom of interest [53,177,178]. The transverse displacement around the zigzag distortion contains a rapidly oscillating part, the amplitude of which varies much slower, such that

$$u_{j,\mathsf{z}}(t) = a e^{-ik_s \mathsf{x}_j}\tilde{\phi}(t,\mathsf{x}), \quad \partial_t u_{j,\mathsf{z}}(t) = \frac{1}{m_a}e^{-ik_s \mathsf{x}_j}\tilde{\pi}(t,\mathsf{x}), \tag{70}$$

where $\tilde{\phi}(t,\mathsf{x})$ is the slowly varying component that will play the role of the scalar field in the continuum $\mathsf{x}_j \to \mathsf{x}$, and $\tilde{\pi}(t,\mathsf{x})$ is its conjugate momentum. These operators are defined in a way that one recovers equal-time commutation relations in the continuum limit $[\tilde{\phi}(t,\mathsf{x}_i), \tilde{\pi}(t,\mathsf{x}_j)] = i\hbar\delta_{i,j}/a \to i\hbar\delta(\mathsf{x} - \mathsf{x}')$, corresponding to the canonical commutator of the scalar field defined below Eq. (1) for natural units. Note that, however, we need to work in SI units as we have not yet identified the quantity that will play the role of the speed of light. Accordingly, we must rescale the fields through a canonical transformation to achieve the correct scaling dimensions of the Klein-Gordon model, which for $D = 1 + 1$ dimensions is

$$\phi(t,\mathsf{x}) = \frac{1}{\sqrt{m_a a}}\tilde{\phi}(t,\mathsf{x}), \quad \pi(t,\mathsf{x}) = \sqrt{m_a a}\tilde{\pi}(t,\mathsf{x}). \tag{71}$$

Since the field varies slowly, one proceeds by performing a gradient expansion to capture the long-wavelength physics

$$\phi(t,\mathsf{x}_j) \approx \phi(t,\mathsf{x}_i) + (\mathsf{x}_j - \mathsf{x}_i)\hat{\nabla}_{\mathsf{x}_i}\phi(t,\mathsf{x}_i) + \cdots, \tag{72}$$

where we introduce the discretized derivative

$$\hat{\nabla}_{\mathsf{x}_i}\phi(t,\mathsf{x}_i) = \frac{\phi(t,\mathsf{x}_{i+1}) - \phi(t,\mathsf{x}_i)}{a}. \tag{73}$$

As a consequence of this gradient expansion, the long-range terms, Eq. (66), contribute effectively to nearest-neighbor couplings, and lead to a clear similarity with the solid-state harmonic crystal discussed above. As becomes clear below, the long-range couplings should decay sufficiently fast such that the corresponding series obtained

by summing over all neighbors converges, and the truncated gradient expansion is thus meaningful. This procedure improves upon the so-called phononlike approximation [171], where one truncates the dipolar tail to nearest neighbors without a previous gradient expansion, and thus yields an incorrect speed of sound. Although there exist other methods to obtain a more accurate dispersion relation at long wavelengths [170,171], the current gradient expansion is likely the simplest and most economic.

Substituting the expressions in Eqs. (70)–(72) in the Coulomb-chain Hamiltonian (66), we find that the vibrations along the transverse z axis can be described by

$$H_h = a\sum_{\mathsf{x}\in\Lambda_s}\frac{1}{2}\left(\frac{c_{\mathrm{t}}^2\pi^2(t,\mathsf{x})}{K^2\hbar^2} + K^2\hbar^2[\hat{\nabla}_{\mathsf{x}}\phi(t,\mathsf{x})]^2\right.$$
$$\left. + m_0^2 c_{\mathrm{t}}^2 K^2\phi^2(t,\mathsf{x})\right), \tag{74}$$

where Λ_s stands for the positions of the ions in the chain, and we introduce the parameters

$$c_{\mathrm{t}} = \omega_{\mathsf{x}}a\sqrt{\frac{\ell^3}{a^3}\log 2}, \quad m_0 = \frac{\hbar\omega_{zz}}{c_{\mathrm{t}}^2}, \quad K = \frac{m_a a c_{\mathrm{t}}}{\hbar}, \tag{75}$$

where the zigzag mode frequency reads

$$\omega_{zz}^2 = \omega_{\mathsf{z}}^2 - \frac{7}{2}\zeta(3)\omega_{\mathsf{x}}^2\frac{\ell^3}{a^3}, \tag{76}$$

and we make use of the Riemann ζ function

$$\zeta(z) = \sum_{r=1}^{\infty}\frac{1}{r^z}. \tag{77}$$

The physical interpretation of these parameters is now given. In the continuum limit, one gets $a\sum_{\mathsf{x}\in\Lambda_s} \to \int d\mathsf{x}$, such that the term inside the parenthesis of Eq. (74) can be identified with a Hamiltonian density. After a canonical rescaling $\phi(x) \to \phi(x)/K$, $\pi(x) \to K\pi(x)$, this Hamiltonian density can be derived from $\mathscr{L}_{\mathrm{KG}} = \frac{1}{2}(\hbar^2\partial_\mu\phi\partial^\mu\phi - m_0^2 c_{\mathrm{t}}^2\phi^2)$, which is the Klein-Gordon Lagrangian density in SI units. Hence, one clearly sees that c_{t} plays the role of an effective speed of light, and m_0 of an effective bare mass. To understand the role of the dimensionless parameter K, we need to use a different normalization of the fields, Eq. (71), such that the canonical algebra is $[\phi(t,\mathsf{x}_i), \pi(t,\mathsf{x}_j)] = i\delta_{i,j}/a \to i\delta(\mathsf{x} - \mathsf{x}')$, the scalar field is dimensionless, and its conjugate momentum has units

of inverse length. This is achieved by the transformation $\phi(x) \rightarrow \phi(x)(c_t/K\hbar)^{1/2}$, $\pi(x) \rightarrow \hbar\pi(x)(K\hbar/c_t)^{1/2}$, which, in the massless limit $m_0 = 0$, leads to the Hamiltonian density $\mathcal{H}_{CB} = (\hbar c_t/2)[(1/K)\pi^2 + K(\nabla\phi)^2]$. Note that, in this case, this Hamiltonian density corresponds to the field theory of a conformal boson with Tomogana-Luttinger parameter K [21]. This parameter appears in the treatment of strongly correlated 1D models [179,180], where various gapless phases of matter arising from very different microscopic models [181–183] share fundamental properties with the ground state of the Tomonaga-Luttinger model [184,185]. This leads to the concept of the Tomonaga-Luttinger liquid [186], where, regardless of the nature of the fundamental constituents, the relevant low-energy excitations are bosonic particle-hole pairs with a long-wavelength description in terms of this conformal boson QFT with additional local interactions: the so-called sine-Gordon model [187]. Due to the very nature of these interactions, the boson field can be compactified on a circle with a radius that depends on the Tomonaga-Luttinger parameter $R = 1/\sqrt{4\pi K}$, which, in turn, controls the power-law decay of two-point functions of the original microscopic degrees of freedom [188]. In the present situation, the additional local interactions in the trapped-ion crystal shall not be those of the sine-Gordon model [187], such that there is no reason to compactify the scalar field. Moreover, as the original degrees of freedom are already a discretized version of the bosonic field, the Luttinger parameter will not appear in the two-point functions. In fact, one can readily see that this parameter does not modify the Heisenberg equations of motion of the scalar field, and will thus not appear in the dispersion relation. In spite of this, as discussed in the following subsection, the Tomonaga-Luttinger parameter plays an important role in the presence of $\lambda\phi^4$ interactions, controlling the amount of quantum fluctuations in the structural phase transition of the ion crystal. However, prior to that, let us give some additional insight on the microscopic expressions for c_t, m_0, and K.

The effective speed of light c_t can also be derived from a coarse-grained elastodynamical theory of the ion crystal. As discussed around Eq. (C4) of the Appendix, deformations with shear strain lead to sound waves that do not alter the length of chain, but describe shape deformations. The speed of such transverse sound waves can be expressed in terms of the crystal density ρ and the shear modulus μ_r through

$$c_t = \sqrt{\frac{\mu_r}{\rho}}. \tag{78}$$

In this case, the shear modulus measures the rigidity of the ion chain to changes to its linear shape, as opposed to the compression and expansion that would be described by the bulk modulus and lead to longitudinal sound waves.

Within this gradient expansion, the shear modulus reads

$$\mu_r = \frac{1}{2a} \sum_{j \neq i} \kappa_{i,j}^z |x_j - x_i|^2 \cos(k_s|x_j - x_i|)$$

$$= m_a \omega_x^2 a \frac{\ell^3}{a^3} \log 2, \tag{79}$$

where, in the last equality, we take the thermodynamic limit $N \rightarrow \infty$, substituted $k_s|x_j - x_i| = \pi|j - i|$, and summed the corresponding series $\sum_{r=1}^{\infty}(-1)^r/r = -\log 2$. Within this homogeneous approximation, the mass density of the ion chain is $\rho = m_a/a$, and the transverse speed of sound

$$c_t = \sqrt{\frac{e^2}{4\pi\epsilon_0} \frac{\log 2}{m_a a}}, \tag{80}$$

which leads directly to the corresponding expression in Eq. (75), upon using the length scale in Eq. (69).

Let us now derive the expression for the bare mass or, equivalently, the Compton wavelength ξ_0 associated to these massive scalar bosons. By multiplying the first and third terms in Eq. (74) and, likewise, in the trapped-ion Hamiltonian (66), we find the following expression:

$$\xi_0^{-2} = \frac{m_0^2 c_t^2}{\hbar^2}$$

$$= \frac{1}{c_t^2}\left[\omega_z^2 - \sum_{j \neq i} \frac{2\kappa_{j,i}^z(-1)^{j-i}}{m_a} \sin^2\left(\frac{1}{2}k_s|x_j - x_i|\right)\right]. \tag{81}$$

Once again, taking the thermodynamic limit in the homogeneous bulk for the ion chain, we find

$$\xi_0 = a\frac{\omega_x}{\omega_{zz}}\sqrt{\frac{\ell^3}{a^3}\log 2}, \tag{82}$$

where the zigzag mode frequency, Eq. (76), is obtained by summing the series $\sum_{r=1}^{\infty}[1 - (-1)^r]/r^3 = 7\zeta(3)/4$. This Compton wavelength, Eq. (82), will be a key quantity below, and leads directly to the bare mass of Eq. (75).

Let us now give a physical interpretation of the Tomonaga-Luttinger parameter. First of all, the conformal boson is a self-dual QFT under the transformation $\pi(x) \leftrightarrow \phi(x)$, $K \leftrightarrow 1/K$, such that the definition of the Tomonaga-Luttinger parameter as K or K^{-1} depends on convention. We follow the choice in Refs. [21,53], although we note that it is also customary to take the inverse convention in condensed matter [176,180]. Also note that the normalization of the fields may differ, and one often finds definitions $K \rightarrow K/2\pi$ [189]. For these different choices, one can relate the Tomonaga-Luttinger parameter to the

sound speed and the thermal compressibility of a 1D harmonic chain [190,191]. With our current convention, and considering the transverse nature of the trapped-ion displacements, this relation would involve the rigidity modulus instead

$$c_{\mathrm{t}} K = \frac{\mu_r a^2}{\hbar}, \tag{83}$$

which leads to the corresponding parameter of Eq. (75).

Being proportional to the shear modulus, the Tomonaga-Luttinger parameter is thus a measure of the rigidity of the ion chain to shear deformations. As discussed in more detail in the following section, given the current microscopic interpretation in terms of shear rigidity, it is not surprising that the Tomonaga-Luttinger parameter gets renormalized by additional anharmonicities. Indeed, prior to the canonical rescaling mentioned below Eq. (74), the coarse-grained Lagrangian of the ion chain would be $\mathscr{L}_{\mathrm{KG}} = (K^2/2)[\hbar^2 \partial_\mu \phi \partial^\mu \phi - m_0^2 c_{\mathrm{t}}^2 \phi^2]$, which can be readily identified with our discussion of the wave-function renormalization for the $\lambda \phi^4$ theory in the Appendix below Eq. (B16). The difference here is that, for the trapped-ion chain, the Tomonaga-Luttinger parameter can be interpreted as a wave-function renormalization $K^2 \leftrightarrow z_\phi^{-1}$ that occurs already in the free theory, and is a consequence of the underlying rigidity of the ion chain. From this perspective, it is not surprising that this rigidity gets renormalized by anharmonicities, which gives a physical interpretation of the field-theoretic multiplicative renormalizations, Eq. (56), due to the sunrise Feynman diagram. Indeed, such "noninteracting multiplicative renormalizations" are directly taken care of by the parameter definition of the coarse-grained theory, Eq. (74).

Let us now present an alternative account of these results that will be useful later. Since the harmonic trapped-ion Hamiltonian (66) is quadratic, one can derive an exact description of the collective vibrational branches in the homogeneous limit by a simple Fourier transform [174]. The collective-mode frequencies for transverse z vibrations are

$$\omega^2(\mathsf{k}) = \omega_{\mathsf{z}}^2 + \sum_{j \neq i} \frac{2}{m_a} \kappa_{j,i}^{\mathsf{z}} \sin^2\left(\frac{1}{2}\mathsf{k}|x_j - x_i|\right), \tag{84}$$

where the momentum belongs to the first Brillouin zone BZ $= \{\mathsf{k} = (2\pi/Na)n : n \in \mathbb{Z}_N\}$. In the thermodynamic limit, the exact dispersion relation is expressed in terms of the Riemann ζ function and the series representation of the polylogarithm

$$\mathrm{Li}_n(z) = \sum_{r=1}^{\infty} \frac{z^r}{r^n}, \tag{85}$$

where $z \in \mathbb{C}$ and the radius of convergence is $|z| \leq 1$ [125]. In the present case, the polylogarithms are evaluated

at the N roots of unity to yield the following dispersion relation:

$$\omega^2(\mathsf{k}) = \omega_{\mathsf{z}}^2 + \omega_{\mathsf{x}}^2 \frac{\ell^3}{a^3} \left[2\zeta(3) - \mathrm{Li}_3\left(e^{ika}\right) - \mathrm{Li}_3\left(e^{-ika}\right)\right]. \tag{86}$$

One can now Taylor expand the polylogarithms around the lowest-energy mode for the transverse vibrations $\mathsf{k}a \approx \pi + \delta \mathsf{k}a$ for $|\delta \mathsf{k}| \ll \pi/a$, to find

$$\omega^2(\delta \mathsf{k}) \approx \omega_{\mathsf{z}}^2 - \omega_{\mathsf{x}}^2 \frac{\ell^3}{a^3} \left(\frac{7}{2}\zeta(3) - (\delta \mathsf{k}a)^2 \log 2\right)$$

$$= \frac{m_0^2 c_{\mathrm{t}}^4}{\hbar^2} + c_{\mathrm{t}}^2 \delta \mathsf{k}^2, \tag{87}$$

where one obtains the same expressions for the effective speed of light and Compton wavelength as in Eqs. (80) and (82), respectively. As already advanced above, the dispersion relation gives us no information about the Tomonaga-Luttinger parameter, which can be either extracted from the gradient expansion, or using the above relationship $c_{\mathrm{t}} K = \mu_r a^2/\hbar = c_{\mathrm{t}}^2 m_a a/\hbar$. It is interesting to note that, while the longitudinal vibrational modes for a harmonic crystal with dipolar couplings do not lead to a well-defined sound speed $\omega_{\delta \mathsf{k}}^2 \approx |\mathsf{k}|^2 \log|\mathsf{k}|$ [174], the transverse sound speed of the ion crystal is perfectly valid, Eq. (103), due to the repulsive nature of the harmonic couplings, Eq. (66), and the out-of-phase oscillations of neighboring ions in the lowest-energy mode. This is the underlying reason for our choice to focus on the transverse vibrations of the ions along the z axis.

We have seen that the transverse displacement of each ion can be described by a scalar quantum field discretized in a lattice formed by the positions of the ions in the Coulomb crystal. In addition, at each of these positions, we have all the electronic degrees of freedom of each ion, among which we select only a pair of energy levels $\{|0_{\mathsf{x}}\rangle = |\uparrow_{\mathsf{x}}\rangle, |1_{\mathsf{x}}\rangle = |\downarrow_{\mathsf{x}}\rangle\}$. These will typically correspond to long-lived levels in the ground- and/or metastable-state manifolds. The specific choices lead to the so-called hyperfine, Zeeman, optical, or fine-structure qubits [15], where we recall that ω_0 is the transition frequency between the two corresponding levels. Using the discretized version of the orthogonal projectors introduced around Eq. (5), $Q(t, \mathsf{x}) = |\uparrow_{\mathsf{x}}\rangle \langle\uparrow_{\mathsf{x}}| = \mathbb{I} - P(t, \mathsf{x})$, the dynamics of the internal and motional degrees of freedom is described by

$$H_0 = H_h + a \sum_{\mathsf{x} \in \Lambda_s} \delta\epsilon(\mathsf{x}) Q(t, \mathsf{x}), \quad \delta\epsilon(\mathsf{x}) = \frac{\hbar \omega_0}{a}, \tag{88}$$

where the vibrational Hamiltonian in the long-wavelength harmonic approximation corresponds to Eq. (74). According to our long-wavelength description, this system will then correspond to a scalar-σ model, Eq. (47), for $S = \frac{1}{2}$.

The coupling of the qubits to the vibrational degrees of freedom is realized by shining electromagnetic radiation into the ion crystal, which stems from additional laser or microwave sources, again depending on the chosen qubit type [15]. In order to achieve the form of the Ising-Schwinger sources, either in the $Z(x)$ basis, Eq. (17), or any other Pauli basis, one typically works in the Lamb-Dicke regime of resolved sidebands [163]. Here, one selects the propagation direction and frequency of the radiation to couple selectively to the desired vibrational branch by creating or annihilating a single phonon. The desired Ising-Schwinger sources can be achieved by using a Mølmer-Sørensen [192] or Leibfried [193] scheme, both of which generate a so-called state-dependent force that underlies the realization of multiqubit entangling gates for quantum computation [194]. For concreteness, following the discussion in the first part of this paper, we focus on Z-dependent forces and hyperfine and Zeeman qubits, but remark that similar expressions can be found for other Pauli operators depending on the qubit choice. Following the notation introduced in Ref. [53], but sticking to the use of fields in SI units, the corresponding spin-phonon coupling can be rewritten as

$$\hat{V} = a \sum_{\mathbf{x} \in \Lambda_s} \cos(\mathsf{k}_s \mathbf{x}) \frac{g}{a} \sin(\Delta\omega_L t - \Delta\mathbf{k}_L \cdot \mathbf{x}) Z(t, \mathbf{x})\phi(t, \mathbf{x}).$$
$$(89)$$

Here, $\Delta\mathbf{k}_L$ ($\Delta\omega_L$) is the wavevector (frequency) of the beat note arising from a pair of interfering laser beams, and $g = \hbar\Omega_L \Delta\mathbf{k}_L \cdot \mathbf{e}_z \sqrt{m_a a^3}$ is the coupling strength between the qubits and the scalar field, which is controlled by the two-photon Rabi frequency Ω_L [193]. By a direct comparison with the harmonic Ising-Schwinger sources introduced in Eq. (35), we directly find that the harmonic dependence of the source is fully tunable via the laser's beat note

$$\omega_J = \Delta\omega_L, \quad \mathbf{k}_J = \Delta\mathbf{k}_L. \quad (90)$$

Let us now discuss the role of the Tomonaga-Luttinger parameter. As already discussed above, in order to arrive at the corresponding expression of the Klein-Gordon QFT, we should use a canonical transformation of the fields $\phi(x) \to \phi(x)/K$, $\pi(x) \to K\pi(x)$. For a pure scalar theory, this rescaling has no effect on the dynamics, such that the Tomonaga-Luttinger parameter does not have any dynamical manifestation. However, as soon as we couple the scalar field to the Ising spins, the situation changes. Since the Tomonaga-Luttinger parameter is a measure of the harmonic internal forces that quantify the shear stress of the crystal, it does not appear directly in the bare coupling strength of the Ising-Schwinger sources, which can be understood as external sources that lead to shear strain. Note however that, under the canonical transformation of the fields mentioned above, the Ising-Schwinger sources

will get effectively rescaled by the Tomonaga-Luttinger parameter, which can be interpreted as Hook's law in disguise (i.e., strain proportional to stress) [195,196]. Considering the additional alternation due to the oscillating nature of the lowest-energy $\mathsf{k}_s = \pi/a$ vibrational mode, one finds that the amplitude of Ising-Schwinger sources is

$$J_0 \to J_0(\mathbf{x}) = -J_0 \cos(\mathsf{k}_s \mathbf{x}), \quad J_0 = \frac{g}{K}. \quad (91)$$

Hence, the Tomonaga-Luttinger parameter will appear in the strength of the boson-mediated Ising interactions, Eq. (29). This will be particularly important in the presence of nonlinearities for the sound waves. As commented in the paragraph below Eq. (83), the Tomonaga-Luttinger parameter can be understood as a noninteracting wave-function renormalization, and one will get further renormalizations when including interactions, modifying the strength of the spin-spin couplings.

Finally, to conclude with the discussion about the trapped-ion realization, the additional transverse field $H_t(x)$ in Eq. (35) can be obtained by adding another source of radiation, either from additional laser beams, or from an external microwave source, tuned in resonance with the carrier transition instead of the vibrational sidebands [163]. Altogether, the time-evolution unitary, Eq. (36), would depend on

$$\hat{V} = \sum_{\mathbf{x} \in \Lambda_s} J_0(\mathbf{x}) \sin(\Delta\omega_L t - \Delta\mathbf{k}_L \cdot \mathbf{x}) K\phi(t, \mathbf{x}) Z(t, \mathbf{x})$$
$$- h_t X(t, \mathbf{x}), \quad (92)$$

where the transverse field $h_t = \hbar\Omega_0/2 \ll \hbar\omega_0$ depends on the carrier Rabi frequency Ω_0.

According to the generic results of Sec. II, the source term, Eq. (92), will lead to Ising interactions mediated by the effective massive Klein-Gordon fields, which can be written as

$$H_{\text{eff}} = \frac{1}{2} \sum_{i=1}^{n} \sum_{j=1}^{n} J_{ij} \, Z(\mathbf{x}_i) Z(\mathbf{x}_j) - h_t \sum_{i=1}^{n} X(\mathbf{x}_i). \quad (93)$$

Here, the Ising couplings, Eq. (29), must be updated to account for the spatial modulation of the source couplings, Eq. (91), yielding

$$J_{ij} = -2J_0(\mathbf{x}_i) G_{m_{\text{eff}}}^{E}(\mathbf{x}_i - \mathbf{x}_j) \cos\left[\mathsf{k}_{J,\mathbf{x}}(\mathbf{x}_i - \mathbf{x}_j)\right] J_0(\mathbf{x}_j).$$
$$(94)$$

We recall that the decay of the interactions with the distance is controlled by the dimensionally reduced Euclidean propagator, which corresponds to $d = 1$ dimensions, Eq. (28), in this case, with an effective mass, Eq. (26), that depends on the frequency of the harmonic sources.

Note that, however, all of the expressions in Secs. II and III use natural units. In the context of trapped ions, one can translate them into SI units by exchanging the mass parameter in favor of an effective Compton wavelength $m_{\text{eff}}^2 \to \xi_{\text{eff}}^{-2} = \xi_0^{-2} - \Delta\omega_L^2/c_t^2$, such that

$$\xi_{\text{eff}} = \frac{c_t}{\sqrt{\omega_{zz}^2 - \Delta\omega_L^2}}, \tag{95}$$

where we recall that the beat note is always red detuned with respect to the transverse vibrational branch $\Delta\omega_L \lesssim \omega_{zz} = \min\{\omega(k), k \in [0, 2\pi/a]\}$. In addition, to be consistent with the SI units, the Euclidean propagator in Eq. (29) should be rescaled as $G_{m_{\text{eff}}}^E(x_1 - x_2) \to G_{m_{\text{eff}}}^E(x_1 - x_2)/\hbar^2$. We recall that these spin-spin couplings can be measured by monitoring the dynamics of an initial product state of the spins, as described around Eq. (39). There are also alternative spectroscopic techniques that also allow one to infer the spin-spin couplings by sweeping the frequency ω_m of a periodic modulation of the transverse field $h_t \to h_t + \delta h_t \sin(\omega_m t)$ [197].

We thus see that, as announced in the previous sections, the trapped-ion setup offers an ideal scenario where to apply our results for the harmonic Ising-Schwinger sources in Sec. II, and the effective Ising interactions mediated by the scalar Klein-Gordon field. In fact, following the seminal works [34,172], there have been numerous trapped-ion experiments [35,36,198–205] that have explored the physics of phonon-mediated Ising-type interactions with an increasing number of qubits. Our results indicate that the long-wavelength QFT describing these experiments in the harmonic regime is indeed the previous scalar-σ model (47) in the absence of self-interactions. This unveils the key role played by the generating functional of the massive Klein-Gordon QFT for a particular type of source: the harmonic Ising-Schwinger source, Eq. (35). This not only allows for a neat connection of recent trapped-ion experiments to the physics of relativistic QFTs, but shall also be useful in the two following aspects. On the one hand, it sheds light on the specific decay law of the spin-spin couplings for sufficiently large ion crystals, complementing the results presented in Refs. [206,207] as discussed in the following paragraph. On the other hand, the results presented in Sec. III show a very interesting path for the characterization of renormalization effects in such mediated Ising interactions, which take place when the scalar bosons are not described by free Klein-Gordon fields, but instead through a self-interacting $\lambda\phi^4$ QFT. The following two sections will present a detailed account of that situation.

Let us then finish this section by discussing the effective range of the phonon-mediated spin-spin interactions in the harmonic approximation of the trapped-ion crystal. To simplify the discussion, we orient the laser beams such that $\Delta\mathbf{k}_L \cdot \mathbf{x}_i = 0$, neglecting in this way the additional

frustration of the spin-spin couplings [208,209]. Using the explicit form of the Euclidean propagator, Eq. (32), and substituting in Eq. (29) the trapped-ion expressions of the effective speed of light and the Compton wavelength, we find

$$J_{ij} = -(-1)^{i-j} J_{\text{eff}} \frac{\xi_{\text{eff}} a^2}{\ell^3} e^{-(|x_i - x_j|/\xi_{\text{eff}})}. \tag{96}$$

Here, we define a coupling strength

$$J_{\text{eff}} = \frac{\hbar \Omega_L^2 \eta_x^2}{\omega_x} \frac{2}{\log 2}, \tag{97}$$

where $\eta_x = \Delta k_L \sqrt{\hbar/2m_a\omega_x}$ is the so-called Lamb-Dicke parameter. The crucial point is that, according to the expression of the effective Compton wavelength, Eq. (95), by controlling the detuning of the laser beat note with respect to the resonance with the lowest-energy zigzag mode $\Delta\omega_L^2 \lesssim \omega_{zz}^2$, one can control the exponential decay of the Ising interactions.

Interestingly, Eq. (96) shows the same distance dependence as the exponential tail of the spin-spin couplings derived in Ref. [206], where no reference is made to an effective QFT for the ion chain, nor to the role of the Feynman propagators or the generating functional. This agreement serves as a validation of our approach, and gives a concrete physical interpretation of the decay length ξ_{eff} in Eq. (96) as the effective Compton wavelength of the bosons. It also clarifies that the alternation in Eq. (96) is the remnant of the separation of fast and slow variations during the coarse graining, Eq. (70). We also note that Eq. (96) gives a more-accurate estimate of the exponential decay, Eq. (95), with respect to the approach of Ref. [206], since the latter uses additional approximations for both the dispersion relation and the spin-spin coupling strengths.

On the other hand, the authors of Ref. [206] identified a key aspect of systems with long-range interactions: there can be additional contributions to the spin-spin interactions due to the power-law couplings between the oscillators, Eq. (67), as also corroborated by alternative perturbative studies [207]. In order to account for these terms, we should work with the full lattice propagator in continuous time, which can be written as

$$\Delta_{m_0}^{\text{lat}}(x) = \int_{\hat{k}} \tilde{\Delta}_{m_0}^{\text{lat}}(\hat{k}) e^{-ikx}, \quad \tilde{\Delta}_{m_0}^{\text{lat}}(\hat{k}) = \frac{i}{\hat{k}^2 - \omega_z^2 + i\epsilon}, \tag{98}$$

where the lattice version of the 2-momentum is

$$\hat{k} = \left[\omega, \sum_{j \neq i} \frac{2}{m_a} \kappa_{j,i}^z \sin^2\left(\frac{1}{2} k|x_j - x_i|\right)\right], \tag{99}$$

and we use the short-hand notation $\int_{\hat{k}} = \int_{\mathbb{R}} (d\omega/2\pi)(1/N)$ $\sum_{k\in BZ}$. In the thermodynamic limit $N \to \infty$, the dimensionally reduced Euclidean lattice propagator reads

$$G^{\text{lat}}_{m_{\text{eff}}}(\mathsf{x}) = a \int_0^{2\pi/a} \frac{d\mathsf{k}}{2\pi} \; \frac{e^{i\mathsf{k}\mathsf{x}}}{\omega^2(\mathsf{k}) - \Delta\omega_L^2}. \qquad (100)$$

Here, $\omega(\mathsf{k})$ stands for the trapped-ion dispersion relation (84), which accounts for the full contribution of the long-range couplings expressed in terms of polylogarithms (86). In the expression above, we define the Brillouin zone $\mathsf{k} \in [0, 2\pi/a)$, such that the low-energy zigzag mode $\mathsf{k}_s = \pi/a$ lies exactly in the middle. The spin-spin couplings, Eq. (29), for $\Delta\mathbf{k}_L \cdot \mathbf{x}_i = 0$ read

$$J_{ij} = -\hbar\Omega_L^2 \eta_{\mathsf{x}}^2 2\omega_{\mathsf{x}} G^{\text{lat}}_{m_{\text{eff}}}(\mathsf{x}_i - \mathsf{x}_j). \qquad (101)$$

The integral of Eq. (100) can be evaluated by extending the momentum $\mathsf{k}a \to z$ to the complex plane $z = x + iy \in \mathbb{C}$. As discussed below, the properties of the lattice propagator can be understood via the analytic structure of $f(z) = 1/[\omega^2(z) - \Delta\omega_L^2]$. Note that the complex-valued dispersion relation

$$\omega^2(z) = \omega_{\mathsf{z}}^2 + \omega_{\mathsf{x}}^2 \frac{\ell^3}{a^3} \left[2\zeta(3) - \text{Li}_3(e^{iz}) - \text{Li}_3(e^{-iz}) \right], \qquad (102)$$

requires analytical continuation of the polylogarithms as one leaves the real axis, since $|e^{\pm iz}| = e^{\mp y} > 1$ lies beyond the radius of convergence of the power series, Eq. (85). Inspired by the analytical techniques underlying the Källén-Lehman spectral representation of the two-point Feynman propagator [20,210–212], we now provide a derivation of the spin-spin couplings alternative to Ref. [206]. In this spectral representation, the full propagator of an interacting QFT can be described as a sum of free propagators, which arise from either isolated single-particle poles at the renormalized mass, or from a branch-cut discontinuity that appears above a certain threshold, and represents multiparticle excitations. This situation finds a clear parallelism in our case due to the power-law couplings, as $f(z)$ contains both a pair of complex-conjugate simple poles $z_- = (z_+)^*$, and a branch cut connecting the branch point z_b of the polylogarithms at $e^{\pm iz_b} = 1$ with the point at infinity along the imaginary axis (see Fig. 5). To understand why the corresponding contributions to the spin-spin couplings are simply added, one can apply Cauchy's theorem [213] along the multiple keyhole contour γ displayed in this figure, which allows us to rewrite the complex function as follows:

$$f(z) = \frac{\mathsf{r}}{z - z_+} + \frac{\mathsf{r}^*}{z - z_-} + \int_0^\infty \frac{ds}{2\pi} \frac{\text{disc}[f(z)]}{is - z}. \quad (103)$$

Here, r, r^* are the residues of the simple poles, and $\text{disc}[f(z)] = \lim_{\epsilon\to 0^+}[f(is+\epsilon) - f(is-\epsilon)]$ is the
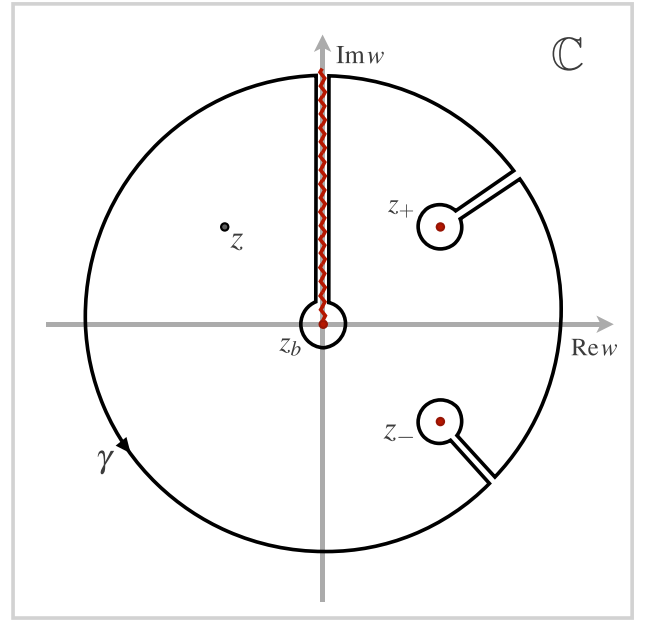

FIG. 5. Cauchy's theorem and branch-cut structure: we use Cauchy's theorem $f(z) = (1/2\pi i) \oint_\gamma dw[f(w)/(w-z)]$ for the multiple keyhole contour γ, which avoids the isolated poles and the branch cut such that the function is analytic inside. The simple poles lie at $z_\pm = \pi \pm i/\xi_{\text{eff}}$, where the effective Compton wavelength is given in Eq. (95). This describes the broadening and screening of the zigzag mode $\mathsf{k}_s a = \pi$. The residues of the poles are $\mathsf{r} = \mathsf{r}^* = \pi\xi_{\text{eff}}a/c_t^2$, where the effective speed of light is given by Eq. (80). The branch point at $ee^{iz_b} = 1$ is connected to the point at infinity by a branch cut along the positive imaginary axis, displaying a discontinuity that is calculated using the properties of the polylogarithms, leading to Eq. (103).

branch-cut discontinuity. For any short-range discretization of the scalar field, which substitutes the derivatives by finite differences that involve only a finite number of neighbors like Eq. (73), this discontinuity is absent and one gets only the contribution of the simple poles. On the other hand, for power-law couplings such as those in Eq. (67), the complex dispersion relation (102) contains polylogarithms with the branch-cut discontinuity $\text{Li}_n(e^s + i\epsilon) - \text{Li}_n(e^s - i\epsilon) = 2\pi i s^{n-1}/\Gamma(n)$ for $\epsilon \to 0^+$ and $s > 0$, where $\Gamma(n)$ is the Γ function. Considering the simplified dependence on $z \in \mathbb{C}$ of the function (103), calculating the Fourier transform in Eq. (100) that yields the spin-spin couplings, Eq. (101), becomes direct.

In the context of the Källén-Lehman representation of the two-point function of an interacting QFT at zero temperature [20], the single-particle pole would be aligned along the real axis $z_+ = z_- \in \mathbb{R}$, leading to a renormalized propagator corresponding to the term $\mathsf{r}/(z - z_+) \to i\mathsf{r}/(k^2 - m_r^2 + i\epsilon)$. The branch cut, which would also be aligned along the real axis, would start at a certain threshold above the single-particle pole where multiparticle excitations can be created by the interactions. The associated

discontinuity, which is related to the continuous part of the so-called spectral function $\rho_c(s)$, weights the contribution of each of the free Klein-Gordon propagators. These would contribute to the term $1/(z - is) \rightarrow i/(k^2 - M^2 + i\epsilon)$, and would be characterized by a mass M above the multiparticle threshold of the theory [20].

Following this analogy, the additive structure for the spin-spin couplings has the following interpretation. The isolated poles give rise to an exponentially decaying contribution, which coincides exactly with the long-wavelength result, Eq. (96). In addition, due to the branch-cut discontinuity, we get an additive contribution that can be understood as the superposition of each of the Euclidean propagators above threshold, which in this case corresponds to the imaginary semiaxis. Thanks to the use of Cauchy's theorem, Eq. (103), there is no need to identify steepest-descent directions, nor to perform any further approximations as discussed in Ref. [206], and the corresponding integral in s leads to

$$J_{ij} = J_{\text{eff}} \left((-1)^{i-j+1} \frac{\xi_{\text{eff}} a^2}{\ell^3} e^{-(|\mathbf{x}_i - \mathbf{x}_j|/\xi_{\text{eff}})} \right.$$
$$\left. + \frac{\omega_{\mathsf{x}}^4 \log 2}{(\omega_{\mathsf{z}}^2 - \Delta\omega_L^2)^2} \frac{\ell^3}{|\mathbf{x}_i - \mathbf{x}_j|^3} \right). \quad (104)$$

This expression shows that, for distances much larger than the effective Compton wavelength, Eq. (95), $|\mathbf{x}_i - \mathbf{x}_j| \gg \xi_{\text{eff}}$, the decay of the spin-spin couplings is dominated by an antiferromagnetic dipolar tail. As one approaches the resonance with the zigzag mode from below $\Delta\omega_L \rightarrow \omega_{zz}$, the contribution of the alternating exponential becomes more pronounced, and there are deviations from the dipolar decay. In Fig. 6(b), we compare these analytical predictions to the exact expression of the Ising couplings for an inhomogeneous crystal of $^{171}\text{Yb}^+$ ions. As shown in this figure, there is a clear agreement of the spin-spin couplings even for an inhomogeneous lattice spacing.

We note that using the exact expressions for the dispersion relation and the boson-mediated Ising couplings, as we do in this work, should give more accurate estimates of the spin-spin couplings, especially in the vicinity of the structural phase transition. Regardless of these quantitative details, our conclusion is the same as in Ref. [206]: although phonon-mediated Ising couplings in small trapped-ion crystals can be approximated by a power-law decay with a tunable exponent [198–204], theoretical predictions about static or dynamical effects that aim to describe the thermodynamic limit should consider that Eq. (104) is not a power-law decay with a tunable exponent [207]. Otherwise, some of the predicted phenomena, such as phase diagrams or quantum phase transitions that depend on the power-law exponent would not represent what can be explored with trapped-ion experiments.
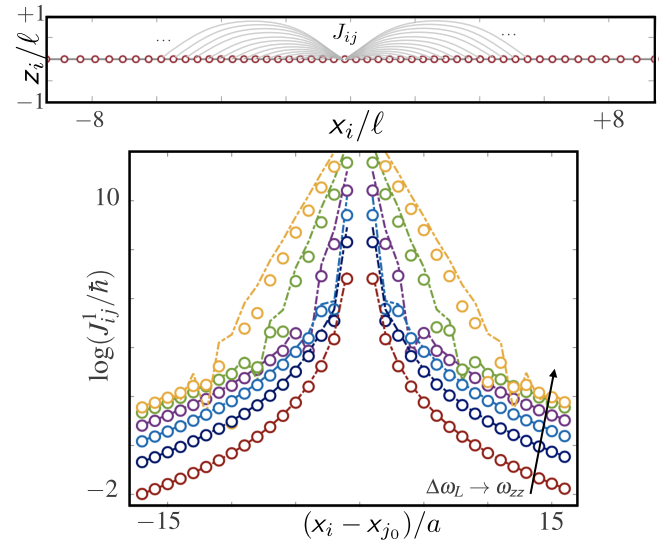

FIG. 6. Trapped-ion chain and effective Ising couplings: (a) equilibrium positions for a chain of $N = 50$ $^{171}\text{Yb}^+$ ions. The gray lines depict the long-range spin-spin couplings J_{ij}^1 between the center-most ion $j_0 = N/2$ and the rest of the chain. (b) The exact spin-spin couplings, represented by circles, are calculated from $J_{ij}^1 = |\Omega_L|^2 E_r \sum_n [\mathcal{M}_{i,n} \mathcal{M}_{jn}/(\Delta\omega_L^2 - \omega_{\mathsf{z},n}^2)]$, where $\{\omega_{\mathsf{z},n}, \mathcal{M}_{i,n}\}_{n=1}^N$ are the eigenvalues and eigenvectors obtained from the diagonalization of Eq. (66), and $E_r = \mathbf{p}_L^2/2m_a$ is the recoil energy of the ions due to the beat-note momentum $\mathbf{p}_L = \hbar\Delta\mathbf{k}_L$ [205]. We note that for the $^{171}\text{Yb}^+$ ions, the Ising interactions typically use a Mølmer-Sørensen scheme, such that the roles of the X, Z operators must be reversed. The dashed-dotted lines correspond to the coarse-grained predictions of Eq. (104) with no fitting parameter, but directly using the microscopic expressions of all the parameters derived in the main text, and substituting the homogeneous approximation $\mathbf{x}_i^0 = ia$ for the inhomogeneous positions of (a). The different curves and data correspond to different detunings of the laser beat notes with respect to the zigzag mode $(\omega_{zz} - \Delta\omega_L)/2\pi \in \{18.75, 37, 5, 93.75, 187.5, 937.5\}$ kHz.

B. Anharmonic trapped-ion crystals: $\lambda\phi^4$ fields, sound renormalization, and Ising models

The real advantage of the present approach is that it allows us to explore situations beyond the harmonic approximation of the trapped-ion crystal. Anharmonic corrections to the vibrational Hamiltonian (66) become particularly relevant in the vicinity of structural transitions for anisotropically confined ion crystals [214]. By increasing the ratio of the secular trap frequencies $\omega_{\mathsf{x}}/\omega_{\mathsf{z}}$ in the regime $\omega_{\mathsf{y}} \gg \omega_{\mathsf{z}} \gtrsim \omega_{\mathsf{x}}$, the linear configuration becomes unstable towards ladderlike structures with an increasing number of legs, which have been characterized in several experiments [209,215–219]. The first structural change between the ion chain and a so-called zigzag ladder corresponds to a second-order phase transition taking place at some critical $\omega_{\mathsf{x}}/\omega_{\mathsf{z}}|_c$, which can be described by an effective Landau model [111]. In our work, we work in

the regime $\omega_x/\omega_z \lesssim \omega_x/\omega_z|_c$, such that the linear configuration is stable, but we are sufficiently close to the structural phase transition where the anharmonic corrections become important. In the context of elasticity theory, this is the so-called yield limit, where a small increase in stress causes a large strain, and one expects large deviations from Hook's law [196]. Note that we are focusing on the vicinity of the structural phase transition, but making sure the crystal is still in the linear configuration, as the zigzag structure will be accompanied by additional excess micromotion synchronous with the rf potential of the linear Paul trap [164,165], and combining this driven motion with a coarse-grained QFT model lies beyond the scope of this work.

In the vicinity of this phase transition, the most relevant corrections $H = H_h + H_a$ to Eq. (66), coming from higher orders in the Taylor expansion of the Coulomb potential, are

$$H_a = \frac{1}{2} \sum_i \sum_{j \neq i} \frac{\beta_{i,j}^z}{4!} \left(u_{i,z} - u_{j,z}\right)^4, \qquad (105)$$

where we introduce the anharmonic coupling strengths

$$\beta_{i,j}^z = \frac{e^2}{4\pi\epsilon_0} \frac{9}{|\mathsf{x}_i - \mathsf{x}_j|^5}. \qquad (106)$$

One now proceeds with the substitution of the gradient expansion in SI units, Eqs. (70) and (71), to ultimately find that the long-wavelength anharmonic corrections to the massive Klein-Gordon QFT, Eq. (74), corresponds to a quartic self-interaction

$$H_a \approx a \sum_{\mathsf{x} \in \Lambda_s} \frac{1}{4!} \lambda_0 K^4 \phi^4(t, \mathsf{x}). \qquad (107)$$

Let us note that the canonical rescaling $\phi(x) \to \phi(x)/K$, $\pi(x) \to K\pi(x)$ yields the standard $\lambda\phi^4$ QFT in SI units

$$H = a \sum_{\mathsf{x} \in \Lambda_s} \frac{1}{2} \left[\left(\frac{c_t^2}{\hbar^2} \pi^2(x) + \hbar^2 [\hat{\nabla}_\mathsf{x}\phi(x)]^2 + m_0^2 c_t^2 \phi^2(x) \right) \right.$$
$$\left. + \frac{\lambda_0}{4!} \phi^4(x) \right], \qquad (108)$$

where we introduce the quartic coupling

$$\lambda_0 = 8 \frac{m_a^2}{K^4} \sum_{j \neq i} \beta_{j,i}^z \sin^4\left(\frac{1}{2} \mathsf{k}_s |\mathsf{x}_j - \mathsf{x}_i|\right), \qquad (109)$$

which reads as follows in the thermodynamic limit:

$$\lambda_0 = \frac{279\zeta(5)}{2K^4} m_a^3 \omega_x^2 \ell^3. \qquad (110)$$

Once we derive the complete coarse-grained theory, and find the microscopic trapped-ion expressions of the bare

parameters in Eqs. (75), (90), (91), and (109), we can directly apply the results of Sec. III to understand how the dynamics of the Ising spins changes due to the leading anharmonicities of the ion crystal in the vicinity of the structural phase transition. As concluded around Eq. (61), the main contribution to the dynamics can still be described by the long-range quantum Ising model, Eq. (93), but one must consider renormalized spin-spin couplings

$$J_{ij}^r = -2J_r(\mathsf{x}_i) G_{m_{\text{eff},r}}^E (\mathsf{x}_i - \mathsf{x}_j) J_r(\mathsf{x}_j), \qquad (111)$$

with renormalized sources, Eq. (91), and an effective renormalized mass that flows with the quartic coupling, Eq. (63). As discussed in Sec. III, all these renormalizations account for the various scattering processes of the phonon mediating the interactions, as it propagates between the two distant spins, Eq. (51).

In order to connect to the perturbative calculations of Sec. III, which use natural units, we recall that the effective-mass term m_{eff} should be substituted by an inverse length scale related to the Compton wavelength $1/\xi_{\text{eff}} = m_{\text{eff}} c_t / \hbar$ in SI units, Eq. (95). Likewise, in natural units, the renormalization equations (57) indicate that the coupling constant λ_0 has natural dimension $d_{\lambda_0} = 4 - D = 2$. Hence, it should be substituted by a combination of SI parameters $\lambda_0, \hbar, c_t$ that carries units of inverse length squared. In the present case, this leads to

$$\frac{\lambda_0 c_t}{\hbar^3} = \frac{a^{-2}}{K} \frac{279\zeta(5)}{2\log 2}. \qquad (112)$$

Accordingly, we can use the perturbative equations (55)–(57) by substituting $\lambda_0 \to \lambda_0 c_t/\hbar^3$, as well as $m_{\text{eff}}^2 \to m_{\text{eff}}^2 c_t^2/\hbar^2$. However, we face the problem that was already alluded to in connection to interacting QFTs: these perturbative corrections introduce UV divergences, which must be dealt with by means of the renormalization group (RG). In the present trapped-ion context, these divergences are an artefact of our coarse-grained description, and will always be regularized by the physical UV cutoff due to the underlying lattice

$$|\mathsf{k}| \leq \Lambda_c = \frac{\pi}{a}, \quad |k^0| \leq c_t \frac{\pi}{a}. \qquad (113)$$

Note that this equation coincides exactly with Debye's cutoff in solid-state crystals discussed in Eq. (C5) of the Appendix, since the length of the 1D crystal would be $L = Na$ when a is the lattice spacing. The goal of the renormalization group is then not to deal with infinities, but to extract the universal features of the renormalized theory, Eq. (29), that will not depend on short wavelengths on the order of the lattice spacing a, but describe instead length scales $\xi \gg a$. We deal with these RG predictions in the following section.

C. Rigidity and renormalization-group predictions

The typical starting point of the Wilsonian RG [106,149] is the normalization factor N in Eq. (B3). After a Wick rotation $\tau = it$, this factor can be interpreted as the partition function $N \to Z$ of a model of statistical mechanics in a higher spatial dimension $D = d + 1$, where the free energy corresponds to the QFT action, Eq. (B3), in imaginary time, the so-called Euclidean action. This partition function displays the same renormalization of the microscopic couplings g_i, together with the aforementioned UV divergences, as those discussed in Sec. B via the normalized generating functional. The key idea of the RG is that, after regularizing these divergences by introducing a UV cutoff Λ_c, the microscopic couplings will flow in the larger parameter space of all possible couplings of the theory $\{g_i(\Lambda_c)\}$, the so-called theory space. This flow occurs as one lowers the cutoff in order to focus on the low-energy or infrared (IR) behavior [106,220]. A quantitative description of this RG flow can be obtained by first performing a coarse-graining step on the partition function, where one integrates out the high-energy modes at the cutoff scale $k \in [\Delta_c/s, \Delta_c]$ for some parameter $s > 1$. After such a coarse graining, a second RG step consists of rescaling the momenta and fields in order to compare the original partition function Z with the coarse-grained one, extracting how the microscopic parameters run with the cutoff, and

finding differential equations for the RG flow [106,149]. Given our focus on the normalized generating functional in this work, as it is the key quantity to understand the effective Ising dynamics for the full model of $\lambda\phi^4$ fields coupled to spins, Eq. (58), we revisit this RG procedure using the results of Appendix B and Sec. III B.

Let us start by discussing the first RG step. From now on, we set natural units $\hbar = c_t = 1$, keeping in mind our previous discussion to connect the results to the SI trapped-ion units. After the Wick rotation, we can define the space-time points and wave vectors as follows: $\mathbf{x} = (it, \mathbf{x})$ and $\mathbf{k} = (-ik^0, \mathbf{x})$, which are $D = 2$ Euclidean vectors. In the absence of the Ising spins, one can calculate the perturbative expansion of the full generating functional (B5) by separating the slow $\varphi_<(x)$ and fast $\varphi_>(x)$ field components

$$\varphi_<(x) = \int_0^{\Lambda_c/s} \frac{d^2k}{(2\pi)^2} e^{-i\mathbf{k}\cdot\mathbf{x}}\varphi(\mathbf{k}),$$

$$\varphi_>(x) = \int_{\Lambda_c/s}^{\Lambda_c} \frac{d^2k}{(2\pi)^2} e^{-i\mathbf{k}\cdot\mathbf{x}}\varphi(\mathbf{k}), \quad (114)$$

where the scalar product is now Euclidean. The diagrammatic expansion in the absence of Ising spins in Eq. (B6) can be rewritten in Euclidean time as follows:

$$(115)$$

where we see that some of the factors preceding the diagrams change sign, and all become real. Additionally, we note that the lines now stand for the free Euclidean propagator

$$\Delta_{m_0}^E(\mathbf{x}) = \int_{\mathbf{k}} \tilde{\Delta}_{m_0}^E(\mathbf{k}) e^{-i\mathbf{k}\cdot\mathbf{x}},$$

$$\tilde{\Delta}_{m_0}^E(\mathbf{k}) = \frac{1}{\mathbf{k}^2 + m_0^2} =: \tilde{\Delta}_{m_0,\mathbf{k}}^E, \quad (116)$$

such that, for slow components (solid lines), the momentum integrals extend to $|\mathbf{k}| \in [0, \Lambda_c/s]$, whereas for fast components (dashed lines), they extend to a small annulus around the UV cutoff $|\mathbf{k}| \in [\Lambda_c/s, \Lambda_c]$. Note that the ellipsis in Eq. (115) now contains, in addition to higher-order terms in the interaction strength, also Feynman diagrams that involve other combinations of slow and fast components, e.g., tree level diagrams with only fast-mode propagators. However, the current combinations in Eq. (115) suffice to understand the RG flow, as they capture the effect

that the coarse-grained over fast modes within the annulus around the cutoff will have on the slow modes, and thus on the low-energy IR theory.

As discussed around Eq. (B7), the additional scattering terms, Eq. (115), lead to an effective generating functional in which the bare parameters get renormalized. In this case, such a renormalization is a result of the coarse graining over fast modes, such that the dressed parameters now become cutoff dependent. For instance, the bare mass $m_0^2 \to m_0^2 + \delta m_0^2$ changes due to the tadpoles and sunrise mass renormalization of the fast modes similarly to Eq. (55), namely

$$\delta m_0^2 = \frac{\lambda_0}{2} \int_{\mathbf{k}_1}^f \tilde{\Delta}_{m_0,\mathbf{k}_1}^E$$

$$\times \left[1 - \lambda_0 \int_{\mathbf{k}_2}^f \left(\frac{1}{2}\tilde{\Delta}_{m_0,\mathbf{k}_1}^E + \frac{1}{3}\tilde{\Delta}_{m_0,\mathbf{k}_1+\mathbf{k}_2}^E\right)\tilde{\Delta}_{m_0,\mathbf{k}_2}^E\right], \quad (117)$$

where the integrals restricted to momenta of the fast modes, as indicated by $\int_{\mathbf{k}}^{f} = \int_{(\Lambda_c/s)<|\mathbf{k}|<\Lambda_c} |\mathbf{k}|(d|\mathbf{k}|/2\pi)$. Likewise, the interaction strength changes according to $\lambda_0 \to \lambda_0 + \delta\lambda_0$, where

$$\delta\lambda_0 = -\frac{3\lambda_0^2}{2} \int_{\mathbf{k}_1}^{f} \left(\tilde{\Delta}_{m_0,\mathbf{k}_1}^{E}\right)^2. \tag{118}$$

The next RG step is to rescale the variables and fields, recovering the original cutoff. In this way, the resulting partition function or, in this case, the generating functional can be compared to the original one, such that the flow in theory space can be extracted. At this step, the sunrise diagram and the wave-function renormalization, Eq. (B16), leading to the multiplicative mass and source renormalizations, Eq. (56), come into play

$$\mathbf{k} \to \mathbf{k}' = s\mathbf{k}, \quad \varphi(\mathbf{k}) \to \varphi(\mathbf{k}'s^{-1}) = s^2 z_{m_0,\lambda_0}^{-1} \varphi'(\mathbf{k}'), \tag{119}$$

where the integrals are again restricted to the fast modes

$$z_{m_0,\lambda_0}^{-1} = 1 + \frac{\lambda_0^2}{6} \int_{\mathbf{k}_1}^{f} \tilde{\Delta}_{m_0,\mathbf{k}_1}^{E} \int_{\mathbf{k}_2}^{f} \left(\tilde{\Delta}_{m_0,\mathbf{k}_1+\mathbf{k}_2}^{E}\right)^2 \tilde{\Delta}_{m_0,\mathbf{k}_2}^{E}. \tag{120}$$

After this rescaling, one can obtain the total running of the microscopic couplings in theory space. The only step left is to extract the system of differential equations for infinitesimal coarse-graining $s = e^{\delta\ell} \approx 1 + \delta\ell$. This allows us to approximate the above Euclidean integrals, and leads to

$$\frac{dm_0^2}{d\delta\ell} = 2m_0^2 + \frac{\lambda_0}{4\pi} \frac{\Lambda_c^2}{\Lambda_c^2 + m_0^2},$$

$$\frac{d\lambda_0}{d\delta\ell} = 2\lambda_0 - \frac{3\lambda_0^2}{4\pi} \frac{\Lambda_c^2}{(\Lambda_c^2 + m_0^2)^2}. \tag{121}$$

Up to this point, the discussion parallels the standard RG treatment of the $\lambda\phi^4$ QFT based on the partition function [106,149]. For the $D = 2$ case, these RG equations are not very informative, as both couplings are relevant already at tree level (i.e., they grow exponentially as one approaches long wavelengths). Indeed, any self-interacting term φ^{2n} with $n \geq 3$ will also be relevant, bringing us away from the Gaussian fixed point $(m_0, \lambda_0) = (0, 0)$.

We note that the Tomonaga-Luttinger parameter of the original low-energy description, Eq. (74), does not seem to play any role in the RG treatment, as we have rescaled the fields to get the standard QFT, Eq. (108). Note, however, that this parameter is proportional to the shear modulus of the ion crystal, and thus quantifies how rigid the system is. Accordingly, the effect of the quantum fluctuations introduced by the canonically conjugate momentum

operators in Eq. (74) will be inversely proportional to the Tomonaga-Luttinger parameter. As neatly discussed in Ref. [221], even if the above RG equations (121) do not contain information about the nonperturbative fixed point that controls the scaling of the phase transition (i.e., the $D = 2$ analog of the Wilson-Fisher fixed point for $D = 4 - \epsilon$); they can determine how the classical critical point $m_0^2|_c = 0$ changes with the strength of the quartic interactions towards $m_0^2(\lambda_0)|_c \neq 0$ when quantum fluctuations are very small. Following Ref. [221], quantum fluctuations are controlled by a dimensionless effective Planck's constant

$$\tilde{\hbar} = \frac{\hbar}{m_a \omega_{\mathsf{x}} a^2} = \frac{\sqrt{(\ell^3/a^3)\log 2}}{K}, \tag{122}$$

which we find to be inversely proportional to the Tomonaga-Luttinger parameter. For the crystal of $^{171}\mathrm{Yb}^+$ ions (see Fig. 4), $K = 1.3 \times 10^5$ and quantum fluctuations are thus highly suppressed $\tilde{\hbar} = 3.1 \times 10^{-5}$. Since the quartic-interaction parameter in SI units, Eq. (112), is proportional to $K^{-1} \propto \tilde{\hbar} \ll 1$, the flow equations (??) can be rewritten in a way that the dependence on quantum fluctuations becomes apparent. In particular, linearizing them around $m_0^2 = 0$ allows the prediction of how this classical critical point changes as a function of the quantum fluctuations. To make contact with our previous exposition of the trapped-ion problem, we rewrite this result in terms of the Luttinger parameter and use SI units for the interaction strength, Eq. (112), such that

$$\left.\frac{m_0^2 c_\mathsf{t}^2}{\hbar^2}\right|_c = \frac{279\zeta(5)}{16\pi K a^2 \log 2} \left(\log K - \log K^*\right). \tag{123}$$

Here, K^* is a nonuniversal parameter that can be extracted from the numerical results of Ref. [221] via Eq. (122), such that $K^* \approx 58.98$ for the $^{171}\mathrm{Yb}^+$ crystal. We note that this is a nonuniversal property, unlike the scaling behavior of the structural phase transition, which is controlled by a nonperturbative fixed point that, due to symmetry considerations, must be in the universality class of the 2D Ising model [222].

With this perturbative RG prediction, we can analyze how the boson-mediated Ising interactions will change due to the quartic interactions. In particular, their decay, Eq. (104), is controlled by the effective Compton wavelength of the bosons in the coarse-grained theory before the dipolar tail takes on. Since the classical critical point moves according to Eq. (123), the effective Compton wavelength can still be described by Eq. (95) if we substitute $\omega_{\mathsf{zz}}^2 \to \omega_{\mathsf{zz}}^2 + \delta\omega_{\mathsf{zz}}^2$, where

$$\delta\omega_{\mathsf{zz}}^2 = \omega_{\mathsf{x}}^2 \frac{\ell^3}{a^3} \frac{279\zeta(5)}{16\pi K a^2} \left(\log K - \log K^*\right) \tag{124}$$

includes the renormalization of the bare parameters due to the quartic interactions. We now make the following two

remarks. On the one hand, the combination of this shift with the scaling of Eq. (95) is consistent with the scaling properties of the Gaussian fixed point. We know, on the other hand, that the correlation length should be controlled by the Ising universality class, in which case the scaling will differ. In any case, since the correction in Eq. (124) turns out to be rather small (i.e., $\sqrt{\delta\omega_{zz}^2}/\omega_{zz} = 2.5 \times 10^{-3}$ for the $^{171}\text{Yb}^+$ crystal of Fig. 6), it will be very challenging to probe these differences experimentally, which is a result of the very large rigidity of the ion crystal and the suppressed quantum fluctuations. In the last section of this paper, we discuss how this rigidity could be controlled by introducing additional parametric drivings of the crystal that allow one to tune the value of the shear modulus and, in turn, lower the Tomonaga-Luttinger parameter.

D. Parametric drivings to control the shear modulus

In this section, we discuss how the shear rigidity and, in turn, the Tomonaga-Luttinger parameter can be controlled by introducing a fast parametric modulation of the transverse trap frequency ω_z. As discussed in Ref. [223], the transverse modes of the harmonic ion crystal are rather special in the sense that the total number of local vibrational excitations of the ions is a conserved quantity for the timescales of interest. This is a consequence of the microscopic parameters in Eq. (66), which fulfil $\hbar|\kappa_{ij}^z|/4m_a\omega_z \ll 2\hbar\omega_z$. Accordingly, one can treat the local vibrations as particles tunneling between neighboring ions, and explore experimentally their propagation along the Coulomb crystal, as realized in various recent experiments [224–231]. Moreover, the corresponding tunneling amplitude can be controlled by Floquet engineering via periodic modulations [232], mimicking situations considered for electrons in solids [233] and beyond [234,235]. In the present context, we consider a site-dependent parametric modulation of the trap frequency

$$\omega_z \to \omega_z + \omega_d\eta_i \cos(\omega_d t), \tag{125}$$

where ω_d is the parametric driving frequency, and $\eta_i = i\Delta\eta$ is a relative modulation amplitude that increases linearly along the ion chain. We consider the fast-modulation regime, such that the aforementioned tunneling gets dressed in analogy to what occurs for electrons in solids [233]. For the transverse vibrations, this effect can in turn be recast as a dressing of the shear modulus, Eq. (79), of the ion crystal

$$\tilde{\mu}_r \approx \frac{1}{2a}\sum_{j\neq i}\kappa_{i,j}^z|x_j - x_i|^2 \cos(k_s|x_j - x_i|)\mathfrak{J}_0\big[\Delta\eta(j-i)\big], \tag{126}$$

where we introduce the zeroth Bessel function of the first kind $\mathfrak{J}_0(x) \approx \sqrt{2/\pi x}\cos[(\pi/4) - x]$ for $x \gg 1$. This

approximation requires $\hbar|\kappa_{i,j}^z|/4m_a\omega_z \ll \hbar\omega_d, \hbar\omega_z$, where $\omega_d \neq \omega_z$, where corrections due to rapidly rotating terms will be vanishingly small, and the main contribution of the parametric drivings is the dressing of the shear modulus, Eq. (126).

Note that this parametric dressing can even change the sign of the tunneling [233], inverting the band structure, and changing the role of the zigzag mode. This can be avoided in the present context, ensuring that the dressed rigidity $\mu_r > 0$, by working with modulations $\Delta\eta \in (5.3, 9)$, as depicted in Fig. 7. This figure shows that the dressed rigidity can achieve much smaller values for $\Delta\eta \gtrsim 5.3$, or $\Delta\eta \lesssim 9$. Accordingly, both the transverse speed of sound and the Tomonaga-Luttinger parameter, Eq. (75), can be reduced considerably, such that the ion crystal is less rigid and the effect of quantum fluctuations will become more important at the expense of a slower transverse speed of sound. For instance, for $\Delta\eta = 5.33$, we would get $K \approx 3.2 \times 10^3$, effectively reducing the Tomonaga-Luttinger parameter by 2 orders of magnitude.

In contrast, in this regime $\hbar|\kappa_{i,j}^z|/4m_a\omega_z \ll \hbar\omega_d \neq \hbar\omega_z$, the bare mass of the scalar bosons and the quartic coupling, Eq. (110), would get no appreciable dressing as they are purely local terms. Accordingly, the effective range of the Ising spin-spin interactions in the harmonic limit of the crystal are still described by Eq. (95), and can thus be controlled by setting the frequency of the state-dependent force closer or further from the zigzag mode, taking into account the flow of the classical critical point, Eq. (123), due to the quartic interactions. Since this shift scales with $\log K/K$, the dressing scheme will amplify the effects of the quartic interactions, making the corresponding change in ξ_{eff} more amenable to be measured experimentally. Note, however, that including the specific parametric modulation, Eq. (125), may require the use of microfabricated trap electrodes in the spirit of Ref. [231], or global modulations, such as those stemming from ac-Stark shifts [209,234] that
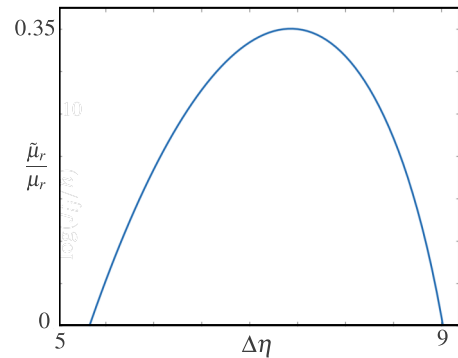

FIG. 7. Dressed shear modulus: ratio of the dressed shear modulus, Eq. (126), and the original shear modulus, Eq. (79), of the parametrically driven crystal of $^{171}\text{Yb}^+$ ions, as a function of the relative modulation amplitude $\Delta\eta$ in Eq. (125).

will lead to similar dressing effects in the long-wavelength description of the ion chain. Therefore, although the effect of the quartic interactions is amplified by reducing the rigidity of the crystal, the experimental complexity also increases.

V. CONCLUSIONS AND OUTLOOK

We have presented a new perspective on a protocol for the interferometric sensing, Eq. (12), of the generating functional of a scalar QFT [53], which clarifies the role of the interactions between the quantum sensors mediated by the scalar bosons, Eq. (16), and the requirement of multipartite entanglement in the initial state. This has allowed us to propose a new simplified sensing scheme, which uses unentangled probes that are coupled to the scalar field via always-on harmonic sources, Eq. (20), and which evolve under an effective quantum Ising model with long-range couplings, Eq. (29), controlled by a dimensionally reduced Euclidean propagator of the scalar field, Eq. (28). In the presence of self-interactions, these Ising spin-spin interactions are mediated by virtual $\lambda\phi^4$ bosons that can also scatter. This regime can be explored using functional-integral methods by means of a scalar-σ model, Eq. (47) and a diagrammatic expansion, Eq. (51), which shows that this additional scattering leads to renormalizations of the spin-spin couplings between the sensors, and further $2n$-spin interactions (58). In the regime of interest, we have argued that the real-time dynamics is dominated by a renormalized quantum Ising model, where the pairwise interactions get additive and multiplicative renormalizations, Eqs. (55)–(57).

These formal results find a natural application for $D = 1 + 1$ dimensions in the physics of crystals of trapped ions close to a structural phase transition, and subjected to state-dependent forces. We have shown that a coarse-grained elastodynamical theory, Eq. (74), yields a transparent long-wavelength description of phonon-mediated spin-spin interactions in harmonic trapped-ion crystals, Eq. (96), and that additional branch-cut contributions to the spin-spin couplings, Eq. (104), can be incorporated by considering the full lattice propagator, Eq. (100). By approaching the structural phase transition, the quartic nonlinearities start playing a role, and we use RG predictions to estimate how the bare couplings flow, Eq. (124), and how this flow will affect the range of the interactions in a regime where the rigidity of the ion crystal is very large, and the quantum fluctuations are largely suppressed. Finally, we have discussed a parametric driving scheme that can lead to a reduction of the shear modulus of the crystal, Eq. (126), which should amplify the effect of the nonlinearities in the effective Ising model.

Although the formalism hereby presented is specific to the zero-temperature $\lambda\phi^4$ QFT, the underlying ideas can be readily generalized to finite temperatures, to other QFTs of interest, and other couplings between the Ising sensors and the corresponding field operators. This could include composite operators in the Ising-Schwinger sources, Eq. (17), opening a route to probe fermionic QFTs, or to connect to generating functionals of other types of correlations functions in bosonic QFTs. Likewise, although we have focused on Lorentz-invariant QFTs, the underlying idea can also be applied to long-wavelength descriptions of quantum many-body systems where Lorentz invariance is not recovered at criticality.

Regarding the application to trapped-ion crystals, we have focused on $D = 1 + 1$ dimensions and the linear-to-zigzag structural phase transition. It would be interesting to find the coarse-grained description of other situations, such as two-dimensional triangular crystals of ions in Penning traps, or specific layouts of microfabricated Paul or Penning traps with other crystalline configurations. In addition, there are other types of structural phase transitions that can lead to other effective QFTs, and it would be interesting to understand the sensing scheme presented in our work for those situations. In addition to trapped-ion crystals, our results may also find applications in other quantum technologies, such as superconducting qubits coupled to Josephson-junction arrays, or other variants of transmission lines where nonlinear effects can play a role. In the atomic realm, one could also explore the application of our formalism to atomic impurities trapped coupled to ultracold quantum gases.

APPENDIX A: GENERATING FUNCTIONAL OF KLEIN-GORDON FIELDS

In this Appendix, we start with a basic description of the canonical quantization of a scalar QFT [104,105], which appears in many textbooks, e.g., Refs. [20,124]. We then introduce the concept of the generating functional [236], and make explicit derivations using canonical quantization instead of functional integral methods. This derivation will serve to set the notation, and discuss the sensing schemes

in the main text using a QFT language that is closer to quantum optics, preparing the ground for the functional-integral formalism used at later stages. As discussed in the main text, this derivation is useful to clarify key aspects of the interferometric scheme to measure such a generating functional by incorporating Ising spins [53], or the simpler sensing scheme that relies on the appearance of effective Ising models in specific dynamical situations.

The generating functional $Z_0[J]$ depends on the so-called Schwinger sources $J(x)$ [236], which, in the canonical formalism, are introduced as perturbations of the Klein-Gordon Hamiltonian density, Eq. (1), as follows: $\mathscr{H}_0 \to \mathscr{H}_0 + \mathscr{V}_J$, where

$$\mathscr{V}_J = -J(x)\phi(x), \tag{A1}$$

and $\phi(x)$ is the scalar-field operator described below Eq. (1). The sourced time-evolution operator $U(t_f, t_0) = U_{\mathscr{H}_0}U_{\mathscr{V}_J}$ can be expressed in terms of two unitaries

$$U_{\mathscr{H}_0} = e^{-i\int d^D\mathscr{H}_0}, \quad U_{\mathscr{V}_J} = \mathsf{T}\left\{e^{+i\int d^D J(x)\phi_H(x)}\right\}. \tag{A2}$$

Here, $\mathsf{T}\{\cdot\}$ is the time-ordering operator, and we introduce the fields $\phi_H(x) = (U_{\mathscr{H}_0})^\dagger \phi(x) U_{\mathscr{H}_0}$ evolving in the Heisenberg picture with respect to the unsourced Klein-Gordon Hamiltonian (1). In this picture, the vacuum persistence amplitude $\langle 0| U_{\mathscr{V}_J} |0\rangle$ can be used to define the normalized generating functional, as it clearly encodes all the information about n-point Feynman propagators of the field theory, $G_0^{(n)}(x_1, \ldots, x_n) = \langle 0| \mathsf{T}\{\phi_H(x_1)\cdots\phi_H(x_n)\} |0\rangle$. These can be recovered by taking functional derivatives

$$Z_0[J] = \langle 0| U_{\mathscr{V}_J} |0\rangle, \quad G_0^{(n)}(x_1, \ldots, x_n)$$
$$= \frac{(-i)^n \delta^n Z_0[J]}{\delta J(x_1)\cdots\delta J(x_n)}\bigg|_{J=0}. \tag{A3}$$

In order to derive the explicit expression of the normalized generating functional, and the corresponding Feynman propagators, we use the canonical mode expansion

$$\phi_H(x) = \int \frac{d^d\mathbf{k}}{(2\pi)^d 2\omega_\mathbf{k}} \left(a_\mathbf{k} e^{-ikx} + a_\mathbf{k}^\dagger e^{ikx}\right)\big|_{\mathrm{MS}},$$
$$\pi_H(x) = \int \frac{d^d\mathbf{k}}{(2\pi)^d 2}(-i)\left(a_\mathbf{k} e^{-ikx} - a_\mathbf{k}^\dagger e^{ikx}\right)\big|_{\mathrm{MS}}, \tag{A4}$$

where $kx = k_\mu x^\mu = \omega_\mathbf{k} t - \mathbf{k}\cdot\mathbf{x}$ is the Minkowski product for $\mu \in \{0, 1, \ldots, D-1\}$ on mass shell (MS) with

$$\omega_\mathbf{k} = \sqrt{\mathbf{k}^2 + m_0^2}. \tag{A5}$$

This is the dispersion relation of the Klein-Gordon massive bosons, which can be created or annihilated

by the covariant creation-annihilation operators $a_\mathbf{k}^\dagger, a_\mathbf{k}$, which satisfy Lorentz-invariant commutation relations $[a_\mathbf{k}, a_{\mathbf{k}'}^\dagger] = (2\pi)^d 2\omega_\mathbf{k}\delta^d(\mathbf{k} - \mathbf{k}')$. Up to the zero-point energy, the Hamiltonian terms in their corresponding pictures become

$$H_0 = \int \frac{d^d\mathbf{k}}{(2\pi)^d} \frac{\omega_\mathbf{k}}{2\omega_\mathbf{k}} a_\mathbf{k}^\dagger a_\mathbf{k},$$
$$V_J(t) = -\int \frac{d^d\mathbf{k}}{(2\pi)^d} \frac{J_\mathbf{k}(t)}{2\omega_\mathbf{k}} a_\mathbf{k}^\dagger e^{i\omega_\mathbf{k} t} + \mathrm{H.c.}, \tag{A6}$$

where we introduce the Fourier transform of the Schwinger sources $J_\mathbf{k}(t) = \int d^d\mathbf{x} \; J(t, \mathbf{x})e^{-i\mathbf{k}\cdot\mathbf{x}}$.

Let us note that the contribution of the sources to the evolution operator (A2) can be evaluated to the desired order of the coupling $J(x)$ by means of the Magnus expansion [114,115]. Moreover, for free Klein-Gordon fields, this expansion can be truncated at second order without any approximation

$$\log U_{\mathscr{V}_J} = -i \int_{t_0}^{t_f} dt_1 V_J(t_1)$$
$$- \frac{1}{2} \int_{t_0}^{t_f} dt_1 \int_{t_0}^{t_1} dt_2 \, [V_J(t_1), V_J(t_2)]. \tag{A7}$$

Using the Baker-Campbell-Haussdorf formula [237] to normal order the exponential of the first term, and considering the explicit time ordering of the second one, one finds that

$$U_{\mathscr{V}_J} =: e^{-i\int d^D x J(x)\phi_H(x)} :$$
$$e^{-(1/2)\int d^D x_1 \int d^D x_2 J(x_1)\Delta_{m_0}(x_1-x_2)J(x_2)}, \tag{A8}$$

where : : is the normal-ordering symbol, and we introduce the following space-time function:

$$\Delta_{m_0}(x) = \int \frac{d^d\mathbf{k}}{(2\pi)^d} \frac{1}{2\omega_\mathbf{k}} \left(e^{-ikx}\theta(t) + e^{+ikx}\theta(-t)\right)\big|_{\mathrm{MS}}. \tag{A9}$$

As customary in canonical quantization [20], the mass-shell condition in Eq. (A9) can be automatically imposed by introducing an extra contour integration over k^0, such that

$$\Delta_{m_0}(x) = \int_k \tilde{\Delta}_{m_0}(k)e^{-ikx}, \quad \tilde{\Delta}_{m_0}(k) = \frac{i}{k^2 - m_0^2 + i\epsilon}, \tag{A10}$$

where one directly identifies Feynman's two-point propagator of the Klein-Gordon field for $\epsilon \to 0^+$, and we use the short-hand notation $\int_k = \int d^D k/(2\pi)^D$. Since the normal-ordered term in Eq. (A8) will have a vanishing contribution

when acting on the Klein-Gordon vacuum, one can easily see that the vacuum persistence amplitude in Eq. (A3) yields

$$\mathsf{Z}_0[J] = e^{-(1/2)\int d^D x_1 \int d^D x_2 J(x_1)\Delta_{m_0}(x_1-x_2)J(x_2)}, \quad \text{(A11)}$$

which gives rise to any n-point propagator upon functional differentiation, Eq. (A3), in accordance to Wick's theorem, e.g.,

$$G_0^{(2)}(x_1, x_2) = -\left.\frac{\delta^2 \mathsf{Z}_0}{\delta J_{x_1} \delta J_{x_2}}\right|_{J=0} = \Delta_{m_0}(x_1-x_2) =: \Delta_{m_0,12},$$
$$\text{(A12)}$$

for the two-point function, and the four-point function

$$G_0^{(4)}(x_1,\dots,x_4) = \Delta_{m_0,12}\Delta_{m_0,34} + \Delta_{m_0,13}\Delta_{m_0,24}$$
$$+ \Delta_{m_0,14}\Delta_{m_0,23}. \quad \text{(A13)}$$

From now onwards we refer to the normalized $\mathsf{Z}_0[J]$, or its interacting version $\mathsf{Z}[J]$, as simply the generating functional.

APPENDIX B: GENERATING FUNCTIONAL OF INTERACTING $\lambda\phi^4$ FIELDS

In this Appendix, we describe the connection of the generating functional to the perturbative approach to QFTs based on Feynman diagrams, in which the $\lambda\phi^4$ model plays a key role [238]. Although this is discussed in several textbooks, e.g., Refs. [20,124,239], this Appendix makes our work self-contained, and presents the results in a way that are useful to connect to the effective Ising models, making this material more amenable to the quantum-technology community not familiarized with QFT functional methods.

The time-evolution operator in the presence of classical Schwinger sources, Eq. (A1), $U(t_f, t_0) = U_{\mathscr{H}} U_{\mathscr{V}_J}$, can again be expressed in terms of two unitaries

$$U_{\mathscr{H}} = e^{-i\int d^D x \mathscr{H}}, \quad U_{\mathscr{V}_J} = \mathsf{T}\left\{e^{+i\int d^D x J(x)\phi_H(x)}\right\}, \quad \text{(B1)}$$

where the field operators $\phi_H(x) = U_{\mathscr{H}}^\dagger \phi(x) U_{\mathscr{H}}$ now evolve in the Heisenberg picture with respect to the full interacting $\lambda\phi^4$ model, Eq. (40), in the absence of sources, thus accounting for possible scattering events. In this case, the "vacuum" persistence amplitude will lead to the full generating functional

$$\mathsf{Z}[J] = \langle 0| U_{\mathscr{V}_J} |0\rangle, \quad G^{(n)}(x_1,\dots,x_n)$$
$$= \left.\frac{(-i)^n \delta^n \mathsf{Z}[J]}{\delta J(x_1)\cdots\delta J(x_n)}\right|_{J=0}, \quad \text{(B2)}$$

where $|0\rangle$ is the ground state of the interacting QFT, and the functional derivatives yield the full n-point propagators.

Note that, depending on the bare parameters of the theory, this ground state can support a nonzero particle content via spontaneous symmetry breaking [132,133], although it is still customary to refer to it as the "vacuum." In this paper, we are only interested in regimes with unbroken symmetry.

We note that the exact expression, Eq. (A7), for the source contribution to the evolution operator, Eq. (B1), is no longer valid in the presence of interactions, and working with the canonical formalism gets cumbersome rapidly. Hence, one typically switches to functional integral methods. As customary, one uses the field and momentum representation at fixed time $t = x^0$, $\phi(x)|\{\varphi(x^0, \mathbf{x})\}\rangle = \varphi(x^0, \mathbf{x})|\{\varphi(x^0, \mathbf{x})\}\rangle$, $\pi(x)|\{\Pi(x^0, \mathbf{x})\}\rangle = \Pi(x^0, \mathbf{x})|\{\Pi(x^0, \mathbf{x})\}\rangle$, where the eigenvalues are now classical fields, and the eigenvectors form a complete orthonormal basis [20,239]. By splitting the time evolution in infinitesimal lapses, one can introduce the resolution of the identity at nearby fixed instants of time, alternating the use of the field and momentum basis. Performing a Gaussian integral over the momentum fields $\Pi(x^0, \mathbf{x})$, the generating functional (B2) can be expressed as the functional integral

$$\mathsf{Z}[J] = \frac{1}{\mathsf{N}}\int D\varphi\, e^{iS}, \quad S = \int d^D x\left[\mathscr{L}_0 - \mathscr{V}_{\text{int}}(\varphi) - \mathscr{V}_J(\varphi)\right],$$
$$\text{(B3)}$$

where $D\varphi$ is the functional-integral measure. Here, the action is expressed in terms of the Klein-Gordon Lagrangian

$$\mathscr{L}_0 = \frac{1}{2}\partial_\mu\varphi(x)\partial^\mu\varphi(x) - \frac{1}{2}m_0^2\varphi^2(x), \quad \text{(B4)}$$

where $\partial_\mu = (\partial_t, \nabla)$, $\partial^\mu = (\partial_t, -\nabla)$, and the source and interaction parts correspond to Eqs. (A1) and (40), respectively, expressed in terms of the basis fields $\phi(x) \to \varphi(x)$. In addition, we introduce a normalization factor in terms of the unsourced action $\mathsf{N} = \int D\varphi\, e^{iS}\big|_{J=0}$ such that $\mathsf{Z}[0] = 1$.

A central result in the perturbative approach to QFTs is that the full generating functional can be expressed in terms of the noninteracting one, Eq. (11), as follows:

$$\mathsf{Z}[J] = \frac{e^{-i\int d^D x \mathscr{V}_{\text{int}}(-i\delta_{J(x)})}\mathsf{Z}_0[J]}{e^{-i\int d^D x \mathscr{V}_{\text{int}}(-i\delta_{J(x)})}\mathsf{Z}_0[J]\bigg|_{J=0}}, \quad \text{(B5)}$$

where we introduce a short-hand notation for the functional derivatives $\delta_{J(x)} = \delta/\delta J(x)$. In perturbative treatments, one typically expands the exponential of the interacting potential to the desired order of the interaction strength λ_0, allowing for a graphical representation in terms of Feynman diagrams. In our case, keeping second-order terms with at most four sources, we get the following diagrammatic representation:

$$Z[J] = \left(1 + \frac{i}{4} \times\!\!\bullet\!\!\times + \frac{1}{8} \times\!\!\bullet\!\!\times + \frac{1}{8} \times\!\!\bullet\bullet\!\!\times + \frac{1}{12} \times\!\!\bigcirc\!\!\times - \frac{i}{4!} \times\!\!+\!\!\times - \frac{1}{12} \times\!\!\bullet\!\!\times - \frac{1}{32} \times\!\!\bullet\bullet\!\!\times - \frac{1}{16} \times\!\!\bigcirc\!\!\times + \cdots \right) Z_0[J],$$

$$\text{(B6)}$$

which should be read as follows: crosses $\times = J(x)$ represent the Schwinger sources acting at different space-time locations x, and blobs $\bullet = \lambda_0$ stand for interaction vertices with the bare quartic coupling. Solid lines that join a cross and a blob should be translated into $\times\!\!-\!\!\bullet = \Delta_{m_0}(x - z)$, and thus involve the free d-dimensional Feynman propagator (10) from the source at x to the vertex at z. Likewise, solid lines connected to the same blob stand for interaction loops that should be translated for $\bigcirc = \Delta_{m_0}(0)$, while those connecting two distant blobs must be substituted by the propagator between the corresponding points $\bullet\!\!-\!\!\bullet = \Delta_{m_0}(z_1 - z_2)$. For each of the above diagrams, we should integrate over all possible space-time locations of the sources $\int d^D x_i$, and those of the intermediate interaction vertices $\int d^D z_i$.

This perturbative expression (B6) suffices to understand the main effects of the scalar-field self-interactions. The standard approach calculates how the two- and four-point functions $G^{(2)}(x_1, x_2)$, $G^{(4)}(x_1, \ldots, x_4)$, obtained by substituting Eq. (B6) in Eq. (B2), change with respect to the free ones, Eqs. (A12) and (A13), due to the self-interactions. This leads to a neat discussion of the appearance of divergences, the need to regularize the QFT, and renormalization [20,124,239]. We focus instead on rewriting this perturbative series as a renormalized generating functional, as this sets the stage for our calculation of the changes in the effective Ising model, Eq. (38), when upgrading to Ising-Schwinger sources, as described in the main text. For the moment, we focus on the first four diagrams of Eq. (B6), which involve a pair of sources. The first three diagrams are combinations of the so-called tadpole, and one can see that a renormalized functional

$$Z_r[J] = e^{-(1/2) \int d^D x_1 \int d^D x_2 J(x_1) \Delta_{m_r}(x_1 - x_2) J(x_2)}, \quad \text{(B7)}$$

generates directly these terms to second order in λ_0 if the propagator has the following additive mass renormalization:

$$m_0^2 \rightarrow m_r^2 = m_0^2 + \Sigma(0). \quad \text{(B8)}$$

Here, we introduce the so-called self-energy $\Sigma(k)$, which relates the full and free propagators via the Dyson-Schwinger equation [107,108,240], namely

$$i\tilde{G}^{-1}(k) = i\tilde{\Delta}_{m_0}^{-1}(k) + \Sigma(k), \quad \tilde{G}(k) = \frac{i}{k^2 - m_0^2 - \Sigma(k)}, \quad \text{(B9)}$$

such that the renormalization of the mass by the zero-momentum self-energy, Eq. (55), becomes apparent.

To show that the different powers of the Taylor series of the renormalized generating functional (B7) are equivalent to the first three diagrams, one must apply $\int d^D k \, e^{-ik(x-y)}/(k^2 - m_0^2 + i\epsilon)^2 = -(2\pi)^D \int d^D z \, \Delta_{m_0}(x - z) \Delta_{m_0}(z - y)$ repeatedly, and consider a mass renormalization $\Sigma(0) = \Sigma_{m_0,\lambda_0}^{(1,\text{td})} + \Sigma_{m_0,\lambda_0}^{(2,\text{td})}$ with

$$\Sigma_{m_0,\lambda_0}^{(1,\text{td})} = \frac{\lambda_0}{2} \int_{k_1} \tilde{\Delta}_{m_0}(k_1), \quad \text{(B10)}$$

for the single-tadpole diagram [i.e., first diagram in Eq. (B6)], and

$$\Sigma_{m_0,\lambda_0}^{(2,\text{td})} = -i \frac{\lambda_0^2}{4} \int_{k_1} \int_{k_2} \tilde{\Delta}_{m_0}^2(k_1) \tilde{\Delta}_{m_0}(k_2), \quad \text{(B11)}$$

for the double-tadpole diagram [i.e., second diagram in Eq. (B6)]. Interestingly, the third diagram is directly generated by the Taylor expansion of the exponential, and does not contribute with an additional renormalization of the mass. In the language of QFTs, the self-energy only has contributions from one-particle irreducible (1PI) diagrams, namely those that cannot be split into two disconnected diagrams by cutting a single internal line and propagator. Since the third diagram in Eq. (B6) can indeed be split in a couple of disconnected tadpoles, it does not contribute to the self-energy as just shown.

Finding the contribution of the fourth diagram in Eq. (B6), the so-called sunrise diagram, to a renormalized generating functional like Eq. (B7) is slightly more involved. While the tadpole diagrams involve virtually excited bosons with a momentum that is independent to that of the propagating bosons; this is not the case for the virtual bosons in the sunrise diagram. As a consequence, its contribution to the self-energy depends on the external momentum, and cannot be simply recast as a mass renormalization, Eq. (55). In fact, one finds

$$\Sigma^{(2,\text{sr})}(k) = -i \frac{\lambda_0^2}{6} \int_{k_1} \int_{k_2} \tilde{\Delta}_{m_0}(k_1) \tilde{\Delta}_{m_0}(k_2) \tilde{\Delta}_{m_0}(k - k_1 - k_2), \quad \text{(B12)}$$

which can be expanded in a power series of the external momentum as follows:

$$\Sigma^{(2,\text{sr})}(k) = \Sigma^{(2,\text{sr})}_{m_0,\lambda_0} + k^2 \left.\frac{\partial \Sigma^{(2,\text{sr})}(k)}{\partial k^2}\right|_{k^2=0} + \cdots. \quad (B13)$$

To zeroth order in the external momentum, one finds that the sunrise diagram indeed contributes to the renormalized mass via $\Sigma(0) = \Sigma^{(1,\text{td})}_{m_0,\lambda_0} + \Sigma^{(2,\text{td})}_{m_0,\lambda_0} + \Sigma^{(2,\text{sr})}_{m_0,\lambda_0}$, where

$$\Sigma^{(2,\text{sr})}_{m_0,\lambda_0} = -i\frac{\lambda_0^2}{6} \int_{k_1} \int_{k_2} \tilde{\Delta}_{m_0}(k_1) \tilde{\Delta}_{m_0}(k_2) \tilde{\Delta}_{m_0}(k_1+k_2). \quad (B14)$$

To next order in the external momentum, one sees through the Dyson-Schwinger Eq. (B9) that the sunrise diagram changes the propagator in momentum space, Eq. (10), into

$$\tilde{\Delta}_{m_0}(k) \to \tilde{G}(k) = \frac{i}{z^{-1}_{m_0,\lambda_0} k^2 - m_r^2 + i\epsilon}. \quad (B15)$$

Here, we introduce the following parameter: $z^{-1}_{m_0,\lambda_0} = 1 - \partial_{k^2}\Sigma(k)|_{k^2=0}$, which, for the sunrise diagram, reads

$$z^{-1}_{m_0,\lambda_0} = 1 - \frac{\lambda_0^2}{6} \int_{k_1} \int_{k_2} \tilde{\Delta}_{m_0}(k_1) \tilde{\Delta}_{m_0}(k_2) \tilde{\Delta}^2_{m_0}(k_1+k_2). \quad (B16)$$

This effect can be alternatively understood as a renormalization of the derivative terms $\partial_\mu\varphi\partial^\mu\varphi \to z^{-1}_{m_0,\lambda_0}\partial_\mu\varphi\partial^\mu\varphi$ in the action, Eq. (B4). This leads to the so-called wavefunction renormalization [20,124], where the fields must be rescaled $\varphi(x) \to \varphi(x)/\sqrt{z_{m_0,\lambda_0}}$ in order to recover the original form of the Klein-Gordon Lagrangian. As a consequence of this rescaling, one gets a multiplicative renormalization of both the bare mass $m_0^2 \to m_r^2$, and the Schwinger sources $J(x) \to J_r(x)$

$$m_r^2 = \left(m_0^2 + \Sigma^{(1,\text{td})}_{m_0,\lambda_0} + \Sigma^{(2,\text{sr})}_{m_0,\lambda_0}\right) z_{m_0,\lambda_0},$$
$$J_r(x) = J(x)\sqrt{z_{m_0,\lambda_0}}. \quad (B17)$$

It turns out that contributions to Eq. (B13) of a higher-order in the external momentum are irrelevant in the renormalization-group sense [106,113,149], and can thus be neglected at long wavelengths. Taking into account all these different renormalizations, the full generating functional of the interacting QFT to second order is

$$\mathsf{Z}_r[J_r] = e^{-(1/2)\int d^D x_1 \int d^D x_2 J_r(x_1)\Delta_{m_r}(x_1-x_2)J_r(x_2)}. \quad (B18)$$

Once all of the two-source diagrams in Eq. (B6) have been carefully accounted for in the renormalized generating functional (B18), we focus on the remaining four-source

processes. We start with the tree-level vertex corresponding to the fifth Feynman diagram, which can be recast as

$$e^{-(i/4!)\int d^D x_1 \int d^D x_2 \int d^D x_3 \int d^D x_4 J(x_1)J(x_2)G^{(4,c)}_{m_0,\lambda_0}(x_1,x_2,x_3,x_4)J(x_3)J(x_4)}. \quad (B19)$$

Here, we introduce the connected four-point propagator, which is consistent with the fact that only 1PI diagrams should be incorporated in the renormalized generating functional, as the reducible ones will be automatically generated by the power expansion of the exponential. This connected four-point function is obtained from Eq. (B2) via $G^{(4,c)}_{m_0,\lambda_0}(x_1,x_2,x_3,x_4) = G^{(4)}_{m_0,\lambda_0}(x_1\cdots x_4) - \Delta_{m_0,12}\Delta_{m_0,34} - \Delta_{m_0,13}\Delta_{m_0,24} - \Delta_{m_0,14}\Delta_{m_0,23}$. To this lowest order in the interaction strength, we find

$$G^{(4,c)}_{m_0,\lambda_0} = \lambda_0 \int d^D z \Delta_{m_0}(x_1-z)\Delta_{m_0}(x_2-z)$$
$$\times \Delta_{m_0}(z-x_3)\Delta_{m_0}(z-x_4). \quad (B20)$$

The sixth diagram in Eq. (B6) can be seen as a tadpole decoration of the previous one, which, together with higher-order terms involving more tadpoles, can be accounted for by considering the connected propagator with a renormalized mass. Note that the seventh diagram, and higher-order disconnected diagrams of the like, are already accounted for by the expansion of the functional (B18) to the corresponding order. Had we considered $\mathcal{O}(\lambda_0^3)$ corrections, we would have also obtained a disconnected four-source diagram decorated with a sunrise graph, which is again directly accounted for if we use the renormalized functional in Eq. (B18). Therefore, all of these decorations are accounted for by substituting $G^{(4,c)}_{m_0,\lambda_0} \to G^{(4,c)}_{\tilde{m}_r,\lambda_0}$ in Eq. (B19) with the additive and multiplicative renormalizations of the mass and sources.

Once again, we have left the discussion about a diagram leading to new effects, the eighth diagram of Eq. (B6), for the last part of this Appendix. This term describes how the four-point interaction can be mediated by a pair of virtual bosons exchanged between a pair of propagating particles. Therefore, it will lead to a renormalization of the coupling strength $\lambda_0 \to \lambda_r$

$$\lambda_r = \lambda_0 + \Gamma^{(4)}_{m_0,\lambda_0}, \quad \Gamma^{(4)}_{m_0,\lambda_0} = -i\frac{3\lambda_0^2}{2} \int_{k_1} \tilde{\Delta}^2_{m_0}(k_1), \quad (B21)$$

which should also be complemented with the wavefunction renormalization

$$\tilde{\lambda}_r = \left(\lambda_0 + \Gamma^{(4)}_{m_0,\lambda_0}\right) z^2_{m_0,\lambda_0}. \quad (B22)$$

The combination of all these renormalizations must be included in the following renormalized generating functional:

$$\mathsf{Z}_r[J_r] = e^{-(1/2)\int d^D x_1 \int d^D x_2 J_r(x_1)\Delta_{m_r}(x_1-x_2)J_r(x_2)-(i/4!)\int d^D x_1 \int d^D x_2 \int d^D x_3 \int d^D x_4 J_r(x_1)J_r(x_2)G^{(4,c)}_{m_r,\lambda_r}(x_1,x_2,x_3,x_4)J_r(x_3)J_r(x_4)}. \quad \text{(B23)}$$

We close this Appendix by noting that higher-order terms in the expansion will lead to $2n$-source contributions with $n = 3, 4, \ldots$ coupled to the corresponding renormalized connected $2n$-point propagator. In the limit of impulsive sources, one would obtain the $2n$-point propagator, including also the disconnected pieces, by evaluating the corresponding functional derivatives (B2) on the renormalized functional (B23).

APPENDIX C: ELASTIC CRYSTALS: COMPRESSIBILITY, MASSLESS KLEIN-GORDON FIELDS, AND EFFECTIVE ISING MODELS

Following the multidisciplinary approach of this work, we include in this Appendix a basic description of the long-wavelength theory of vibrations of crystalline solids, a topic that appears in several textbooks [173,174]. This serves to give a self-contained presentation, but also to present key concepts in connection to our previous QFT approach, trying to make the discussions of the main text more amenable to potential readers from the high-energy-physics community.

We start by reviewing Debye's model for the specific heat of solids [241], which can be understood as the quantization of a coarse-grained elastodynamical model [195,196] that captures the dynamics of the crystal at long wavelengths. A crystalline solid subjected to external forces can be modeled by a displacement field $\mathbf{u}(t, \mathbf{x})$ at a given instant of time t for each point of the crystal $\mathbf{x}$. This accounts for a deformation of the solid when its components support a nonzero gradient $\nabla u_\alpha(t, \mathbf{x})$, i.e., expansion and compression or shear strain. In the theory of elasticity, the response to such a strain comes in the form of stress forces acting against the deformation, which have their microscopic origin in the interatomic short-range interactions that try to restore equilibrium in the solid. For such a coarse-grained description, these forces are local, and can be described in terms of pressure and shear stress.

To simplify the description, we consider the academic problem of a $d = 1$-dimensional crystal. In this case, strain can only appear in the form of compression and expansion, and stress in the form of pressure. For elastic materials, Hook's law states that strain and stress are proportional. In particular, for this simple 1D situation, the compression and expansion is modeled by the relative change of the length of the crystal $\delta L/L$, which, according to Hook's law, must be proportional to the pressure P. This leads to $\delta L/L = -P/K_e$, where K_e is the elastic or bulk modulus.

This parameter can be related to the inverse of the thermal compressibility $\beta_T = -(1/L)(\partial L/\partial P)\big|_T = K_e^{-1}$, and thus quantifies the stiffness of the crystal to external forces, i.e., how it resists bulk changes in its length.

For homogeneous elastic solids, the dynamics of the coarse-grained field is described by a wave equation, the so-called Cauchy-Navier equation. In this simple 1D case, setting the crystal along the x axis, this equation describes vibrations of pressure in the form of a compressional wave evolving under

$$\left(\partial_t^2 - c_\ell^2 \partial_{\mathsf{x}}^2\right) u_{\mathsf{x}}(t, \mathsf{x}) = 0, \quad c_\ell = \sqrt{\frac{K_e}{\rho}}. \quad \text{(C1)}$$

Here, the sound speed c_ℓ is defined in terms of the elastic modulus and the mass density of the crystal ρ, which must be homogeneous at this coarse-grained scale.

At this point, one can rescale the displacement field to obtain a $D = (1 + 1)$-dimensional scalar field with the correct scaling natural dimension discussed below Eq. (29) in natural units $c_\ell = 1 = \hbar$. Denoting by a some characteristic microscopic length scale of the crystal, one finds that the compressional wave, Eq. (C1), is indeed governed by the massless Klein-Gordon Lagrangian (B4) with the following identifications:

$$\phi(x) \rightarrow \frac{1}{a} u_{\mathsf{x}}(t, \mathsf{x}), \quad c \rightarrow c_\ell, \quad m_0^2 \rightarrow 0. \quad \text{(C2)}$$

Hence, if one considers that the speed of sound plays the role of the light speed, there is an effective Lorentz invariance emerging at long wavelengths in this coarse-grained one-dimensional crystal. Although this symmetry is not strictly exact due to the neglected microscopic short-wavelength details, or possible deviations from Hook's law, one expects it to dominate the low-energy behavior of the crystal, a deep and fundamental result that can be formalized through the use of the renormalization group [106,149]. In fact, this emergence of symmetries at the coarse-grained level underlies contemporary nonperturbative approaches to strongly coupled QFTs, such as lattice quantum chromodynamics [46,242].

In Debye's approach, one proceeds by quantizing this field by the introduction of operators, Eq. (A4), that create-annihilate quantized collective vibrations (C1), the so-called phonons

$$H_p = \int \frac{d\mathsf{k}}{2\pi} \omega_{\mathsf{k}} a_{\mathsf{k}}^\dagger a_{\mathsf{k}}, \quad \omega_{\mathsf{k}} = |\mathsf{k}|, \quad \text{(C3)}$$

and then calculates the partition function to extract any thermodynamic quantity, such as the specific heat [173]. Note that our 1D crystal would be unstable with respect to thermal fluctuations [167–169], and this is why we categorize it as an academic problem. In more realistic situations, the crystal would likely consist of weakly coupled chains, and one would need to consider also deformations with shear strain, which, according to Hook's law, are proportional to the shear stress via a new coefficient: the rigidity or shear modulus μ_r [195,196]. These additional deformations change the longitudinal speed of sound and, moreover, lead to additional transverse sound waves. For instance, for the z axis transverse to the weakly coupled chains, the wave equation is

$$\left(\partial_t^2 - c_{\text{t}}^2\partial_{\text{x}}^2\right)u_{\text{z}}(t,\text{x}) = 0, \quad c_{\text{t}} = \sqrt{\frac{\mu_r}{\rho}}. \quad \text{(C4)}$$

This forbids the recovery of Lorentz invariance even at long wavelengths, as massless fundamental particles should propagate within a unique light cone, but the longitudinal and transverse waves propagate with different speeds of sound. In fact, both longitudinal and transverse waves play a key role in the usefulness of Debye's model to reproduce correctly the specific heat of a thermal solid. As discussed in the main text, sound waves in laser-cooled crystals of trapped ions can be selectively excited, such that either the longitudinal or the transverse branch contributes to the dynamics, and there is again a Lorentz invariance emerging at long wavelengths.

It is interesting to note that, despite the absence of interactions and UV loop divergences, Debye's theory is a long-wavelength description that requires a frequency cutoff to recover the correct temperature dependence of the specific heat [173]. This is the so-called Debye frequency ω_D, which allows one to reduce the number of degrees of freedom from the infinity of the coarse-grained field theory, Eq. (C1), into the large, yet finite, number that characterizes the elastic crystal. In $d = 1$, this hard cutoff would correspond to

$$\omega_{\text{k}} \leq \omega_D = \pi\frac{c_\ell N}{L}, \quad |\text{k}| \leq \Lambda_c = \pi\frac{N}{L}, \quad \text{(C5)}$$

where N is the number of atoms in the solid. This equation becomes a generic UV cutoff, Eq. (65), using natural units $c_\ell = 1$.

To carry this discussion further, let us now address the difficulties in including the Ising-Schwinger couplings, Eq. (17), in a solid-state crystal. One may consider a collection of n impurities at positions $\mathbf{x}_i = \text{x}_i\mathbf{e}_{\text{x}}$, each of which can host electrons in a single orbital of energy ω_0. These impurities are sufficiently far apart that the electrons cannot tunnel between them, and thus remain localized. In the regime where all the electrons are spin polarized, e.g.,

using an external magnetic field, they can be described by spinless fermion operators c_i, $c_i^\dagger$ with the following simple Hamiltonian:

$$H_e = \sum_i \omega_0 c_i^\dagger c_i = \int d\text{x}\delta\epsilon(\text{x})Q(t,\text{x}), \quad \text{(C6)}$$

where we use the energy densities in Eq. (31), and the Jordan-Wigner transformation $Z(t,\text{x}_i) = 2c_i^\dagger c_i - 1$ [127], such that the Ising projector is $Q(t,\text{x}) = [1 + Z(t,\text{x})]/2$. In the context of electron-phonon coupling, a so-called Holstein coupling [243] of strength g, would then lead to

$$H_{e\text{-}p} = \sum_i gc_i^\dagger c_i u_\text{x}(t,\text{x}_i) = \int d\text{x}J(t,\text{x})Z(t,\text{x})\phi(t,\text{x}),$$
$$\text{(C7)}$$

where $J(t,x)$ is defined according to Eq. (35) with $J_0 = -2g$. In order to get the harmonic time dependence of the sources, one would need to introduce externally controlled periodic modulations of the electron-phonon coupling, which does not sound very realistic. In the main text, we explore more realistic alternatives based on trapped ions.

Let us close this Appendix by noting how Debye's cutoff enters in the discussion. In our high-energy physics model, we emphasized the importance of using a harmonic source with a frequency below the bare mass of the scalar field, avoiding in this way possible resonances and dissipative processes [see the discussion below Eq. (24)]. Clearly, in the absence of a UV cutoff, the dispersion relation (A5) extends to arbitrarily large energies, and the only possibility was to set $\omega_J^2 \lesssim m_0^2$. However, in the presence of a physical cutoff, one can also set $\omega_J^2 \gtrsim \Lambda_c$ to avoid such resonances. For the massless scalar field associated to the longitudinal phonons, Eq. (C2), we would get effective Ising interactions with the exponentially decaying couplings in Eq. (32), controlled by $m_{\text{eff}}^2 = \omega_J^2$. In this case, the spin-spin couplings read

$$\mathsf{J}_{ij} \propto e^{-\omega_J|t_{\text{x}_i-\text{x}_j}|}\cos\left[\mathsf{k}_J(\text{x}_i - \text{x}_j)\right], \quad \text{(C8)}$$

where $t_{\text{x}_i-\text{x}_j} = |\text{x}_i - \text{x}_j|/c_\ell$ is the time the sound wave takes to propagate between the two corresponding spins.

Let us note that, in addition to the limitations already discussed, including the transverse field, Eq. (38), which makes the Ising model an archetype for the study of quantum phase transitions [244], would also be unrealistic, as the Jordan-Wigner transformation would require highly nonlocal electronic terms. Last, but not least, the simplified sensing protocol discussed in Sec. II B would require local measurements of the electronic populations to be performed and, more critically, the effective spins to be initialized in a coherent superposition of the impurity being vacant or occupied by a single electron, which is also not

very realistic. One could avoid this complication by considering spinful fermions instead, but then the the problem would translate into finding materials where the Holstein coupling, Eq. (C7), is spin dependent. In the main text, we show that all these drawbacks can be overcome by moving from solid-state physics to trapped-ion quantum technologies.

---

[1] M. A. Nielsen and I. L. Chuang,*Quantum Computation and Quantum Information: 10th Anniversary Edition* (Cambridge University Press, Cambridge, 2010).

[2] B. M. Terhal, Quantum error correction for quantum memories, Rev. Mod. Phys. **87**, 307 (2015).

[3] D. G. Cory, M. D. Price, W. Maas, E. Knill, R. Laflamme, W. H. Zurek, T. F. Havel, and S. S. Somaroo, Experimental Quantum Error Correction, Phys. Rev. Lett. **81**, 2152 (1998).

[4] J. Chiaverini, D. Leibfried, T. Schaetz, M. D. Barrett, R. B. Blakestad, J. Britton, W. M. Itano, J. D. Jost, E. Knill, C. Langer, R. Ozeri, and D. J. Wineland, Realization of quantum error correction, Nature **432**, 602 (2004).

[5] M. D. Reed, L. DiCarlo, S. E. Nigg, L. Sun, L. Frunzio, S. M. Girvin, and R. J. Schoelkopf, Realization of three-qubit quantum error correction with superconducting circuits, Nature **482**, 382 (2012).

[6] P. Schindler, J. T. Barreiro, T. Monz, V. Nebendahl, D. Nigg, M. Chwalla, M. Hennrich, and R. Blatt, Experimental repetitive quantum error correction, Science **332**, 1059 (2011).

[7] D. Nigg, M. Müller, E. A. Martinez, P. Schindler, M. Hennrich, T. Monz, M. A. Martin-Delgado, and R. Blatt, Quantum computations on a topologically encoded qubit, Science **345**, 302 (2014).

[8] J. Kelly, *et al.*, State preservation by repetitive error detection in a superconducting quantum circuit, Nature **519**, 66 (2015).

[9] N. M. Linke, M. Gutierrez, K. A. Landsman, C. Figgatt, S. Debnath, K. R. Brown, and C. Monroe, Fault-tolerant quantum error detection, Sci. Adv. **3**, e1701074 (2017).

[10] R. Stricker, D. Vodola, A. Erhard, L. Postler, M. Meth, M. Ringbauer, P. Schindler, T. Monz, M. Müller, and R. Blatt, Experimental deterministic correction of qubit loss, Nature **585**, 207 (2020).

[11] L. Egan, D. M. Debroy, C. Noel, A. Risinger, D. Zhu, D. Biswas, M. Newman, M. Li, K. R. Brown, M. Cetina, and C. Monroe, Fault-tolerant operation of a quantum error-correction code, ArXiv:2009.11482 (2021).

[12] A. Erhard, H. Poulsen Nautrup, M. Meth, L. Postler, R. Stricker, M. Stadler, V. Negnevitsky, M. Ringbauer, P. Schindler, H. J. Briegel, R. Blatt, N. Friis, and T. Monz, Entangling logical qubits with lattice surgery, Nature **589**, 220 (2021).

[13] D. Wineland, C. Monroe, W. Itano, B. King, D. Leibfried, D. Meekhof, C. Myatt, and C. Wood, Experimental primer on the trapped ion quantum computer, Fortsch. Phys. **46**, 363 (1998).

[14] P. Schindler, D. Nigg, T. Monz, J. T. Barreiro, E. Martinez, S. X. Wang, S. Quint, M. F. Brandl, V. Nebendahl,

[15] C. F. Roos, M. Chwalla, M. Hennrich, and R. Blatt, A quantum information processor with trapped ions, New J. Phys. **15**, 123012 (2013).

[15] C. D. Bruzewicz, J. Chiaverini, R. McConnell, and J. M. Sage, Trapped-ion quantum computing: Progress and challenges, Appl. Phys. Rev. **6**, 021314 (2019).

[16] J. Preskill, Quantum computing in the NISQ era and beyond, Quantum **2**, 79 (2018).

[17] F. Arute, *et al.*, Quantum supremacy using a programmable superconducting processor, Nature **574**, 505 (2019).

[18] H.-S. Zhong, *et al.*, Quantum computational advantage using photons, Science **370**, 1460 (2020).

[19] A. W. Harrow and A. Montanaro, Quantum computational supremacy, Nature **549**, 203 (2017).

[20] M. E. Peskin and D. V. Schroeder, *An Introduction to Quantum Field Theory* (Addison-Wesley, Reading, USA, 1995).

[21] E. Fradkin, *Field Theories of Condensed Matter Physics* (Cambridge University Press, Cambridge, 2013), 2nd ed.

[22] S. P. Jordan, K. S. M. Lee, and J. Preskill, Quantum algorithms for quantum field theories, Science **336**, 1130 (2012).

[23] S. Hands, The phase diagram of QCD, Contemp. Phys. **42**, 209 (2001).

[24] R. P. Feynman, Simulating physics with computers, Int. J. Theor. Phys. **21**, 467 (1982).

[25] J. I. Cirac and P. Zoller, Goals and opportunities in quantum simulation, Nat. Phys. **8**, 264 (2012).

[26] S. Lloyd, Universal quantum simulators, Science **273**, 1073 (1996).

[27] D. Jaksch, C. Bruder, J. I. Cirac, C. W. Gardiner, and P. Zoller, Cold Bosonic Atoms in Optical Lattices, Phys. Rev. Lett. **81**, 3108 (1998).

[28] M. Greiner, O. Mandel, T. Esslinger, T. W. Hänsch, and I. Bloch, Quantum phase transition from a superfluid to a mott insulator in a gas of ultracold atoms, Nature **415**, 39 (2002).

[29] W. Hofstetter, J. I. Cirac, P. Zoller, E. Demler, and M. D. Lukin, High-Temperature Superfluidity of Fermionic Atoms in Optical Lattices, Phys. Rev. Lett. **89**, 220407 (2002).

[30] R. Jördens, N. Strohmaier, K. Günter, H. Moritz, and T. Esslinger, A mott insulator of fermionic atoms in an optical lattice, Nature **455**, 204 (2008).

[31] U. Schneider, L. Hackermüller, S. Will, T. Best, I. Bloch, T. A. Costi, R. W. Helmes, D. Rasch, and A. Rosch, Metallic and insulating phases of repulsively interacting fermions in a 3D optical lattice, Science **322**, 1520 (2008).

[32] I. Bloch, J. Dalibard, and S. Nascimbène, Quantum simulations with ultracold quantum gases, Nat. Phys. **8**, 267 (2012).

[33] D. Jaksch and P. Zoller, The cold atom Hubbard toolbox, Ann. Phys. **315**, 52 (2005).Special issue.

[34] D. Porras and J. I. Cirac, Effective Quantum Spin Systems with Trapped Ions, Phys. Rev. Lett. **92**, 207901 (2004).

[35] A. Friedenauer, H. Schmitz, J. T. Glueckert, D. Porras, and T. Schaetz, Simulating a quantum magnet with trapped ions, Nat. Phys. **4**, 757 (2008).

[36] R. Islam, E. E. Edwards, K. Kim, S. Korenblit, C. Noh, H. Carmichael, G.-D. Lin, L.-M. Duan, C.-C. Joseph Wang,

J. K. Freericks, and C. Monroe, Onset of a quantum phase transition with a trapped ion quantum simulator, Nat. Commun. **2**, 377 (2011).

[37] B. P. Lanyon, C. Hempel, D. Nigg, M. Müller, R. Gerritsma, F. Zähringer, P. Schindler, J. T. Barreiro, M. Rambach, G. Kirchmair, M. Hennrich, P. Zoller, R. Blatt, and C. F. Roos, Universal digital quantum simulation with trapped ions, Science **334**, 57 (2011).

[38] R. Blatt and C. F. Roos, Quantum simulations with trapped ions, Nat. Phys. **8**, 277 (2012).

[39] C. Monroe, W. C. Campbell, L. M. Duan, Z. X. Gong, A. V. Gorshkov, P. Hess, R. Islam, K. Kim, N. Linke, G. Pagano, P. Richerme, C. Senko, and N. Y. Yao, Programmable quantum simulations of spin systems with trapped ions, ArXiv:1912.07845 (2020).

[40] M. C. Bañuls, *et al.*, Simulating lattice gauge theories within quantum technologies, Eur. Phys. J. D **74**, 165 (2020).

[41] L. Lamata, J. León, T. Schätz, and E. Solano, Dirac Equation and Quantum Relativistic Effects in a Single Trapped Ion, Phys. Rev. Lett. **98**, 253005 (2007).

[42] R. Gerritsma, G. Kirchmair, F. Zähringer, E. Solano, R. Blatt, and C. F. Roos, Quantum simulation of the Dirac equation, Nature **463**, 68 (2010).

[43] R. Gerritsma, B. P. Lanyon, G. Kirchmair, F. Zähringer, C. Hempel, J. Casanova, J. J. García-Ripoll, E. Solano, R. Blatt, and C. F. Roos, Quantum Simulation of the Klein Paradox with Trapped Ions, Phys. Rev. Lett. **106**, 060503 (2011).

[44] S.-L. Zhu, B. Wang, and L.-M. Duan, Simulation and Detection of Dirac Fermions with Cold Atoms in an Optical Lattice, Phys. Rev. Lett. **98**, 260402 (2007).

[45] L. Tarruell, D. Greif, T. Uehlinger, G. Jotzu, and T. Esslinger, Creating, moving and merging Dirac points with a Fermi gas in a tunable honeycomb lattice, Nature **483**, 302 (2012).

[46] C. Gattringer and C. B. Lang, *Quantum Chromodynamics on the Lattice* (Springer, Berlin, 2010), Vol. 788.

[47] A. Bermudez, L. Mazza, M. Rizzi, N. Goldman, M. Lewenstein, and M. A. Martin-Delgado, Wilson Fermions and Axion Electrodynamics in Optical Lattices, Phys. Rev. Lett. **105**, 190404 (2010).

[48] N. Goldman, J. C. Budich, and P. Zoller, Topological quantum matter with ultracold gases in optical lattices, Nat. Phys. **12**, 639 (2016).

[49] J. I. Cirac, P. Maraner, and J. K. Pachos, Cold Atom Simulation of Interacting Relativistic Quantum Field Theories, Phys. Rev. Lett. **105**, 190403 (2010).

[50] J. Jünemann, A. Piga, S.-J. Ran, M. Lewenstein, M. Rizzi, and A. Bermudez, Exploring Interacting Topological Insulators with Ultracold Atoms: The Synthetic Creutz-Hubbard Model, Phys. Rev. X **7**, 031057 (2017).

[51] A. Bermudez, E. Tirrito, M. Rizzi, M. Lewenstein, and S. Hands, Gross-Neveu-Wilson model and correlated symmetry-protected topological phases, Ann. Phys. (N. Y.) **399**, 149 (2018).

[52] L. Ziegler, E. Tirrito, M. Lewenstein, S. Hands, and A. Bermudez, Correlated Chern insulators in two-dimensional Raman lattices: a cold-atom regularization of strongly-coupled four-Fermi field theories, ArXiv:2011.08744 (2020).

[53] A. Bermudez, G. Aarts, and M. Müller, Quantum Sensors for the Generating Functional of Interacting Quantum Field Theories, Phys. Rev. X **7**, 041012 (2017).

[54] N. Klco and M. J. Savage, Digitization of scalar fields for quantum computing, Phys. Rev. A **99**, 052335 (2019).

[55] C. N. Yang and R. L. Mills, Conservation of isotopic spin and isotopic gauge invariance, Phys. Rev. **96**, 191 (1954).

[56] T. Byrnes and Y. Yamamoto, Simulating lattice gauge theories on a quantum computer, Phys. Rev. A **73**, 022328 (2006).

[57] H. P. Büchler, M. Hermele, S. D. Huber, M. P. A. Fisher, and P. Zoller, Atomic Quantum Simulator for Lattice Gauge Theories and Ring Exchange Models, Phys. Rev. Lett. **95**, 040402 (2005).

[58] H. Weimer, M. Müller, I. Lesanovsky, P. Zoller, and H. P. Büchler, A Rydberg quantum simulator, Nat. Phys. **6**, 382 (2010).

[59] L. Tagliacozzo, A. Celi, P. Orland, M. W. Mitchell, and M. Lewenstein, Simulation of non-Abelian gauge theories with optical lattices, Nat. Commun. **4**, 2615 (2013).

[60] E. Zohar, J. I. Cirac, and B. Reznik, Simulating Compact Quantum Electrodynamics with Ultracold Atoms: Probing Confinement and Nonperturbative Effects, Phys. Rev. Lett. **109**, 125302 (2012).

[61] D. Banerjee, M. Dalmonte, M. Müller, E. Rico, P. Stebler, U.-J. Wiese, and P. Zoller, Atomic Quantum Simulation of Dynamical Gauge Fields Coupled to Fermionic Matter: From String Breaking to Evolution After a Quench, Phys. Rev. Lett. **109**, 175302 (2012).

[62] E. A. Martinez, C. A. Muschik, P. Schindler, D. Nigg, A. Erhard, M. Heyl, P. Hauke, M. Dalmonte, T. Monz, P. Zoller, and R. Blatt, Real-time dynamics of lattice gauge theories with a few-qubit quantum computer, Nature **534**, 516 (2016).

[63] F. Görg, K. Sandholzer, J. Minguzzi, R. Desbuquois, M. Messer, and T. Esslinger, Realization of density-dependent peierls phases to engineer quantized gauge fields coupled to ultracold matter, Nat. Phys. **15**, 1161 (2019).

[64] C. Schweizer, F. Grusdt, M. Berngruber, L. Barbiero, E. Demler, N. Goldman, I. Bloch, and M. Aidelsburger, Floquet approach to $\mathbb{Z}_2$ lattice gauge theories with ultracold atoms in optical lattices, Nat. Phys. **15**, 1168 (2019).

[65] A. Mil, T. V. Zache, A. Hegde, A. Xia, R. P. Bhatt, M. K. Oberthaler, P. Hauke, J. Berges, and F. Jendrzejewski, A scalable realization of local $U(1)$ gauge invariance in cold atomic mixtures, Science **367**, 1128 (2020).

[66] F. M. Surace, P. P. Mazza, G. Giudici, A. Lerose, A. Gambassi, and M. Dalmonte, Lattice Gauge Theories and String Dynamics in Rydberg Atom Quantum Simulators, Phys. Rev. X **10**, 021041 (2020).

[67] B. Yang, H. Sun, R. Ott, H.-Y. Wang, T. V. Zache, J. C. Halimeh, Z.-S. Yuan, P. Hauke, and J.-W. Pan, Observation of gauge invariance in a 71-site Bose–Hubbard quantum simulator, Nature **587**, 392 (2020).

[68] C. Kokail, C. Maier, R. van Bijnen, T. Brydges, M. K. Joshi, P. Jurcevic, C. A. Muschik, P. Silvi, R. Blatt,

C. F. Roos, and P. Zoller, Self-verifying variational quantum simulation of lattice models, Nature **569**, 355 (2019).

[69] Y. Atas, J. Zhang, R. Lewis, A. Jahanpour, J. F. Haase, and C. A. Muschik, Su(2) hadrons on a quantum computer, ArXiv:2102.08920, (2021).

[70] N. Klco, E. F. Dumitrescu, A. J. McCaskey, T. D. Morris, R. C. Pooser, M. Sanz, E. Solano, P. Lougovski, and M. J. Savage, Quantum-classical computation of schwinger model dynamics using quantum computers, Phys. Rev. A **98**, 032331 (2018).

[71] H. Lamm and S. Lawrence, Simulation of Nonequilibrium Dynamics on a Quantum Computer, Phys. Rev. Lett. **121**, 170501 (2018).

[72] H. Lamm, S. Lawrence, and Y. Yamauchi, (NuQS Collaboration), General methods for digital quantum simulation of gauge theories, Phys. Rev. D **100**, 034518 (2019).

[73] D. B. Kaplan and J. R. Stryker, Gauss's law, duality, and the Hamiltonian formulation of $U(1)$ lattice gauge theory, Phys. Rev. D **102**, 094515 (2020).

[74] G. Magnifico, D. Vodola, E. Ercolessi, S. P. Kumar, M. Müller, and A. Bermudez, Symmetry-protected topological phases in lattice gauge theories: Topological QED_2, Phys. Rev. D **99**, 014503 (2019).

[75] G. Magnifico, D. Vodola, E. Ercolessi, S. P. Kumar, M. Müller, and A. Bermudez, $\mathbb{Z}_N$ gauge theories coupled to topological fermions: QED_2 with a quantum mechanical θ angle, Phys. Rev. B **100**, 115152 (2019).

[76] D. González-Cuadra, L. Tagliacozzo, M. Lewenstein, and A. Bermudez, Robust Topological Order in Fermionic $\mathbb{Z}_2$ Gauge Theories: From Aharonov-Bohm Instability to Soliton-Induced Deconfinement, Phys. Rev. X **10**, 041007 (2020).

[77] U. Borla, B. Jeevanesan, F. Pollmann, and S. Moroz, Quantum phases of two-dimensional $\mathbb{Z}_2$ gauge theory coupled to single-component fermion matter, ArXiv:2012.08543 (2021).

[78] R. J. Glauber, The quantum theory of optical coherence, Phys. Rev. **130**, 2529 (1963).

[79] B. R. Mollow, Quantum theory of field attenuation, Phys. Rev. **168**, 1896 (1968).

[80] M. O. Scully and W. E. Lamb, Quantum theory of an optical maser. III. Theory of photoelectron counting statistics, Phys. Rev. **179**, 368 (1969).

[81] P. W. Milonni, D. F. V. James, and H. Fearn, Photodetection and causality in quantum optics, Phys. Rev. A **52**, 1525 (1995).

[82] R. H. Brown and R. Q. Twiss, Correlation between photons in two coherent beams of light, Nature **177**, 27 (1956).

[83] R. Hanbury Brown and R. Q. Twiss, The question of correlation between photons in coherent light rays, Nature **178**, 1447 (1956).

[84] W. G. Unruh, Notes on black-hole evaporation, Phys. Rev. D **14**, 870 (1976).

[85] N. D. Birrell and P. Davies, *Quantum Fields in Curved Space* (Cambridge University Press, Cambridge, 1999).

[86] L. C. B. Crispino, A. Higuchi, and G. E. A. Matsas, The Unruh effect and its applications, Rev. Mod. Phys. **80**, 787 (2008).

[87] B. DeWitt, *General Relativity: An Einstein Centenary Survey*, edited by S. Hawking and W. Israel (Cambridge University Press, 2010).

[88] W. G. Unruh and R. M. Wald, What happens when an accelerating observer detects a Rindler particle, Phys. Rev. D **29**, 1047 (1984).

[89] W. G. Unruh, Thermal bath and decoherence of Rindler spacetimes, Phys. Rev. D **46**, 3271 (1992).

[90] J. de Ramón, L. J. Garay, and E. Martín-Martínez, Direct measurement of the two-point function in quantum fields, Phys. Rev. D **98**, 105011 (2018).

[91] C. L. Degen, F. Reinhard, and P. Cappellaro, Quantum sensing, Rev. Mod. Phys. **89**, 035002 (2017).

[92] N. F. Ramsey, A molecular beam resonance method with separated oscillating fields, Phys. Rev. **78**, 695 (1950).

[93] A. D. Ludlow, M. M. Boyd, J. Ye, E. Peik, and P. O. Schmidt, Optical atomic clocks, Rev. Mod. Phys. **87**, 637 (2015).

[94] M. Bruderer and D. Jaksch, Probing BEC phase fluctuations with atomic quantum dots, New J. Phys. **8**, 87 (2006).

[95] F. Schmidt, D. Mayer, Q. Bouton, D. Adam, T. Lausch, N. Spethmann, and A. Widera, Quantum Spin Dynamics of Individual Neutral Impurities Coupled to a Bose-Einstein Condensate, Phys. Rev. Lett. **121**, 130403 (2018).

[96] T. J. Elliott and T. H. Johnson, Nondestructive probing of means, variances, and correlations of ultracold-atomic-system densities via qubit impurities, Phys. Rev. A **93**, 043612 (2016).

[97] M. Streif, A. Buchleitner, D. Jaksch, and J. Mur-Petit, Measuring correlations of cold-atom systems using multiple quantum probes, Phys. Rev. A **94**, 053634 (2016).

[98] L. S. Levitov, H. Lee, and G. B. Lesovik, Electron counting statistics and coherent states of electric current, J. Math. Phys. **37**, 4845 (1996).

[99] G. B. Lesovik, F. Hassler, and G. Blatter, Using Qubits to Measure Fidelity in Mesoscopic Systems, Phys. Rev. Lett. **96**, 106801 (2006).

[100] A. Bermudez, M. Bruderer, and M. B. Plenio, Controlling and Measuring Quantum Transport of Heat in Trapped-Ion Crystals, Phys. Rev. Lett. **111**, 040601 (2013).

[101] R. Dorner, S. R. Clark, L. Heaney, R. Fazio, J. Goold, and V. Vedral, Extracting Quantum Work Statistics and Fluctuation Theorems by Single-Qubit Interferometry, Phys. Rev. Lett. **110**, 230601 (2013).

[102] L. Mazzola, G. De Chiara, and M. Paternostro, Measuring the Characteristic Function of the Work Distribution, Phys. Rev. Lett. **110**, 230602 (2013).

[103] E. Zohar and B. Reznik, Topological Wilson-Loop area law manifested using a superposition of loops, New J. Phys. **15**, 043041 (2013).

[104] O. Klein, Quantentheorie und fünfdimensionale relativitätstheorie, Z. Phys. **37**, 895 (1926).

[105] W. Gordon, Der comptoneffekt nach der schrödingerschen theorie, Z. Phys. **40**, 117 (1926).

[106] K. G. Wilson and J. Kogut, The renormalization group and the ϵ expansion, Phys. Rep. **12**, 75 (1974).

[107] J. Schwinger, On the Green's functions of quantized fields. I, Proc. Natl. Acad. Sci. **37**, 452 (1951).

[108] J. Schwinger, On the Green's functions of quantized fields. II, Proc. Natl. Acad. Sci. **37**, 455 (1951).

[109] I. Pogorelov, T. Feldker, C. D. Marciniak, L. Postler, G. Jacob, O. Krieglsteiner, V. Podlesnic, M. Meth, V. Negnevitsky, M. Stadler, B. Höfer, C. Wächter, K. Lakhmanskiy, R. Blatt, P. Schindler, and T. Monz, Compact iontrap quantum computing demonstrator, PRX Quantum **2**, 020343 (2021).

[110] L. Postler, S. Heußen, I. Pogorelov, M. Rispler, T. Feldker, M. Meth, C. D. Marciniak, R. Stricker, M. Ringbauer, R. Blatt, P. Schindler, M. Müller, and T. Monz, Demonstration of fault-tolerant universal quantum gate operations, ArXiv:2111.12654 (2021).

[111] S. Fishman, G. De Chiara, T. Calarco, and G. Morigi, Structural phase transitions in low-dimensional ion crystals, Phys. Rev. B **77**, 064111 (2008).

[112] F. Kranzl, M. K. Joshi, C. Maier, T. Brydges, J. Franke, R. Blatt, and C. F. Roos, Controlling long ion strings for quantum simulation and precision measurements, ArXiv:2112.10655 (2021).

[113] T. J. Hollowood, *Renormalization Group and Fixed Points*, SpringerBriefs in Physics (Springer, Berlin, 2013).

[114] W. Magnus, On the exponential solution of differential equations for a linear operator, Commun. Pure. Appl. Math. **7**, 649 (1954).

[115] S. Blanes, F. Casas, J. A. Oteo, and J. Ros, A pedagogical approach to the magnus expansion, Eur. J. Phys. **31**, 907 (2010).

[116] H. Häffner, C. Roos, and R. Blatt, Quantum computing with trapped ions, Phys. Rep. **469**, 155 (2008).

[117] T. D. Ladd, F. Jelezko, R. Laflamme, Y. Nakamura, C. Monroe, and J. L. O'Brien, Quantum computers, Nature **464**, 45 (2010).

[118] A. J. Leggett, S. Chakravarty, A. T. Dorsey, M. P. A. Fisher, A. Garg, and W. Zwerger, Dynamics of the dissipative two-state system, Rev. Mod. Phys. **59**, 1 (1987).

[119] W. G. Unruh, Maintaining coherence in quantum computers, Phys. Rev. A **51**, 992 (1995).

[120] G. M. Palma, K.-A. Suominen, and A. Ekert, Quantum computers and dissipation, Proc. R. Soc. London, A **452**, 567 (1996).

[121] G. Díaz-Camacho, A. Bermudez, and J. J. García-Ripoll, Dynamical polaron *Ansatz*: A theoretical tool for the ultrastrong-coupling regime of circuit QED, Phys. Rev. A **93**, 043843 (2016).

[122] J. Zinn-Justin, *Quantum Field Theory and Critical Phenomena* (Clarendon Press, Oxford, 2012).

[123] J. Zinn-Justin, *Phase Transitions and Renormalization Group* (Oxford Univ. Press, Oxford, 2013).

[124] E. Fradkin, *Quantum Field Theory: An Integrated Approach* (Princeton University Press, Princeton, 2021).

[125] I. S. Gradshteĭn, A. Jeffrey, and I. M. Ryzhik, *Table of Integrals, Series, and Products* (Academic Press, New York, 1965), pp. xiv. 1086 p.

[126] H. Yukawa, On the interaction of elementary particles. I, Prog. Theor. Phys. Suppl. **1**, 1 (1955).

[127] P. Jordan and E. Wigner, Über das paulische äquivalenzverbot, Z. Phys. **47**, 631 (1928).

[128] P. Pfeuty, The one-dimensional Ising model with a transverse field, Ann. Phys. (N. Y.) **57**, 79 (1970).

[129] J. B. Kogut, An introduction to lattice gauge theory and spin systems, Rev. Mod. Phys. **51**, 659 (1979).

[130] E. L. Hahn, Spin echoes, Phys. Rev. **80**, 580 (1950).

[131] D. Suter and G. A. Álvarez, Colloquium: Protecting quantum information against environmental noise, Rev. Mod. Phys. **88**, 041001 (2016).

[132] S. Coleman and E. Weinberg, Radiative corrections as the origin of spontaneous symmetry breaking, Phys. Rev. D **7**, 1888 (1973).

[133] R. Jackiw, Functional evaluation of the effective potential, Phys. Rev. D **9**, 1686 (1974).

[134] L. Dolan and R. Jackiw, Symmetry behavior at finite temperature, Phys. Rev. D **9**, 3320 (1974).

[135] S. Weinberg, Gauge and global symmetries at high temperature, Phys. Rev. D **9**, 3357 (1974).

[136] K. G. Wilson and M. E. Fisher, Critical Exponents in 3.99 Dimensions, Phys. Rev. Lett. **28**, 240 (1972).

[137] M. E. Fisher, Renormalization group theory: Its basis and formulation in statistical physics, Rev. Mod. Phys. **70**, 653 (1998).

[138] J. Glimm and A. Jaffe, A $\lambda\phi^4$ quantum field theory without cutoffs. I, Phys. Rev. **176**, 1945 (1968).

[139] J. Glimm and A. Jaffe, Positivity of the φ hamiltonian, Fortsch. Phys. **21**, 327 (1973).

[140] J. S. Feldman and K. Osterwalder, The Wightman axioms and the mass gap for weakly coupled $(\phi^4)_3$ quantum field theories, Ann. Phys. (N. Y.) **97**, 80 (1976).

[141] J. Glimm and A. Jaffe, Remark on the Existence of ϕ_4^4, Phys. Rev. Lett. **33**, 440 (1974).

[142] M. Lüscher and P. Weisz, Scaling laws and triviality bounds in the lattice φ^4 theory: (I). one-component model in the symmetric phase, Nucl. Phys. B **290**, 25 (1987).

[143] M. Aizenman, Proof of the Triviality of ϕ_d^4 Field Theory and Some Mean-Field Features of Ising Models for $d > 4$, Phys. Rev. Lett. **47**, 1 (1981).

[144] J. Fröhlich, On the triviality of $\lambda\varphi_d^4$ theories and the approach to the critical point in $d_{(-)} > 4$ dimensions, Nucl. Phys. B **200**, 281 (1982).

[145] J. M. Radcliffe, Some properties of coherent spin states, J. Phys. A: Gen. Phys. **4**, 313 (1971).

[146] F. Haldane, Continuum dynamics of the 1-D Heisenberg antiferromagnet: Identification with the $O(3)$ nonlinear sigma model, Phys. Lett. A **93**, 464 (1983).

[147] E. Fradkin and M. Stone, Topological terms in one- and two-dimensional quantum Heisenberg antiferromagnets, Phys. Rev. B **38**, 7215 (1988).

[148] M. Gell-Mann and M. Lévy, The axial vector current in beta decay, Il Nuovo Cimento (1955–1965) **16**, 705 (1960).

[149] R. Shankar, Renormalization-group approach to interacting fermions, Rev. Mod. Phys. **66**, 129 (1994).

[150] P. K. Ghosh, *Ion Traps* (Clarendon Press, Oxford, 1995).

[151] D. H. E. Dubin and T. M. O'Neil, Trapped nonneutral plasmas, liquids, and crystals (the thermal equilibrium states), Rev. Mod. Phys. **71**, 87 (1999).

[152] D. J. Wineland and W. M. Itano, Laser cooling of atoms, Phys. Rev. A **20**, 1521 (1979).

[153] W. M. Itano and D. J. Wineland, Laser cooling of ions stored in harmonic and penning traps, Phys. Rev. A **25**, 35 (1982).

[154] D. J. Wineland, W. M. Itano, J. C. Bergquist, and R. G. Hulet, Laser-cooling limits and single-ion spectroscopy, Phys. Rev. A **36**, 2220 (1987).

[155] J. I. Cirac, R. Blatt, P. Zoller, and W. D. Phillips, Laser cooling of trapped ions in a standing wave, Phys. Rev. A **46**, 2668 (1992).

[156] G. Morigi, J. Eschner, and C. H. Keitel, Ground State Laser Cooling Using Electromagnetically Induced Transparency, Phys. Rev. Lett. **85**, 4458 (2000).

[157] J. Eschner, G. Morigi, F. Schmidt-Kaler, and R. Blatt, Laser cooling of trapped ions, J. Opt. Soc. Am. B **20**, 1003 (2003).

[158] F. Diedrich, E. Peik, J. M. Chen, W. Quint, and H. Walther, Observation of a Phase Transition of Stored Laser-Cooled Ions, Phys. Rev. Lett. **59**, 2931 (1987).

[159] D. J. Wineland, J. C. Bergquist, W. M. Itano, J. J. Bollinger, and C. H. Manney, Atomic-Ion Coulomb Clusters in an Ion Trap, Phys. Rev. Lett. **59**, 2935 (1987).

[160] M. G. Raizen, J. M. Gilligan, J. C. Bergquist, W. M. Itano, and D. J. Wineland, Ionic crystals in a linear Paul trap, Phys. Rev. A **45**, 6493 (1992).

[161] S. L. Gilbert, J. J. Bollinger, and D. J. Wineland, Shell-Structure Phase of Magnetically Confined Strongly Coupled Plasmas, Phys. Rev. Lett. **60**, 2022 (1988).

[162] G. Birkl, S. Kassner, and H. Walther, Multiple-shell structures of laser-cooled ^{24}Mg$^+$ ions in a quadrupole storage ring, Nature **357**, 310 (1992).

[163] D. Leibfried, R. Blatt, C. Monroe, and D. Wineland, Quantum dynamics of single trapped ions, Rev. Mod. Phys. **75**, 281 (2003).

[164] D. J. Berkeland, J. D. Miller, J. C. Bergquist, W. M. Itano, and D. J. Wineland, Minimization of ion micromotion in a Paul trap, J. Appl. Phys. **83**, 5025 (1998).

[165] A. Bermudez, P. Schindler, T. Monz, R. Blatt, and M. Müller, Micromotion-enabled improvement of quantum logic gates with trapped ions, New J. Phys. **19**, 113038 (2017).

[166] D. F. V. James, Quantum dynamics of cold trapped ions with application to quantum computation, Appl. Phys. B **66**, 181 (1998).

[167] P. C. Hohenberg, Existence of long-range order in one and two dimensions, Phys. Rev. **158**, 383 (1967).

[168] N. D. Mermin and H. Wagner, Absence of Ferromagnetism or Antiferromagnetism in One- or Two-Dimensional Isotropic Heisenberg Models, Phys. Rev. Lett. **17**, 1133 (1966).

[169] S. Coleman, There are no Goldstone bosons in two dimensions, Commun. Math. Phys. **31**, 259 (1973).

[170] G. Morigi and S. Fishman, Eigenmodes and Thermodynamics of a Coulomb Chain in a Harmonic Potential, Phys. Rev. Lett. **93**, 170602 (2004).

[171] G. Morigi and S. Fishman, Dynamics of an ion chain in a harmonic potential, Phys. Rev. E **70**, 066141 (2004).

[172] X.-L. Deng, D. Porras, and J. I. Cirac, Effective spin quantum phases in systems of trapped ions, Phys. Rev. A **72**, 063407 (2005).

[173] D. L. Goodstein, *States of Matter* (Dover Publications, Inc., Mineola, NY, 2017).

[174] M. Ashcroft, *Solid State Physics: Revised Edition* (Cengage Learning, Boston, MA, 2016).

[175] I. Affleck, *Field Theory Methods and Quantum Critical Phenomena Course 10* (North-Holland, Netherlands, 1990).

[176] R. Shankar, *Bosonization: How to Make it Work for You in Condensed Matter* (World Scientific, Singapore, 1995), p. 353.

[177] E. Shimshoni, G. Morigi, and S. Fishman, Quantum Zigzag Transition in Ion Chains, Phys. Rev. Lett. **106**, 010401 (2011).

[178] A. Bermudez and M. B. Plenio, Spin Peierls Quantum Phase Transitions in Coulomb Crystals, Phys. Rev. Lett. **109**, 010501 (2012).

[179] F. D. M. Haldane, Effective Harmonic-Fluid Approach to Low-Energy Properties of One-Dimensional Quantum Fluids, Phys. Rev. Lett. **47**, 1840 (1981).

[180] T. Giamarchi, *Quantum Physics in One Dimension* (Clarendon Press, Oxford, 2010).

[181] A. Luther and I. Peschel, Calculation of critical exponents in two dimensions from quantum field theory in one dimension, Phys. Rev. B **12**, 3908 (1975).

[182] V. J. Emery, Theory of the quasi-one-dimensional electron gas with strong on-site interactions, Phys. Rev. B **14**, 2989 (1976).

[183] F. D. M. Haldane, General Relation of Correlation Exponents and Spectral Properties of One-Dimensional Fermi Systems: Application to the Anisotropic $s = \frac{1}{2}$ Heisenberg Chain, Phys. Rev. Lett. **45**, 1358 (1980).

[184] S.-I. Tomonaga, Remarks on Bloch's method of sound waves applied to many-fermion problems, Prog. Theor. Phys. **5**, 544 (1950).

[185] J. M. Luttinger, An exactly soluble model of a many-fermion system, J. Math. Phys. **4**, 1154 (1963).

[186] F. D. M. Haldane, 'Luttinger liquid theory' of one-dimensional quantum fluids. I. properties of the Luttinger model and their extension to the general 1D interacting spinless Fermi gas, J. Phys. C: Solid State Phys. **14**, 2585 (1981).

[187] S. Coleman, Quantum sine-Gordon equation as the massive Thirring model, Phys. Rev. D **11**, 2088 (1975).

[188] D. Senechal, in *Theoretical Methods for Strongly Correlated Electrons*, edited by C. Bourbonnais, D. Senechal, A.-M. Tremblay (Springer, 2004), p. 139.

[189] J. von Delft and H. Schoeller, Bosonization for beginners—refermionization for experts, Ann. Phys. **7**, 225 (1998).

[190] V. J. Emery, in *Correlated Electron Systems*, edited by V. J. Emery (World Scientific, 1993), p. 166.

[191] J. Gonzalez, in *Quantum Electron Liquids and High-Tc Superconductivity*, edited by J. Gonzalez, M.A. Martin-Delgado, G. Sierra, and A.H. Vozmediano (Springer, 1995), p. 109.

[192] A. Sørensen and K. Mølmer, Quantum Computation with Ions in Thermal Motion, Phys. Rev. Lett. **82**, 1971 (1999).

[193] D. Leibfried, B. DeMarco, V. Meyer, D. Lucas, M. Barrett, J. Britton, W. M. Itano, B. Jelenković, C. Langer, T. Rosenband, and D. J. Wineland, Experimental demonstration of a robust, high-fidelity geometric two ion-qubit phase gate, Nature **422**, 412 (2003).

[194] K.-A. B. Soderberg and C. Monroe, Phonon-mediated entanglement for trapped ion quantum computing, Rep. Progr. Phys. **73**, 036401 (2010).

[195] L. D. Landau and E. M. Lifshitz, *Theory of Elasticity* (Butterworth-Heinemann, Oxford, 2008).

[196] K. S. Thorne and R. D. Blandford, *Modern Classical Physics: Optics, Fluids, Plasmas, Elasticity, Relativity, and Statistical Physics* (Princeton University Press, Princeton, 2017).

[197] C. Senko, J. Smith, P. Richerme, A. Lee, W. C. Campbell, and C. Monroe, Coherent imaging spectroscopy of a quantum many-body spin system, Science **345**, 430 (2014).

[198] J. W. Britton, B. C. Sawyer, A. C. Keith, C.-C. J. Wang, J. K. Freericks, H. Uys, M. J. Biercuk, and J. J. Bollinger, Engineered two-dimensional Ising interactions in a trapped-ion quantum simulator with hundreds of spins, Nature **484**, 489 (2012).

[199] R. Islam, C. Senko, W. C. Campbell, S. Korenblit, J. Smith, A. Lee, E. E. Edwards, C.-C. J. Wang, J. K. Freericks, and C. Monroe, Emergence and frustration of magnetism with variable-range interactions in a quantum simulator, Science **340**, 583 (2013).

[200] P. Richerme, Z.-X. Gong, A. Lee, C. Senko, J. Smith, M. Foss-Feig, S. Michalakis, A. V. Gorshkov, and C. Monroe, Non-local propagation of correlations in quantum systems with long-range interactions, Nature **511**, 198 (2014).

[201] P. Jurcevic, B. P. Lanyon, P. Hauke, C. Hempel, P. Zoller, R. Blatt, and C. F. Roos, Quasiparticle engineering and entanglement propagation in a quantum many-body system, Nature **511**, 202 (2014).

[202] J. Smith, A. Lee, P. Richerme, B. Neyenhuis, P. W. Hess, P. Hauke, M. Heyl, D. A. Huse, and C. Monroe, Many-body localization in a quantum simulator with programmable random disorder, Nat. Phys. **12**, 907 (2016).

[203] B. P. Lanyon, C. Maier, M. Holzäpfel, T. Baumgratz, C. Hempel, P. Jurcevic, I. Dhand, A. S. Buyskikh, A. J. Daley, M. Cramer, M. B. Plenio, R. Blatt, and C. F. Roos, Efficient tomography of a quantum many-body system, Nat. Phys. **13**, 1158 (2017).

[204] N. Friis, O. Marty, C. Maier, C. Hempel, M. Holzäpfel, P. Jurcevic, M. B. Plenio, M. Huber, C. Roos, R. Blatt, and B. Lanyon, Observation of Entangled States of a Fully Controlled 20-Qubit System, Phys. Rev. X **8**, 021012 (2018).

[205] C. Monroe, W. Campbell, E. Edwards, R. Islam, D. Kafri, S. Korenblit, A. Lee, P. Richerme, C. Senko, and J. Smith, *et al.*, *Quantum Simulation of Spin Models with Trapped Ions* (IOS Press Ebooks, Amsterdam, 2015).

[206] P. Nevado and D. Porras, Hidden frustrated interactions and quantum annealing in trapped-ion spin-phonon chains, Phys. Rev. A **93**, 013625 (2016).

[207] A. Bermudez, L. Tagliacozzo, G. Sierra, and P. Richerme, Long-range Heisenberg models in quasiperiodically driven crystals of trapped ions, Phys. Rev. B **95**, 024431 (2017).

[208] A. Bermudez, J. Almeida, F. Schmidt-Kaler, A. Retzker, and M. B. Plenio, Frustrated Quantum Spin Models with

Cold Coulomb Crystals, Phys. Rev. Lett. **107**, 207209 (2011).

[209] A. Bermudez, J. Almeida, K. Ott, H. Kaufmann, S. Ulm, U. Poschinger, F. Schmidt-Kaler, A. Retzker, and M. B. Plenio, Quantum magnetism of spin-ladder compounds with trapped-ion crystals, New J. Phys. **14**, 093042 (2012).

[210] G. Källén, On the definition of the renormalization constants in quantum electrodynamics, Helv. Phys. Acta **25**, 417 (1952).

[211] H. Lehmann, Über eigenschaften von ausbreitungsfunktionen und renormierungskonstanten quantisierter felder, Il Nuovo Cimento (1943–1954) **11**, 342 (1954).

[212] R. Zwicky, A brief introduction to dispersion relations and analyticity, ArXiv:1610.06090 (2016).

[213] E. M. Stein and R. Shakarchi, *Real Analysis: Measure Theory, Integration, and Hilbert Spaces* (Princeton University Press, Princeton, 2005).

[214] J. P. Schiffer, Phase Transitions in Anisotropically Confined Ionic Crystals, Phys. Rev. Lett. **70**, 818 (1993).

[215] S. Ulm, J. Roßnagel, G. Jacob, C. Degünther, S. T. Dawkins, U. G. Poschinger, R. Nigmatullin, A. Retzker, M. B. Plenio, F. Schmidt-Kaler, and K. Singer, Observation of the Kibble–Zurek scaling law for defect formation in ion crystals, Nat. Commun. **4**, 2290 (2013).

[216] K. Pyka, J. Keller, H. L. Partner, R. Nigmatullin, T. Burgermeister, D. M. Meier, K. Kuhlmann, A. Retzker, M. B. Plenio, W. H. Zurek, A. del Campo, and T. E. Mehlstäubler, Topological defect formation and spontaneous symmetry breaking in ion coulomb crystals, Nat. Commun. **4**, 2291 (2013).

[217] M. Mielenz, J. Brox, S. Kahra, G. Leschhorn, M. Albert, T. Schaetz, H. Landa, and B. Reznik, Trapping of Topological-Structural Defects in Coulomb Crystals, Phys. Rev. Lett. **110**, 133004 (2013).

[218] S. Ejtemaee and P. C. Haljan, Spontaneous nucleation and dynamics of kink defects in zigzag arrays of trapped ions, Phys. Rev. A **87**, 051401 (2013).

[219] J. Brox, P. Kiefer, M. Bujak, T. Schaetz, and H. Landa, Spectroscopy and Directed Transport of Topological Solitons in Crystals of Trapped Ions, Phys. Rev. Lett. **119**, 153602 (2017).

[220] L. P. Kadanoff, Scaling laws for Ising models near T_c, Phys. Phys. Fiz. **2**, 263 (1966).

[221] D. Podolsky, E. Shimshoni, P. Silvi, S. Montangero, T. Calarco, G. Morigi, and S. Fishman, From classical to quantum criticality, Phys. Rev. B **89**, 214408 (2014).

[222] P. Silvi, G. De Chiara, T. Calarco, G. Morigi, and S. Montangero, Full characterization of the quantum linear-zigzag transition in atomic chains, Ann. Phys. **525**, 827 (2013).

[223] D. Porras and J. I. Cirac, Bose-Einstein Condensation and Strong-Correlation Behavior of Phonons in Ion Traps, Phys. Rev. Lett. **93**, 263602 (2004).

[224] K. R. Brown, C. Ospelkaus, Y. Colombe, A. C. Wilson, D. Leibfried, and D. J. Wineland, Coupled quantized mechanical oscillators, Nature **471**, 196 (2011).

[225] M. Harlander, R. Lechner, M. Brownnutt, R. Blatt, and W. Hänsel, Trapped-ion antennae for the transmission of quantum information, Nature **471**, 200 (2011).

[226] S. Haze, Y. Tateishi, A. Noguchi, K. Toyoda, and S. Urabe, Observation of phonon hopping in radial vibrational modes of trapped ions, Phys. Rev. A **85**, 031401 (2012).

[227] M. Ramm, T. Pruttivarasin, and H. Häffner, Energy transport in trapped ion chains, New J. Phys. **16**, 063062 (2014).

[228] S. Debnath, N. M. Linke, S.-T. Wang, C. Figgatt, K. A. Landsman, L.-M. Duan, and C. Monroe, Observation of Hopping and Blockade of Bosons in a Trapped ion Spin Chain, Phys. Rev. Lett. **120**, 073001 (2018).

[229] K. Toyoda, Y. Matsuno, A. Noguchi, S. Haze, and S. Urabe, Experimental Realization of a Quantum Phase Transition of Polaritonic Excitations, Phys. Rev. Lett. **111**, 160501 (2013).

[230] A. Abdelrahman, O. Khosravani, M. Gessner, A. Buchleitner, H.-P. Breuer, D. Gorman, R. Masuda, T. Pruttivarasin, M. Ramm, P. Schindler, and H. Häffner, Local probe of single phonon dynamics in warm ion crystals, Nat. Commun. **8**, 15712 (2017).

[231] F. Hakelberg, P. Kiefer, M. Wittemer, U. Warring, and T. Schaetz, Interference in a Prototype of a Two-Dimensional Ion Trap Array Quantum Simulator, Phys. Rev. Lett. **123**, 100504 (2019).

[232] A. Eckardt, Colloquium: Atomic quantum gases in periodically driven optical lattices, Rev. Mod. Phys. **89**, 011004 (2017).

[233] D. H. Dunlap and V. M. Kenkre, Dynamic localization of a charged particle moving under the influence of an electric field, Phys. Rev. B **34**, 3625 (1986).

[234] A. Bermudez, T. Schaetz, and D. Porras, Synthetic Gauge Fields for Vibrational Excitations of Trapped Ions, Phys. Rev. Lett. **107**, 150501 (2011).

[235] P. Kiefer, F. Hakelberg, M. Wittemer, A. Bermúdez, D. Porras, U. Warring, and T. Schaetz, Floquet-Engineered Vibrational Dynamics in a Two-Dimensional Array of Trapped Ions, Phys. Rev. Lett. **123**, 213605 (2019).

[236] J. Schwinger, On the Green's functions of quantized fields. I, Proc. Natl. Acad. Sci. **37**, 452 (1951).

[237] R. Achilles and A. Bonfiglioli, The early proofs of the theorem of Campbell, Baker, Hausdorff, and Dynkin, Arch. Hist. Exact. Sci. **66**, 295 (2012).

[238] E. Abers and B. Lee, Gauge theories, Phys. Rep. **9**, 1 (1973).

[239] L. H. Ryder, *Quantum Field Theory* (Cambridge University Press, Cambridge, 1996).

[240] F. J. Dyson, The *s* matrix in quantum electrodynamics, Phys. Rev. **75**, 1736 (1949).

[241] P. Debye, Zur theorie der spezifischen wärmen, Ann. Phys. **344**, 789 (1912).

[242] K. G. Wilson, Confinement of quarks, Phys. Rev. D **10**, 2445 (1974).

[243] T. Holstein, Studies of polaron motion: Part I. The molecular-crystal model, Ann. Phys. (N. Y.) **8**, 325 (1959).

[244] S. Sachdev, *Quantum Phase Transitions* (Cambridge University Press, Cambridge, 2011), 2nd ed.